In-situ fabricated epitaxial organic/ferromagnetic contacts for the combination of single-molecule interface characterization and device-level transport measurements

Inaugural-Dissertation

zur

Erlangung des Doktorgrades

der Mathematisch-Naturwissenschaftlichen Fakultät

der Universität zu Köln

vorgelegt von

Samuel Königshofen, geb. Lehnert
aus Dormagen

2022

Berichterstatter: (Gutachter)	PD Dr. Daniel E. Bürgler Prof. Dr. Thomas Michely

Tag der mündlichen Prüfung: 17.01.2022

VolkswagenStiftung

Diese Dissertation wurde Rahmen des von der Volkswagen Stiftung geförderten Projekts ”Optically Controlled Spin Logic” am Forschungszentrum Jülich angefertig.

Teile dieser Dissertation wurden veröffentlicht als:

„Epitaxial and contamination-free Co(0001) electrodes on insulating substrates for molecular spintronic devices “,
S. Königshofen, F. Matthes, D.E. Bürgler, C.M. Schneider, E. Dirksen, T.J.J.Müller
Thin Solid Films, **680**, 67-74 (2019)

Das wachsende Feld der molekularen Spinelektronik ist ein vielversprechender Weg hin zu zukünftigen Konzepten der Datenspeicherung und -verarbeitung. Es wurde berichtet, dass die Hybridisierung der elektronischen Struktur von nicht-magnetischen organischen Molekülen mit den Oberflächen von ferromagnetischen Übergangsmetallen zu neuen magnetischen Einheiten, sogenannten molekularen Hybridmagneten, mit eigenen magnetischen Eigenschaften führen kann, die molekulare spinelektronische Bauteile (devices) mit extrem hoher Informationsdichte und geringem Energieverbrauch verheißen. Die Untersuchung und das tiefgreifende Verständnis dieser Bauteilkonzepte erfordern die Herstellung von sauberen und epitaktischen Grenzflächen zwischen der Oberfläche einer metallischen Elektrode und molekularen Dünnschichten. Dies kann nur im Ultrahochvakuum (UHV) realisiert werden. Zudem müssen die Elektroden auf einem isolierenden Substrat gewachsen werden, um benachbarte Bauteile und auch die einzelnen Elektroden jedes Bauteils elektrisch voneinander zu trennen.

Zu diesem Zweck wurden Verfahren zur Realisierung einer vollständigen *in-situ* Präparation von mesoskopischen Testbauteilen mit strukturell und chemisch wohldefinierten Grenzflächen untersucht und etabliert. Au(111)-gepufferte Co(0001)-Elektroden wurden mittels Molekularstrahlepitaxie auf Saphir- und Glimmersubstraten abgeschieden, wobei Schattenmasken zur Definition der Elektrodengeometrie verwendet werden. Die Oberflächenqualität wurde anschließend durch Rastertunnelmikroskopie (STM) und andere oberflächenwissenschaftliche Methoden charakterisiert. BNTCDI, das als Beispielmolekül dient, wird durch eine weitere Schattenmaske sublimiert, und die Grenzflächenbildung im Monolayer-Regime wird ebenfalls mittels STM untersucht. Sowohl für die Herstellung von Testbauteilen als auch für die Untersuchung mittels STM musste BNTCDI zunächst auf seine Sublimierbarkeit hin untersucht werden. Dazu mussten die entsprechenden Verdampfungsparameter wie Temperatur und Zeit im Zusammenhang mit Abscheiderate, Ausbeute an intakten Molekülen und Oberflächenbedeckung untersucht werden.

Um die Lücke zwischen dem Verständnis von mikroskopischen Effekten und mesoskopischen Bauelementen zu schließen, wurde BNTCDI/Co(0001)/Au(111) auch im Sub-Monolayer-Regime mit STM und STS auf die genaue Adsorptionsposition und die elektronische Wechselwirkung hin untersucht. Zu diesem Zweck wurde BNTCDI mit submolekularer Auflösung mittels STM abgebildet und ein erstes

Modell vorgeschlagen. Zur weiteren Untersuchung der Adsorptionsposition wurden die intramolekularen N-H-Bindungen, die in STM-Bildern sehr prominent sind, als Markierungspunkte innerhalb des Moleküls verwendet und ihr Leitwert mittels STS untersucht. Dabei wurde eine intramolekulare Asymmetrie festgestellt. Diese Asymmetrie wurde mit Hilfe von $\frac{\mathrm{d}I}{\mathrm{d}V}$-Karten ortsaufgelöst und energieabhängig bestätigt. Die gefundene Asymmetrie wurde auf unterschiedliche Adsorptionsstellen der N-H-Bindungen zurückgeführt und das Adsorptionsmodell wurde entsprechend angepasst.

Schließlich wurden eine nicht-magnetische Cu Elektrode und eine Deckschicht aus MgO auf den BNTCDI-Schichten abgeschieden, um ein mesoskopisches ($200\times200\,\mu\mathrm{m}^2$) Testbauteil zu realisieren, das in *ex-situ* Transportmessungen für den Co/BNTCDI/Cu-Übergang nicht-metallisches Verhalten und ein Widerstands-Flächenprodukt von $24\,\mathrm{M}\Omega\cdot\mu\mathrm{m}^2$ bei $10\,\mathrm{K}$ zeigt.

Abstract Königshofen, Samuel

The growing field of molecular spintronics is an auspicious route to future concepts of data storage and processing. It has been reported that the hybridization of the electronic structures of non-magnetic organic molecules and ferromagnetic transition-metal (TM) surfaces can form new magnetic units, so-called hybrid molecular magnets, with distinct magnetic properties, which promise molecular spintronic devices with extremely high information density and low energy consumption. The investigation and profound understanding of these device concepts require the formation of clean and epitaxial interfaces between the surface of a TM bottom electrode and molecular thin films. This can only be realized under ultra-high vacuum (UHV) conditions. In addition, the TM electrodes must be grown on an insulating substrate to electrically separate neighboring devices and also the top and bottom electrodes of each single device.

To this end procedures to realize an entirely *in-situ* preparation of mesoscopic test devices featuring structurally and chemically well-defined interfaces have been investigated and established. Au(111)-buffered Co(0001) electrodes are deposited by molecular-beam epitaxy onto sapphire and mica substrates using shadow-masks to define the electrode geometry. The surface quality is subsequently characterized by scanning tunneling microscopy (STM) and other surface science analysis tools. BNTCDI, which serves as an exemplary molecule, is sublimed through another shadow-mask, and the interface formation in the monolayer regime is also studied by STM. For both the fabrication of test devices and for the investigation by means of STM, BNTCDI first had to be examined with respect to its sublimability. For this purpose, the corresponding evaporation parameters such as temperature and time had to be investigated in connection with deposition rate, yield of intact molecules and surface coverage.

To bridge the gap between the understanding of microscopic effects and mesoscopic devices, BNTCDI/Co(0001)/Au(111) has been studied in the sub monolayer regime with both STM and STS as well, in order to determine the exact adsorption position and the electronic interaction. To this end, BNTCDI was imaged with sub-molecular

resolution by means of STM and a first model was proposed. For further analysis of the adsorption position, the intramolecular N-H bonds which are very prominent in STM images were used as marker points within the molecule and their conductance was investigated by means of STS. Here, an intramolecular asymmetry was found. This asymmetry was confirmed in a spatially resolved and energy dependent manner using $\frac{\mathrm{d}I}{\mathrm{d}V}$-maps. The asymmetry found was attributed to the different adsorption sites of the N-H bonds and the adsorption model was adjusted accordingly.

Finally, a non magnetic Cu top electrode and a capping layer of MgO have been deposited on top of the BNTCDI layers to complete a mesoscopic ($200\times200\,\mu\mathrm{m}^2$) test device, which reveals in *ex-situ* transport measurements for the Co/BNTCDI/Cu junction non-metallic behavior and a resistance-area product of $24\,\mathrm{M}\Omega\cdot\mu\mathrm{m}^2$ at $10\,\mathrm{K}$.

Contents

Chapter 1

Introduction

The demands on semiconductor technology, especially data storage and processing, have been constantly increasing since its discovery. The ever-increasing data volumes worldwide continue to grow and require a constant growth of the available technology. Up to now, the ideal solution has always been to reduce the density of transistors and memory blocks. As early as 1965, Gordon Moore made the assumption that the density within the available semiconductor technology would double approximately every 18 months[1]. This entered the general consciousness as the famous "Moore's law" and, amazingly, seemed to be confirmed again and again over decades. Obviously, however, there is a physical limit to semiconductor technology from where higher densities are not achievable. In recent years, the semiconductor industry has indeed sent signals that Moore's law will no longer be able to be complied with. Since this case was foreseeable, there are significant efforts to develop alternative technologies to push the required computing power and data storage capacity beyond the looming limit of semiconductor technology. At the same time, energy consumption should be reduced as much as possible for practical and environmental reasons, especially as the number of digital media users is growing rapidly worldwide.

Besides quantum computing the growing field of molecular spintronics [1, 2, 3] is a promising approach for future data storage and processing applications. A key feature of these concepts is to increase the density of information per unit area and to decrease energy consumption in operation. Molecular spintronics is a promising route towards using the electron spin as information carrier mainly because of the

---

[1] depending on the source the time interval spans between 12 and 24 months

weak spin-orbit and hyperfine interactions in organic molecules, which promise the preserving of the spin-coherence for much longer times and over wider distances than in metals or conventional semiconductors [2]. Besides the approach of using intrinsically magnetic molecules, so-called single molecular magnets [4, 5, 6, 7], there is an alternative route that employs the hybridization of a small non-magnetic aromatic molecule with a ferromagnetic surface. This direct interaction leads to the formation of new magnetic units at the interface, the so-called hybrid molecular magnets, that consist of the adsorbed molecule and the few substrate atoms it is bound to [8, 9, 10]. Anticipated applications of such hybrid molecular magnets and their technical realization motivate this work towards a deeper understanding of the fundamental processes and their technical feasibility likewise.

It has been shown theoretically and experimentally [11, 12, 13, 14] that hybrid molecular magnets can form upon chemisorption on Co(0001) surfaces, where the π-orbitals of the aromatic molecules hybridize with the spin-split Co $3d$-states. Therefore, well-defined and clean surfaces for the molecules to interact with are crucial. The adsorption and initial growth behavior leading to the formation of an interface with specific magnetic properties, the so-called spinterface [3], can be studied on Co(0001) single crystals. However, actual mesoscopic devices that enable (magneto-)transport measurements and operate on the basis of organic molecular layers showing spinterface effects demand an approach, where the Co(0001) surface is part of the bottom electrode of the device. Since electrodes of the same or several devices fabricated on the same substrate must be electrically separated from each other to enable individual addressability, epitaxial and laterally structured Co(0001) electrodes deposited on an insulating substrate are needed. Furthermore, the high reactivity of Co at ambient conditions, in particular the formation of carbides, oxides, and hydroxides [15, 16], makes an entirely *in-situ* preparation under ultra-high vacuum (UHV) conditions for the Co bottom electrode as well as for the subsequently deposited organic layer and top electrode mandatory.

In this work I present an entirely UHV-based preparation procedure for mesoscopic test devices comprising crossed bottom and top electrodes and an organic molecular interlayer with structurally and chemically well-defined interfaces. The potential interactions between the molecules and the ferromagnet, as chemisorption with spin-split hybridization [17], can thus be ensured. A major focus lies on the understanding of the smallest functional building block, the single molecule which chemisorbs on the ferromagnetic surface of a transition metal, and to bridge the gap between this small unit to mesoscopic devices with macroscopic evaluable effects in the context of a bottom up approach.

A large part of the investigations during this work has been carried out by scanning tunneling microscopy (STM) and scanning tunneling spectroscopy (STS). In Chapter 2 the fundamentals and the working principle of STM and STS will be described. STM and STS provide a crucial contribution to the understanding of the initial processes during the adsorption of molecules and also in the determination of substrate quality. For the targeted device, it is essential to understand which parameters are necessary to obtain the desired interface quality. STM and STS offer a deep insight into both the topographic and electronic properties. In Chapter 3 the interplay between molecules and metal substrates are discussed in the context of molecular spintronics. This serves both as an introduction to the topic and as motivation for this thesis. The effect of interface magneto resistance [9, 12] and the formation and exploitation of the so-called spinterface [13] are of particular interest in this regard. In Chapter 4, the nano spintronic cluster tool (NSCT) is presented. This comprehensive facility offers a broad arsenal of preparation and analysis tool and has been used to produce practically all samples and test devices in the course of this work. Techniques that were used supplementary in other systems are briefly outlined. Co(0001) had to be grown on Au(111) for both all molecular investigations and the fabrication of test devices and therefore is a basic requirement for the majority of experiments of this work. Hence, the preparation and investigation of as flat as possible Co(0001)/Au(111) surfaces are also described in this chapter. Chapter 5 then includes all microscopic and spectroscopic studies of the molecule used namely 2,7-dibenzyl 1,4,5,8-naphthalenetetracarboxylic diimide (BNTCDI). The molecules are considered precursor molecules and shall serve as organic tunneling barriers in the targeted test devices. For this purpose, BNTCDI was deposited on Co(0001) by sublimation and characterized by STM and STS. With respect to the fabrication of devices, the deposition parameters, the yield of intact molecules and the formation of closed layers was just as much of interest as the determination of the adsorption position and the electronic interaction between the single molecule and the substrate. Finally, in Chapter 6 the fabrication of first test devices will be presented and discussed. In the course of this work, a closed organic tunnel barrier of BNTCDI on a Co(0001) electrode was successfully fabricated and verified by transport measurements. For this purpose, some modifications of the NSCT had to be performed in order to realize a suitable electrode geometry. Co(0001) had to be grown on an insulator and suitable stacking sequences had to be found which allow epitaxial growth and subsequent *ex-situ* transport measurements likewise. There is also an error discussion which may be considered in the fabrication of future devices.

Based on these interesting and promising studies, it is worthwhile to investigate further systems of ferromagnetic substrates and organic molecules and, in the long run, even to implement different effects in devices. Therefore, in addition to the conclusion, there is also an outlook for the future in Chapter 7.

Chapter 2

Scanning Tunneling Microscopy

For ages, the examination of nature was limited by the resolution of the human eye. Optical microscopes pushed this boundary far beyond and made smaller structures, like blood cells, bacteria and chloroplasts, accessible. Yet, the optical approach has an inherent limit of resolution around a few hundreds of nanometer given by the wavelength of the used light. The Abbe diffraction limit of a microscope is

$$d = \frac{\lambda}{2n \cdot \sin\theta} = \frac{\lambda}{2\mathrm{NA}} \tag{2.1}$$

with diffraction index n, the wavelength of the used light λ, the half of the converging angle θ and the numerical aperture NA [18]. For e.g. green light and with NA= 1 the Abbe limit is therefore $d = \frac{\lambda}{2} \approx 250\,\mathrm{nm}$. This natural diffraction limit left the realm of atoms, small molecules and nanoscale surface structures veiled for centuries.

That changed dramatically since the invention of the *Scanning Tunneling Microscope* (STM) by Binnig and Rohrer in 1982 [19, 20] which were awarded the Nobel Price in physics in 1986 for this groundbreaking discovery. Since then, STM became a very important tool for the investigation of surfaces and their topographic and electronic structure as well. STM gave insight into the topography of films and surface adsorbates as well. As STM is of utmost importance for this thesis, the following chapter presents the underlying principle of both STM and *Scanning Tunneling Spectroscopy* (STS), likewise. For an overview of several applications of STM see [21, 22, 23, 24, 25].

2.1 Working Principle

Like all *Scanning Probe Microscopy* techniques, STM works technologically according to a rather simple principle. A small conducting tip e.g. tungsten (W), chromium (Cr) or platinum iridium (PtIr) is scanned laterally over the surface of interest, usually a metal, semi- or superconductor, at a defined distance so that both materials can interact. The tip is controlled by a piezoelectric circuit making the tip movement fine enough. In the case of STM said interaction is a tunneling current I_{T} based on the quantum mechanical tunnel effect [26, 27, 28] induced by a bias voltage between tip and sample U_{Bias}. Thus, using a proper distance is crucial as tunneling is extremely distance dependent. If the tip is too far away, no current flows at all. If the tip approaches to close, the tip eventually contacts the sample and the tunneling barrier is short-circuited, yielding an extremely high current compared to the tunneling current values. Typical operating distances are in the order of 0.5 to 1 nm with values of -1...1 V for the bias and tunneling currents in the low nA regime. A negative applied bias lets the electrons tunnel from sample to the tip and therefore probes the occupied states of the sample while a positive bias does the opposite and therefore probes the unoccupied states in the sample material. Note that these low bias voltage values hold for metal samples. If semiconductors such as GaN shall be imaged by STM, voltages of several V are necessary to overcome the large band gap [29, 30].

In this configuration the tip is moved by very precise piezos over the sample plane (x, y-coordinates) depending on the operating mode (cf. Sect. 2.1.1), the values for current and tip distance, respectively, are recorded with respect to the lateral tip position. The tunneling current correlates with the surface topography and thus with the distance to the tip, hence during the scan the STM tip interacts with the local density of states (LDOS) at the sample surface which is convoluted with the LDOS of the tip. A local current peak represents an increased local density of states close to the Fermi energy which is correlated to an atom close to (or at) the surface. A map of the recorded current or the regulation of the piezos in z-direction respectively is thus correlated to the LDOS of sample and tip and in first approximation using specific assumptions (detailed further below) can be interpreted as a real space image of the sample topography. For very small lateral structures with considerable height in z-direction, the convolution with the tip becomes significant as the structure may probe the tip instead of vice versa. On the other hand, the influence of the tip may be used to improve the lateral resolution, for example by selectively picking up atoms or

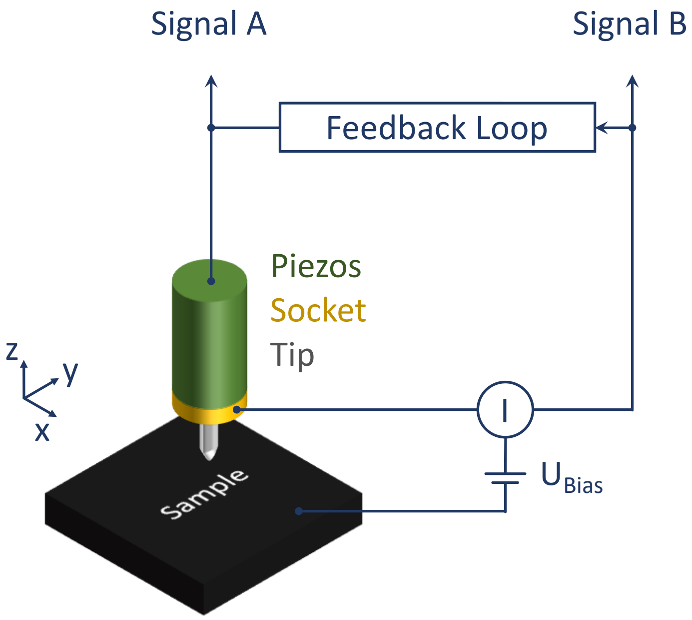

Figure 2.1: Schematic view of an STM unit. A preferably sharp conduction tip (silver) is mounted on a socket (yellow) and can be moved by a piezodrive (green) along the x, y and z axes to scan over the sample surface (black). The tunneling current I is controlled by the feedback loop. Depending on the operating mode, either the piezo signal in z direction (Signal A) or the tunneling current (Signal B) is stored.

molecules with the tip [31]. Figure 2.1 shows the schematic working principle. For a more detailed description of operating an STM see Sect. 2.1.1. In this manner, areas between a few nm^2 up to multiple μm^2 can be investigated during one scan cycle. Additionally nowadays it is also possible to probe the spin of tunneling electrons with specific magnetic tips resulting in spin-polarized STM (SP-STM) [32, 33].

2.1.1 Operating Modes

There are two basic modes to operate an STM machine with regards to imaging a samples topography[1]. In general both modes can be performed by the same setup as it just depends on which signal (cf. Fig. 2.1) is modulated and read out or to put it another way which signal is kept constant. Yet, there are advantages and disadvantages to each mode. Fig. 2.2 shows the working principle of both modes.

---

[1] STM can also perform spectroscopy and even take ”pictures” of the local conductance, see Sect. 2.3

Constant Current Mode

In constant current mode (CCM) the applied bias voltage between tip and sample U_{Bias} is defined by the operator before a measurement as well as the set-point of the desired tunneling current I_{T}. While the tip scans over the sample's surface, due to the topography and thus the sample/tip distance, changes in the tunneling current occur (detailed further below). As soon as the tunneling current drops or rises, the feedback loop in the STM re-positions the tip until I_{T} equals the defined set-point again. The re-positioning is performed with high precision piezo elements. During the whole scan, the piezo values, and thus the z-position of the tip, is recorded with respect to the tip's lateral position (x, y) and afterwards plotted on an (x, y)-map which can be interpreted as an approximation of the samples topography. An early and famous example is the revealing of the well-known Si(111) 7×7 reconstruction [34].

As mentioned before, the tunneling current does not solely depend on the z-position of the tip but also on the LDOS of the sample surface. That results in an actual measurement of the LDOS integrated over the energy interval $[E_{\mathrm{F}}; E_{\mathrm{F}} + eU_{\mathrm{Bias}}]$. This may yield ostensible contradictions, where adsorbates (topography rises) lead to a suppression of the LDOS isosurface (image drops). A common example are oxygen atoms on a metal surface. But also hydrogen on gadolinium has the same effect of inducing apparent valleys [35].

CCM has the advantage, that it is comparatively robust to changes in topography as the tip moves and has almost the same distance to the sample no matter what the surface looks like. This suggests the use of CCM for rather rough (in the broadest sense) surfaces. Yet, it has the disadvantage of being quite slow as the tip needs time to re-adjust after each image point which is usually limited by the bandwidth of the feedback loop, which is typically lower than that of the current amplifier. This mode aims for keeping the tunneling current constant, hence its name. In Fig. 2.1 that would be signal B, while signal A is recorded to image the topography. In constant height mode it is the other way around, which offers several disadvantages and advantages likewise.

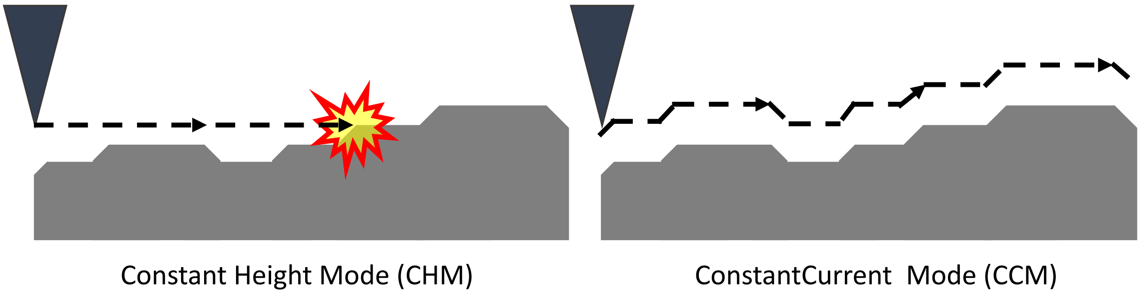

Figure 2.2: Left: Constant Height Mode allows a much faster operation yet is more likely to crash as the tip is not retracted at step edges or topographic changes. Right: In Constant Current Mode the tip is driven back and forth by the topography of the sample. Thus, it is slow in comparison. Moreover, this mode is more susceptible to vibrations due to the permanent movement of the tip.

Constant Height Mode

As the name suggests in constant height mode (CHM) the absolute z-position of the tip is kept constant during the measurement. With variations in the topography and the LDOS isosurface, I_T changes according accordingly and the current values are recorded with respect to their (x, y)-image points. That allows to scan rather quickly as no re-adjusting in the feedback loop happens and the current can be recorded directly. Furthermore the tip tends to stay smoother because no vibrations are induced by the adjustment of the piezos. Then again, CHM is not advisable for rough or generally unknown surfaces as the tip can not respond to steep risings or valleys which would result in a crash or the loss of tunneling contact, respectively. On top of that CHM is very sensitive to thermal drift and creep of the piezo elements making it the mode of choice only for very certain situations, e.g. atomically flat surface areas as even small step edges may lead to a crash of the tip. Its reasonable to say, that CCM is somewhat the standard route and most of the time the mode of choice in practice.

2.1.2 The Tip in Practice

As will be discussed in more detail in Sect. 2.2, STM measurements are extremely sensitive to both the distance between tip and sample and the exact geometry of the tip. In practice this means that a lot of effort has to be put into tip preparation, switching and modulation between and during measurements. Typical *in-situ* tip treatment procedures are heat treatment, picking up atoms from the sample, Ar-ion sputtering and voltage pulsing [31]. Still after any of this treatments, the exact tip configuration remains unknown so one has to decide during a measurement if the tip works sufficiently or not. To some extent the tip is examinable with *Scanning Electron Microscopy* (SEM). Nevertheless, this technique does not reveal the atomic composition at the extreme end of the tip. Furthermore in practice the tip tends to change during several measurements depending on scan speed, applied bias voltage and sample structure. This makes *tip handling* a big challenge and a serious part of STM investigators work and experience.

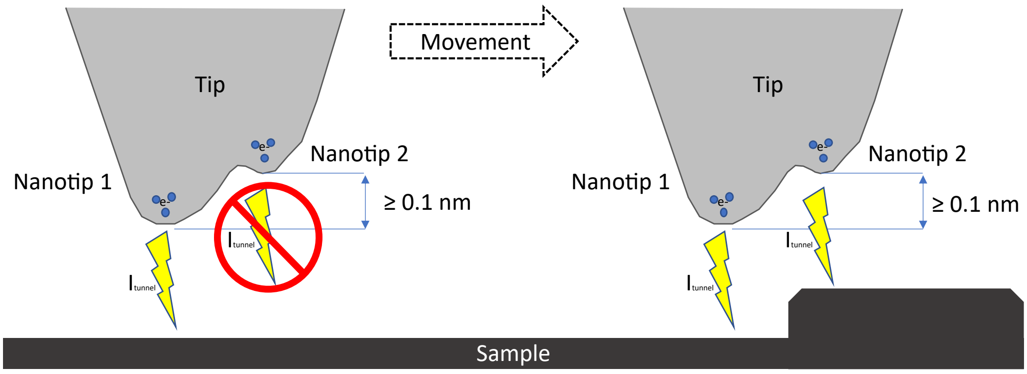

Figure 2.3: As the tunneling current is extremely distance dependent, nanotips are particularly apparent at step edges or other topographic changes. In the area of the step edge, the distance between the sample surface and nanotip 2 is small enough to carry a significant tunneling current. Or in other words, the height of the step edge is bigger than the difference in height between nanotip 1 and nanotip 2. Thus, in the processed image there are duplications of the step edge.

On the other hand, the strong distance dependency of the tunneling current yields an excellent resolution in z-direction since even the smallest changes are detectable. The strong distance dependency delivers another advantage to STM. As mentioned before, a lot of effort is generally put into tip preparation to get a well defined tip. At nanoscale the actual tip remains generally unknown and consists of a fragmented conglomerate of peaks and valleys. This especially holds for a tip which has been in use for a while and underwent possible crashes and fast changes in direction. Yet, it is unlikely to have several of such peaks, so-called nanotips, with the very same distance to the sample. This often leads to a predominant nanotip (see nanotip 1 in Fig. 2.3), which is the actual conductor path where tunneling occurs predominantly and therefore can be considered as the actual tip of the STM. Nevertheless in practice one has to deal regularly with so-called double tips, which occur if the difference in height (measured normal to the lateral sample plane) falls below a value of $\approx 0.1\,\text{nm}$. Due to the exponential dependence of the transmission factor (cf. Eq. 2.10 in Sect. 2.2) the tunneling current from more remote nanotips is no longer negligible. This happens particularly at step edges or islands (cf. Fig. 2.3). Figure 2.4 shows a STM topography measurement of Co(0001) grown on Au(111) with a very pronounced double tip which causes certain features on the image to appear duplicated and offset.

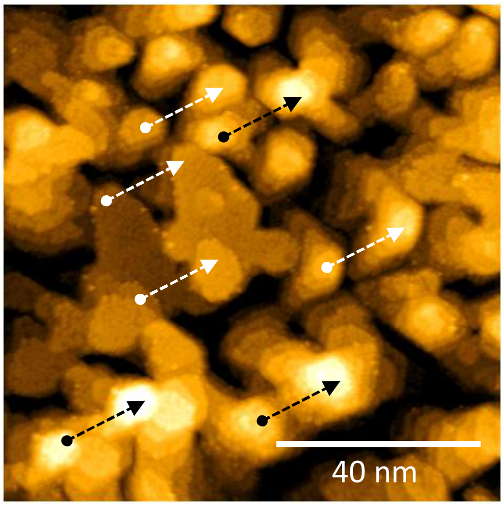

Figure 2.4: STM of Co(0001) grown on Au(111) covered with ≈ 1 monolayer of BNTCDI molecules. The arrows connect positions which appear duplicated and offset due to a double tip. ($100 \times 100\,\mathrm{nm}^2$, $V_{\mathrm{gap}} = 0.3\,\mathrm{V}$, $I = 0.5\,\mathrm{nA}$)

Finally, the strong distance dependence of the tunneling current improves the lateral resolution of STM as the foremost atom contributes most to the measured tunneling current and even tips that look completely bent, blunt or destroyed at first glance may actually deliver excellent results.

2.2 Theoretical Fundamentals

As mentioned above STM does not produce an image solely of the topography but rather creates a map of the surface structure of a sample (including contributions of the tip, the surface composition and adsorbates). In reality STM is mostly performed under vacuum conditions[2], so that the electrons must tunnel through a vacuum gap, i.e. a potential barrier, between the corresponding electrical states of the tip and the sample material. The probability of an electron to penetrate this barrier

---

[2] There are also STMs that are operated in air or in liquids, but clean surfaces on the atomic level can only be obtained in UHV.

decreases exponentially with the barrier width, hence the small distance between tip and sample. That also means that interpreting the gained data is not trivial and a sufficient underlying theory has to be applied. In the following sections the theoretical fundamentals of STM and STS will be presented, essentially based on Chen [31].

2.2.1 One Dimensional Tunneling

A first way to approach the basic physics of STM is the one dimensional tunneling effect at a quantum mechanical potential barrier [31]. Be the potential of the form:

$$V(z) = \begin{cases} V_0 > 0 & \text{for } 0 < z < d \\ 0 & \text{else .} \end{cases} \tag{2.2}$$

In the picture of classical mechanics, an electron with mass m and energy E is described by $\frac{p^2}{2m} + V(z) = E$. Therefore the particle with $E > V_0$ can traverse the potential barrier, while a particle with $E \leq V_0$ cannot, but will be reflected instead (cf. brown arrow in Fig. 2.5). There is zero probability for such an electron to penetrate from region I into region II (the barrier region). In the case of STM, the barrier thickness d can be associated with the distance between the tip and the sample surface, while the barrier height V_0 corresponds to the work function ϕ of the sample material.

As STM is a technique that makes use of electrons probing very small structures, one leaves the classical picture and has to take the quantum mechanical nature of particles into account, introducing the wave-particle duality [36]. In quantum mechanics, the same electron is described by a wave function $\psi(z)$ in the Schrödinger equation:

$$\left[-\frac{\hbar^2}{2m}\frac{d^2}{dz^2} + V(z) \right] \psi(z) = E\psi(z) \tag{2.3}$$

which has a solution depending on the region I, II or III (cf. Fig. 2.5):

$$\psi_{\mathrm{I}}(z) = Ae^{ikz} + Be^{-ikz} \tag{2.4}$$

$$\psi_{\mathrm{II}}(z) = Ce^{\kappa z} + De^{-\kappa z} \tag{2.5}$$

$$\psi_{\mathrm{III}}(z) = Ee^{ikz} \tag{2.6}$$

with the wave vector

$$k = \frac{\sqrt{2mE}}{\hbar}. \tag{2.7}$$

and the decay constant

$$\kappa = \frac{\sqrt{2m(V_0 - E)}}{\hbar}. \tag{2.8}$$

The electron moves with constant momentum $p = \hbar k$ or in the classical picture with $v = \frac{p}{m}$ from left to right in region I. Note that $\psi_{\mathrm{I}}(z)$ is complex and oscillates (cf. green arrows in Fig. 2.5). There is a certain probability for the electron to be reflected at $z = 0$ as well (cf. dotted line in Fig. 2.5) indicated by the second summand in the solution with negative exponent.

The decisive difference, however, lies in the area in which the classical particle can not penetrate, i.e. the barrier (region II). Since $\psi_{\mathrm{II}}(z)$ has a non zero value for $E < V_0$ there is a certain probability $|\psi_{\mathrm{II}}(z)|^2 > 0$ to observe the electron within region II. Interestingly enough that also means that there is a certain probability for an electron with $E > V_0$ to be reflected although its energy E exceeds the barrier height V_0. Unlike $\psi_{\mathrm{I}}(z)$ the solution $\psi_{\mathrm{II}}(z)$ is real and does not oscillate but is damped while penetrating into region II.

Finally, $\psi_{\mathrm{III}}(z)$ is complex again and oscillates. As region III is infinite in the example at hand, there is no reflected fraction of waves contributing to the wave function $\psi_{\mathrm{III}}(z)$ as opposed to $\psi_{\mathrm{I}}(z)$ and $\psi_{\mathrm{II}}(z)$.

The coefficients A, B, C, D can be derived from boundary conditions $\psi(0), \psi(d)$ and continuity considerations. A transmission coefficient T may be considered as the

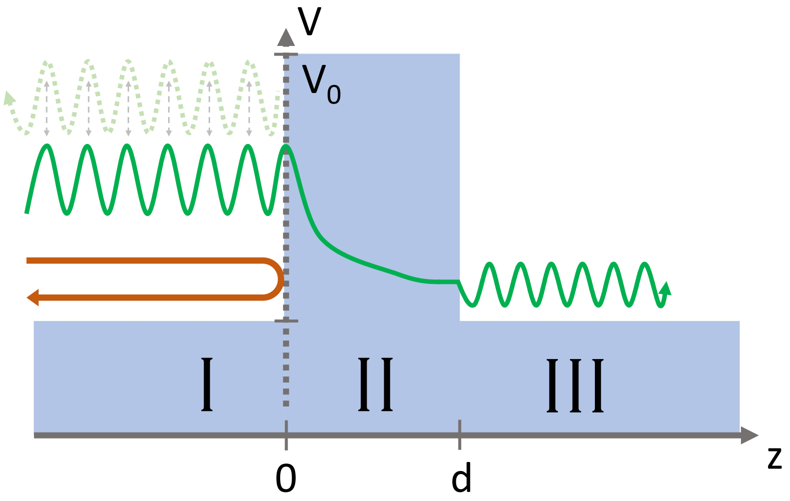

Figure 2.5: Two particles are coming with constant momentum from region I. The classical particle (brown) with $E < V_0$ can not traverse the potential barrier $0 < z < d$ with height V_0 into region II but is reflected instead. The quantum mechanical particle (green) with $E < V_0$ has a probability $T > 0$ to pass the barrier into region II and penetrate into region III. The reflected portion of the quantum mechanical waves are depicted by the dotted light green arrow, which is shifted (transparent gray arrows) for the sake of readability.

ratio of the transmitted electrons probability flux to the probability flux of the impinging electrons and can be written as:

$$T = \frac{1}{1 + (k^2 + \kappa^2)^2 / 4k^2\kappa^2 \sinh \kappa d} \tag{2.9}$$

Assuming a wide and high potential barrier ($\kappa d \gg 1$) as it is common in STM applications Eq. 2.9 can be approximated by:

$$T \approx \frac{16k^2\kappa^2}{(k^2 + \kappa^2)^2} e^{-2\kappa d} \tag{2.10}$$

which reveals a strong dependency of the transmitted electrons (and therefore the current) on the barrier width d [37].

In other words, from a quantum mechanical point of view a particle, e.g. an electron, may penetrate the potential barrier, e.g. a vacuum gap, which it can not within classical mechanics. In this case it *tunnels* through the barrier. The probability to tunnel through the barrier is strongly dependent on the barrier width (e.g. the distance between sample and tip). Applying the considerations made above to STM, that means that if a voltage V_{Bias} is applied between tip and sample, there will be a net current through the vacuum gap which corresponds to the barrier in the picture above. The net current is heavily dependent on the distance d which results in an excellent resolution of STM in particular normal to the sample surface. As a rule of thumb the current decreases in the order of a magnitude when the distance d increases by 1 Å. On the other hand, this makes STM extremely error-prone for tip changes.

Yet, this model is a glaring simplification, since the electronic structure of the sample and tip material are neglected likewise. Thus, we are in the need of a better approximation.

2.2.2 Bardeen's Perturbation Theory Approach

One possible approach to improve the model described above was established by Bardeen et al. and was developed to describe the tunneling process between to electrodes in metal-insulator-metal junctions [38]. The basic idea is to use two separate opposing wave functions each corresponding to one electrode and to examine their behavior when the electrodes are approaching each other.

In an initial state when the electrodes are still distant, the wave functions of each electrode (A, B) satisfy the stationary Schrödinger equation with its own separated spatial wave functions ψ_μ for electrode A and χ_ν for electrode B reaching into the vacuum. When the two electrodes are brought closer together, the Schrödinger equation of the combined system is

$$i\hbar\frac{\partial\Psi}{\partial t} = \left[-\frac{\hbar^2}{2m}\frac{\partial^2}{\partial z^2} + V_A + V_B \right]\Psi \tag{2.11}$$

with the potential functions of each electrode $V_{A,B}$ and the stationary states Ψ. Due to the combined potential of both electrodes, the wave functions ψ_μ and χ_ν do not evolve as in the separated systems but may be transferred to the states of the opposing electrode. Thus, both wave functions fulfill the Schrödinger equation with different Hamiltonians and neither of both is an eigenfunction of the Hamiltonian of the combined system. Therefore Bardeen assumed

$$\Psi = \psi_\mu e^{-E_\mu t/\hbar} + \sum_{\nu=1}^{\infty} c_\nu(t)\chi_\nu e^{-E_\mu t/\hbar} \tag{2.12}$$

for the wave function Ψ with coefficients $c_\nu(t)$ to be determined from continuity conditions of Eq. 2.11. By inserting Eq. 2.12 into Eq. 2.11 one can derive a *tunneling matrix element*

$$M_{\mu\nu} = \int \psi_\mu V_B \chi_\nu^* d^3\mathbf{r} \tag{2.13}$$

which can be developed further to

$$M_{\mu\nu} = \frac{\hbar^2}{2m}\int \left[\psi_\mu \frac{\partial \chi_\nu^*}{\partial z} - \chi_\nu^* \frac{\partial \psi_\mu}{\partial z}\right] dxdy \tag{2.14}$$

as an explicit expression of the tunneling current in the one dimensional case and

$$M_{\mu\nu} = \frac{\hbar^2}{2m}\int_\Sigma (\psi_\mu \nabla \chi_\nu^* - \chi_\nu^* \nabla \psi_\mu) d\mathbf{S} \tag{2.15}$$

for the three dimensional case with the tunneling matrix element being a surface integral on the separation surface Σ. Note that Eq. 2.15 does not contain the potential functions of the electrodes explicitly. Since the wave functions are eigenfunctions of the separated Schrödinger equations of the electrodes, the potentials V_A, V_B of the electrodes are nevertheless incorporated into Eq. 2.15.

Given a particular bias voltage V between the electrodes, the tunneling current I in the energy interval may be calculated for low temperatures by integrating over the corresponding states

$$I = \frac{4\pi e}{\hbar} \int_0^{eV} \rho_A(E_F - eV + \epsilon)\rho_B(E_F + \epsilon)|M_{\mu\nu}|^2 d\epsilon \tag{2.16}$$

with the density of states (DOS) $\rho_{A,B}$ of electrode A and electrode B. Considering the electrodes in a STM machine are the tip and the sample and assuming $|M_{\mu\nu}|$ being constant over the particular energy interval, Eq. 2.16 yields that the tunneling current is proportional to the convolution of the DOS of the tip ρ_{tip} and the sample ρ_{sample}:

$$I \propto \int_0^{\infty} \rho_{\text{tip}}(E_F - eV + \epsilon)\rho_{\text{sample}}(E_F + \epsilon) d\epsilon. \tag{2.17}$$

Since the tunneling matrix in a STM is heavily dependent on both the surface topography and geometry of the tip, it is basically unknown in practice as the exact apex of the measuring tip is not accessible during the measurement.

To this end, Tersoff and Hamann have further developed Bardeen's theory by modeling the tip of the STM by a single atom with a single s-orbital which shows no energy dependence for small bias voltages. The spherical s-orbital of the single atom has a radius r with its center at $\mathbf{r}_0$, while the sample surface is represented by a plane at $z = 0$ and the center of the spherical potential is at $(0, 0, z_0)$ [39, 40]. In the region between the tip and the sample the wave functions of both the tip ψ and the sample χ satisfy the Schrödinger equation and Tersoff and Hamann showed, that for the corresponding tunneling matrix element is up to a constant the value of the sample wavefunction at the center of the sphere $\mathbf{r}_0$:

$$M \propto \psi(\mathbf{r}_0). \tag{2.18}$$

Close to the Fermi level the tunneling current for a tip at $\mathbf{r}_0$ can be expressed in terms of a tunneling *conductance*

$$G \equiv \frac{I}{V} \propto |\psi(\mathbf{r}_0)|^2 \rho_{\text{sample}}(E_F). \tag{2.19}$$

That means that G is proportional to the local density of states (LDOS) of the sample at the Fermi level at the center of the spherical tip. That means one can also write

$$G \equiv \frac{I}{V} \propto \rho_{\text{sample}}(E_F, \mathbf{r}_0) \tag{2.20}$$

or

$$I \propto V \cdot \rho_{\text{sample}}(E_F, \mathbf{r}_0) \tag{2.21}$$

which means that the tunneling current is merely proportional to the LDOS of the sample surface ρ_{sample} but not of the tip. Thus a STM image can be interpreted as a map of an isosurface of the samples LDOS at the Fermi level. The Tersoff-Hamann model is therefore capable of explaining measurements with nanometer-scale resolution if the electronic corrugation is high enough to resolve ρ_{sample} appreciably.

The Tersoff-Hamann model has its limitations though as for feature sizes of the order of 0.3 nm and smaller other tip wave functions than the s-wave might have a significant influence on the tunneling current. The predictions of the Tersoff-Hamann model might therefor not align with the actual measured images in the atomic-scale regime. The typical nearest-neighbor distance between metallic surface atoms is about 0.2-0.3 nm though. The close-packed Au(111) surface was already imaged with atomic resolution in 1983 at Stanford university and has been discussed extensively later [41, 42, 43]. This means that the tip states cannot be neglected at such high resolutions. In particular, the sharp *d*-states of typical tip materials like tungsten play a crucial role in explaining atomic resolutions [31].

2.3 Scanning Tunneling Spectroscopy

Besides the imaging of the topography of a sample in real space, an STM apparatus can be used to probe the local conductance which corresponds within approximations to the LDOS. Scanning tunneling spectroscopy (STS) investigates the differential conductance of a sample's surface $\frac{dI}{dU}$. At a certain data point (x, y) the tip is approached and the voltage is varied, while the resulting current is measured ($I(U)$ for point spectroscopy). Thus, a characteristic curve can be recorded for each data point by differentiating the measured current with respect to the applied voltage. Interestingly enough, originally the STM was build to perform tunneling spectroscopy locally on an area with a diameter of a few nanometer [44]. In the following, the fundamental principles of scanning tunneling spectroscopy will be discussed.

Following Bardeen's approach, Eq. 2.17 implies that the tunneling current is proportional to the convolution of the DOS of the tip and the sample close to the Fermi level. Under the assumptions of Tersoff-Hamann, particularly the independence of the tunneling matrix element and the tip DOS from the energy level, Eq. 2.16 can be written as

$$\begin{aligned} I &= \frac{4\pi e}{\hbar}\int_0^{eV} \rho_{\text{ tip}}(E_F - eV + \epsilon)\rho_{\text{sample}}(E_F + \epsilon)|M|^2 d\epsilon \\ &\approx \frac{4\pi e}{\hbar}\rho_{\text{ tip}}|M^2|\int_0^{eV} \rho_{\text{sample}}(E_F + \epsilon) d\epsilon \end{aligned} \tag{2.22}$$

and with Eq. 2.18 and Eq. 2.21 the tunneling current is proportional to

$$I \propto \int_0^{eV} \rho_{\text{sample}}(E_F + \epsilon, \mathbf{r}_0) d\epsilon \tag{2.23}$$

which means that the *differential tunneling conductance* at a certain bias voltage V_{bias} is proportional to

$$\left.\frac{\mathrm{d}I}{\mathrm{d}V}\right|_{V=V_{\text{bias}}} \propto \rho_{\text{sample}}(E_F + eV_{\text{bias}}, \mathbf{r}_0) d\epsilon. \tag{2.24}$$

From Eq. 2.24 one can deduce that by measuring the tunneling current as a function of V, the LDOS of the sample at a certain position ρ_s is directly accessible. Yet this assumption is restricted to small bias voltages. Ukraintsev [45] showed that this assumption also holds for a broader energy range by introducing a transmission coefficient $T(E, V, S)$ into Eq. 2.17 which can be approximated for a trapezoidal barrier by using the Wentzel-Kramers-Brillouin (WKB) approximation:

$$T(E,V,S) \backsimeq \exp\left\{ -2S\left[\frac{2m}{\hbar^2}\left(\frac{\Phi_\mathrm{tip}+\Phi_\mathrm{sample}}{2}+\frac{eV}{2}-(E-E_{||})\right)\right]^{1/2}\right\}. \quad (2.25)$$

with the corresponding work functions Φ_tip, Φ_sample, the tip-surface separation S and the parallel component of the electron energy between the tip and the sample $E_{||}$. With Eq. 2.25 and Eq. 2.17 the conductance is proportional to [45]:

$$\begin{aligned}\frac{\mathrm{d}I(V,S)}{\mathrm{d}V} &\propto \rho_\mathrm{sample}(E_F-eV)\rho_\mathrm{tip}(E_F)T(eV,V,S)\\ &+\int_0^{eV}\rho_\mathrm{tip}(E_F+\epsilon)\rho_\mathrm{sample}(E_F-eV+\epsilon)\frac{\mathrm{d}}{\mathrm{d}V}T(\epsilon,V,S)d\epsilon \\ &+\int_0^{eV}\rho_\mathrm{tip}(E_F+\epsilon)T(\epsilon,V,S)\frac{\mathrm{d}}{\mathrm{d}V}\rho_\mathrm{sample}(E_F-eV+\epsilon)d\epsilon\end{aligned} \quad (2.26)$$

Under the assumption of a constant tip DOS and a constant transmission (cf. Tersoff-Hamann assumptions) Eq. 2.26 may be simplified to

$$\frac{\mathrm{d}I(V,S)}{\mathrm{d}V} \propto \rho_\mathrm{sample}(E_F-eV) \quad (2.27)$$

which is not restricted to small bias voltages anymore. From Eq. 2.27 one can conclude, that the conductance measured with STS gives insight directly into the LDOS of the sample surface.

Experimentally the conductance can be measured by using a lock-in amplifier and by applying an additional small high frequency (ωt) modulation voltage V_mod [46, 47].

The resulting tunneling current can be approximated by a Taylor series as follows:

$$I(V_{\mathrm{bias}}+V_{\mathrm{mod}}\cos(\omega t)) \approx I(V_{\mathrm{bias}})+\frac{\mathrm{d}I(V_{\mathrm{bias}})}{\mathrm{d}V}V_{\mathrm{mod}}\cos(\omega t)+\frac{\mathrm{d}^2I(V_{\mathrm{bias}})}{2\mathrm{d}V^2}V_{\mathrm{mod}}^2\cos(\omega t)^2+... \tag{2.28}$$

Both the modulation voltage and the temperature have an influence on the energy resolution of the performed measurements. The influence of the modulation voltage on the topography is removed from the measured signal by means of a low pass filter. At high temperatures the states broaden up so that STS measurements deliver reasonable energy resolutions only at very low temperatures. Assuming liquid Helium cooling at about 4.2 K, as it is used during all STS measurements in this work, the typical achievable energy resolution is in the range of $\Delta E = 1.3\,\mathrm{meV}$ [48]. In this manner the resulting curve delivers the local conductance of the sample at a certain position of the sample at a certain energy $E = eV_{\mathrm{bias}}$.

The results are spectra as shown in Fig. 2.6(a). While the evaluation of molecular spectra is a subject of Chapter 5, here I refer exemplary to the red spectrum recorded at the position indicated by the red marker in the STM topography image of Fig. 2.6(b). The STM shows a small section of a test sample fabricated on the way to closed layers of BNTCDI molecules (see Chapter 5) deposited on epitaxial Co(0001) layers grown on Au(111) single crystals (see. Sect. 4.3) and shows several molecular fragments on a Co(0001) mesa. The red spectrum was recorded on bare Co(0001) and is the only spectrum that has the characteristic Co 3*d* peak at -450 mV (see marking in (a); for discussion see Sect. 5.3). The other spectra which do not show this feature at this very energy indicate that the LDOS at these positions differ from the LDOS of the bare Co(0001) surface. This allows conclusions to be drawn about the surface composition and electronic structure of adsorbates. Thus, STS is a powerful tool for surface analysis.

Another application is the creation of $\frac{dI}{dV}$-maps. In this mode a constant voltage is applied. Then the measuring area is scanned, while the differential conductance is measured at each point. In this manner an STM apparatus can perform measurements of the differential conductance $\frac{dI}{dV}$ as a function of the lateral position of the STM tip and thus create maps, similar to the topographic maps. In contrast to the topographic maps, information on the energy dependent LDOS ρ_{sample} can be mapped as $\rho_{\mathrm{sample}}(E, x, y)$ with (x, y) being the image point and accordingly the tip

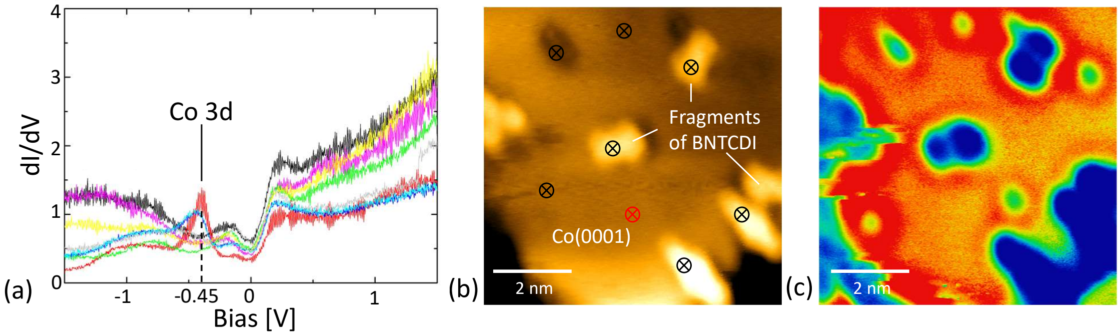

Figure 2.6: (a) STS spectra taken at the positions indicated in (b). The red spectrum corresponds to the red marking in the topography and shows a Co $3d$ surface state at -450 mV ($V_{\text{mod}} = 20$ mV). (b) STM of Co(0001) grown on Au(111) with adsorbed BNTCDI molecules and fragments thereof and marked positions of the spectra shown in (a). ($7.5 \times 7.5\,\text{nm}^2$, $V_{\text{gap}} = 1.0$ V, $I = 1.0$ nA). (c) $\frac{dI}{dU}$-map taken with -450 mV (cf. Co $3d$ peak) at the same position as the topography image. The conductance on the Co(0001) areas is significantly higher at this energy level than on the molecular fragments.

position and $E = eV_{\text{bias}}$ the fixed energy where the conductance is measured.

To distinguish the resulting maps from topographic STM images, the data points are often plotted with a different color scale with high contrast as shown in the exemplary $\frac{dI}{dV}$-map in Fig. 2.6(c) which has been taken at the same time and on the same position as the topography image of (b). The set bias voltage $V_{\text{bias}} = -450$ mV was chosen to match with the Co $3d$ peak of the red spectrum in (a). It shows clearly that the conductance at this energy is spatially dependent and is high (red) in the areas of bare cobalt and considerably lower (blue) on the molecules or the fragments, respectively. Hence, $\frac{dI}{dV}$-maps have the advantage to be not dependent on the exact position of the tip as the whole area of interest can be mapped. This advantage will be highly relevant for the results of Chapter 5.

Besides the method with a fixed bias V_{bias}, where $\frac{dI}{dV}$ is mapped with respect to the lateral position of the tip (x, y) and $\frac{dI}{dV}\big|_{V=V_{\text{bias}}}$ can be measured directly but is restricted to the predefined energy $E = V_{\text{bias}}$, one can also perform full spectroscopy cycles at each position (x, y). The first and most common mode delivers a spatially high resolved $\frac{dI}{dV}$-map and the corresponding topographic map at once. Typical measurement times are between a few minutes and several hours depending on the scan speed, the resolution and the size of scanned area. That again demands a very high stability of the tip and makes very low temperatures mandatory. Usually $\frac{dI}{dV}$-maps are taken at LHe-temperatures which have to be kept constant for the time of the scan, preferably without touching the apparatus which can be challenging. If the cooling section of the apparatus has to be refilled, the induced mechanical vibrations of the chamber may significantly interfere with the measurement. On the other hand, if the apparatus or the sample heat up thermal drift may thermal drift may become too intense and significantly interfere with the measurement or render it unusable. The heat emission of additional external consumers or an unexpected crash of the tip and a resulting change of the tip are further obstacles on the way to the generation of clean and useful $\frac{dI}{dV}$-maps. That makes STS a time-consuming but very powerful analysis tool. This is even more true for the second mode mentioned with a full spectroscopy scan at every single data point (x, y) which delivers a full set of spectroscopy data for a certain region of interest. Obviously enough, these measurements take even longer than the measurements at a fixed energy and can take up to several days. Thus the demands on stability of the microscope are even higher.

Chapter 3

Molecules on Metal

To outline the motivation for this work and to introduce the underlying concepts, in the following sections a brief introduction to spintronics will be given and the motivation and the route to molecular spintronics will be outlined.

3.1 Spintronics

When Albert Fert [49] and Peter Grünberg [50], simultaneously but independently from each other, discovered the phenomenon of Giant Magnetroresistance (GMR) in 1988, they laid the basis for a quantum leap forward in information storage technology. This achievement defines a cornerstone in what we call spintronics today. In 2007 both were awarded the nobel prize for their discovery. The basic concept of spintronics relies on making use not only of the charge of an electron as information carrier but also of its spin.

Today there are many commercially available spintronic devices making use of the above mentioned advantages. Examples are the non volatile data storage like magnetoresistive random access memory (MRAM), which write and read data by spin transfer torque (STT) and tunneling magnetoresistance (TMR), respectively, and most established the hard disc read heads which are based on the GMR effect discovered by Grünberg and Fert.

A major obstacle by the building spintronic devices is the generation of a spin polarized current. Thus, magnetic metals are an obvious material choice, due to their spin imbalance at or close to the Fermi edge and thus the conduction electrons. To circumvent this necessity a lot of techniques have been investigated in the past. With regard to generate spin polarized currents in non-magnetic materials, optical pumping is a common method. Other notable methods are the excitation by micro waves [51, 52] and the exploitation of the spin Hall effect [53].

As the demands on storage capacity, energy efficiency and processing power are continuously increasing, scientists are constantly in search of concepts that push the boundaries of scientific and technological knowledge. An auspicious route for further improvement in both is to implement molecules as small units into spintronic systems and devices. The big advantage is that molecules are small, rather controllable units, whose electronic and magnetic properties can be designed by chemists with respect to the specific needs of a envisioned application. This molecular spintronic concept motivates both fundamental research and applied science.

3.2 Molecular Orbital Theory

Before I discuss on the benefits of introducing molecules into spintronics it is necessary to understand the basic principles of the electronic properties of molecules.

In general these properties are defined by the wave functions of the electrons belonging to the atoms the molecule consists of. Coming from an atomic physics perspective the atomic orbitals don't solely add up in a molecule resulting in the sum of all atomic orbitals. Beside the valence bond theory [54], the molecular orbital theory (MO) is the common way to understand and describe molecular orbitals. Here electrons are not considered to be localized in individual bonds between the molecule's atoms but are delocalized and can travel within the whole molecule under the influence of the nuclei. The states of the bonded electrons forming the molecular orbital are approximated as linear combinations of the atomic orbitals (LCAO) [55]. The approximated orbitals can be numerically calculated by applying suitable models e.g. density functional theory (DFT) to the Schrödinger equation.

In LCAO the set of molecular orbitals are modeled considering the wave functions of each orbital ψ_j can be described with the weighted sum of the orbitals of the contributing atoms χ_i. Assuming there are n contributing atoms the wave functions of the corresponding molecular orbitals can be written as the combination $\psi_j = \sum_{i=1}^{n} c_{ij}\chi_i$ where c_{ij} are the coefficients which have to be determined numerically for example by above mentioned DFT. Other suitable methods inlcude the Hartree-Fock method, Quantum Monte Carlo or Møller-Plesset Pertubation Theory.

While approximating molecular orbitals as a linear combination of atomic orbitals it is assumed that these orbitals arise from the bonds between the contributing atoms. Usually one distinguishes between three types of bonds to wit bonding, antibonding and non-bonding [56]. In this picture the electron wave functions of two atoms ψ_1, ψ_2 can form a singlet state (ψ_1-ψ_2) where the energy of the resulting molecular orbital is lower than the energy of the two contributors solely and thus giving it the bonding character. In this scenario the charge density between the two atoms is increased, so that such an orbital refers mainly to the electrons between the atoms.

On the other hand the atoms can form a triplet state (ψ_1+ψ_2), wherein the energy is higher than the energy of the corresponding single atom state and is therefore considered as antibonding. This orbital refers mainly to the electrons "behind" the atoms with respect to each other. Figure 3.1 shows an according molecular orbital diagram for the exemplary case of the H_2 molecule. Here it becomes apparent that rising the energy in an H_2 molecule results in the dissociation of the molecule into separated atoms and furthermore that hydrogen in gas phase forms (diatomic) molecules. In molecular orbital theory all electrons are considered to be delocalized. All electrons can be anywhere whithin the molecule as long as they stay in permitted eigenstates. Thus, an electron in a molecular orbital with lower energy can be transferred into a higher energy orbital when excited with sufficient energy, e.g. by UV-light. In the example of Fig. 3.1 the antibonding orbital is higher in energy. So when exited into this orbital the molecule dissolves. That procedure is called photo-dissociation and is a standard technique if "atomic" hydrogen is demanded in certain experiments. As the name suggests, non bonding orbitals refer to electrons in atomic orbitals which don't contribute to a bond or antibond respectively. Furthermore molecule must have as many molecular orbitals as there are atomic orbitals. For example two hydrogen atoms with an 1s orbital each form two molecular orbitals when forming a molecule, one bonding σ_{1s} and one antibonding orbital σ^*_{1s}.

The nomenclature of molecular orbitals refers to their symmetry. If the resulting molecular orbital is symmetric with respect to rotation around the internuclear axis, it is called a σ-orbital. If the σ-orbital has a bonding character it has no nodal plane, while when its of antibonding nature it has one perpendicular to the internuclear axis. In the example of H_2, the σ-orbitals originate from two overlapping 1s orbitals, but any other combination of orbitals can form σ-orbitals as long as it fulfills the

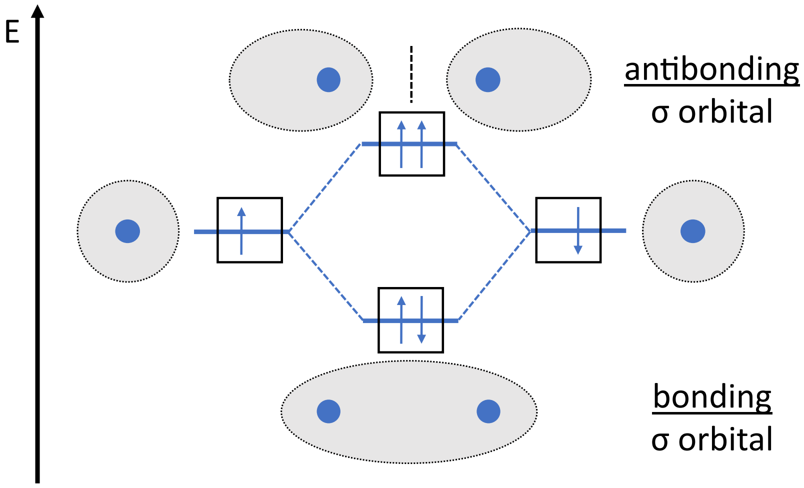

Figure 3.1: Energy diagram of two hydrogen atoms and the corresponding bonding and antibonding molecular orbitals. The bonding orbital is lower in energy than the level of the single atoms. The oval circle around the two nuclei in the bonding case represents the charge density which is increased between the atoms. In the antibonding case the charge density is reduced between the nuclei leading to a dissociation of the molecule. The dashed line represents the nodal plane and the black squares represent the respective electron configuration.

symmetry condition mentioned above. On the other hand, molecular orbitals which don't fulfill this condition are called π-orbitals. In this case, the bonding orbitals have one nodal plane, whereas the corresponding antibonding orbital has two nodal planes. One is along and one is perpendicular to the internuclear axis. Figure 3.2 shows the formation of the π-orbitals in the case of benzene (C_6H_6). The lowest-energy orbital shows the delocalized π-system formed by the six p_z atomic orbitals of the carbon atoms. The σ-orbitals (not shown) are formed by the hybridized sp^2 orbitals between the carbon atoms along the internuclear axis. With increasing energy, the orbitals get more separated by nodal planes. The dashed line separates bonding and antibonding orbitals. The orbital with the highest energy which is populated with electrons is called the highest occupied molecular orbital (HOMO), whereas the orbital with the lowest energy which is not populated is called the lowest unoccupied molecular orbital (LUMO). In this picture another important consequence for STM experiments becomes apparent. While the σ-orbitals are located in the plane of the molecule, the π-orbitals reach out into the vacuum perpendicular to the molecular plane. Thus in STM experiments the tip usually probes the π-orbitals rather than the σ-states as these contribute less to the tunneling current. Additionally it has to be stressed, that molecular orbitals are discrete in energy similar to (single) atomic orbitals. In contrast, bulk materials like metals have a continuous band-like energy distribution. Combining these to different characteristics yields many interesting (and useful) consequences, as will be come apparent in the following chapters.

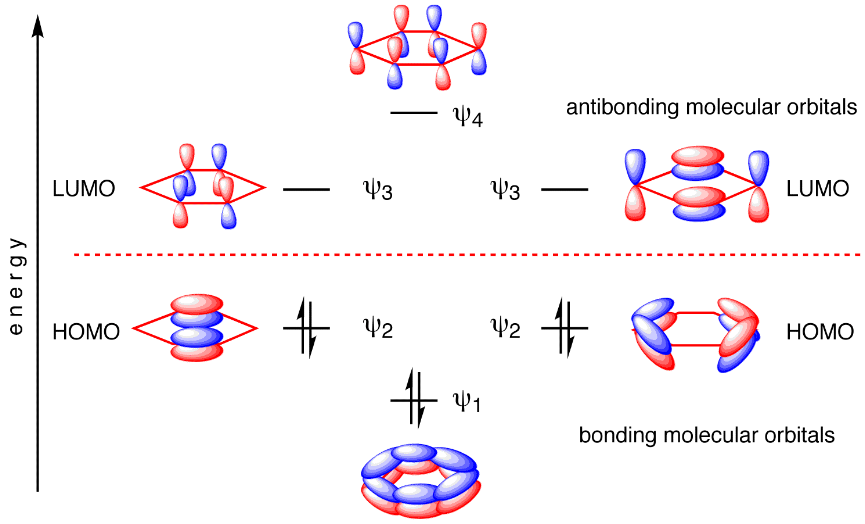

Figure 3.2: The molecular orbitals of a benzene ring. The dashed line represents the transition between bonding and antibonding orbitals which is also the border between the HOMO and the LUMO. Taken from [57]

3.3 Molecular Spintronics

In order to push the boundaries of conventional spintronics a lot of effort has been put into research of the uprising field of molecular spintronics. As mentioned above the usage of molecules as small information units are a promising route to increase information density and decrease energy consumption likewise. To that purpose, molecules can be tailored by chemists according to the needs of a prospective applications in regard to size, stability, electronic and magnetic structure.

In general one aims for the smallest possible (and pracitcal) magnetic unit i.e. information unit. With respect to the usage of molecules there are two main concepts which may be pursued. The first approach is to deposit magnetic molecules on a non-magnetic substrate. In this manner, the molecules have to be designed to show a magnetic moment themselves and zero-field splitting, so as to act as the magnetic unit. These so-called single molecule magnets (SMMs) tend to be rather big complexes housing a metallic ligand and are a promising route to molecular spintronics [5, 58]. In general these molecules are hard to handle though in regards to their stability upon sublimation and the low blocking temperature [5, 59]. Nevertheless, spin valves have already been fabricated using $\mathrm{TbPc_2}$ single molecular magnets together with carbon nano tubes (CNT) sandwiched between non-magnetic electrodes [60].

The other approach is to deposit certain non-magnetic organic molecules on a magnetic substrate as single crystalline or epitaxial iron or cobalt. In this manner the π-orbitals of the former non-magnetic molecules may hybridize with the electronic band structure of the underlying substrate. It has been reported that in this way, molecules can form a new magnetic unit on the surface with a magnetic moment different from that of the magnetic substrate, so-called hybrid molecular magnets. This approach aims to overcome the obstacles of the SMM approach and has gained interest in research both theoretically and experimentally [8, 12].

In order to understand this phenomenon, it is necessary to have a look at the adsorption behavior of molecules on (magnetic) metals. As mentioned in Sect. 3.2 the orbitals of molecules in gas phase show a discrete energy distribution. Metals in contrast have a band-like continuous density of states. When depositing molecules on a metal, both "types" of DOS interact and affect each other so that new DOS's with own characteristics develop. Generally speaking there are two different types of adsorption. Weakly bonding *physisorption*, where mainly Van-der-Waals forces contribute to the tie of the molecules to the surface [61]. Here the interaction of the molecules with the surface is weak and the molecular orbitals, although slightly broadened, remain basically discrete and thus molecular-like. Typical adsorption energies are in the range of 200-400 meV per molecule. If the molecules are strongly i.e. chemically bound to the surface, one speaks of *chemisorption*. In this case the orbitals interact strongly and the molecular orbitals are heavily modified i.e. shifted, broadened and overall more solid-state like[1]. Typical adsorption energies are in the range of 0.5-4 eV per molecule.

To obtain hybrid molecular magnets, it is obvious that chemisorbed molecules are preferably to obtain hybrid adsorbate surface states which differ strongly from the original molecular states and to utilize their certain properties. Therefore, molecules chemisorbed onto magnetic surfaces are of particular interest. The following outlines the underlying principles of hybridization between molecule and metal states. Subsequently an experimental application will be described.

3.3.1 Hybrid Adsorbate-Surface States

As mentioned above, chemisorption of molecules on a metal surface basically leads to the occurrence of two effects. In the following, the main mechanisms are presented

---

[1] Of course the orbitals of the corresponding metal atoms are modified as well in this picture.

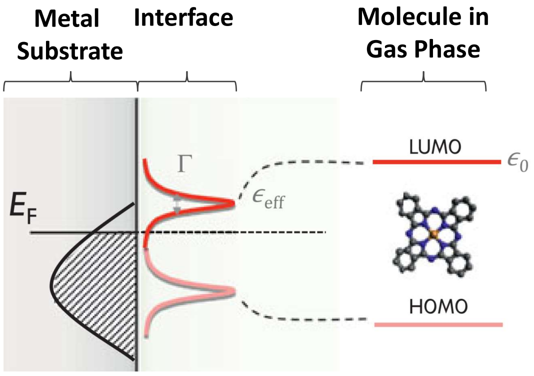

Figure 3.3: The DOS of the metal substrate has a band-like structure and is occupied below E_{F}. The discrete orbitals (HOMO, LUMO) of a molecule in gas phase broaden (Γ) and shift (ϵ_{eff}) when adsorbed on the metal surface by chemisorption. Taken from [13].

essentially on the basis of the publication by Galbiati et al. [13].

Firstly the broadening (Γ) of the former discrete molecular orbital energies, which arises from the previously infinite lifetime (τ) becoming finite, hence the broadening can be correlated with the lifetime $\Gamma \approx \frac{\hbar}{\tau}$. Secondly the molecular energies shifts ($\Delta\epsilon = |\epsilon_0 - \epsilon_{\mathrm{eff}}|$) due to the influence of the substrate DOS [13, 62]. Thus, Γ and ϵ_{eff} are two important values when characterizing hybrid adsorbate-surface states. When the bond and the interaction between the molecule and the substrate is strong (chemisorption) the high values of Γ and $\Delta\epsilon$ may occur and the DOS of the interface region may differ strongly from both, the band-like metal DOS and the discrete molecular states [63, 64].

Figure 3.3 shows the principle of said two fundamental effects on the DOS of the substrate and the molecule upon adsorption of a molecule on a metal substrate. The continuous DOS of the metal substrate on the left is occupied below the Fermi energy (E_{F}). The isolated organic molecule on the right has discrete levels. In the sketch HOMO and LUMO are shown exemplarily. The interface region in the middle represents what happens when the molecule is brought in proximity with the metallic surface. The interaction with the metal leads to a broadening (Γ) of the states and the new formed state in the interface region has a shifted energy of ϵ_{eff} [13].

Figure 3.4 shows a more in depth look into the described phenomenon. Obviously the adsorption energy and the strength of the bond depends heavily on the substrate material. Harutyunyan et al. investigated the effects upon adsorption of cyclooctatetraene (COT) on different metal substrates both theoretically and experimentally [65]. Figure 3.4(a) shows STM measurements of COT on Au(111), Ag(100) and Cu(100). The column besides shows the corresponding proposed models of the adsorbed molecule on the respective surface. The STM images reveal a completely different appearance of the molecules with different rotational symmetries on each substrate. The models next to them reveal the different adsorption geometry of COT on the each substrates. The observation is explained by the fact that COT is only weakly bound and physisorbed on the noble gold. Based on DFT calculations, the molecule itself proved to be stable and energetically advantageous in a so-called tub configuration. The distance from the molecule to the substrate surface was determined to be 2.86 Å. The bond strength increases on the other two substrates (Ag(100) and Cu(100)). On both silver and copper, the authors observed chemisorption with stronger bonds and a lower distance of 2.39 Å and 2.10 Å, respectively. In both cases, the molecule adopts a planar geometry in which it lies flat and parallel to the substrate surface. The adsorption energies are -0.162 eV (Au(111)), -1.604 eV (Ag(100)) and -2.636 eV (Cu(100)).

These observations are also reflected in the calculated DOS in Fig. 3.4 (b). The top two plots of each column show the calculated DOS for COT in gas phase, with the left plot representing the DOS in tub configuration, while the right plot corresponds to the DOS of the flat molecule. In both configurations, the molecular orbitals are well identified by the sharp and intense peaks. Below and above the Fermi energy $\mathrm{E_F}$, HOMO and LUMO are labeled in both plots. In the left column below, the calculated DOSs for COT are shown when adsorbed on Au(111), Ag(100) or Cu(100), respectively. In the case of Au(111) in said tub configuration and for Ag(100) and Cu(100) each adsorbed flatly. It can be seen that the DOS of COT/Au(111) still shows essentially the same peaks, which are slightly shifted and broadened, but still with molecular character. Consequently, the DOS confirms the assumed physisorption. For Ag(100) and Cu(100), however, the sharp peaks are largely suppressed and, if identifiable at all, significantly shifted. Both DOS indicate chemisorption of COT on silver and even stronger on copper. The right column shows plots of the corresponding DOSs of the surface atoms of the substrate. The green graph represents the clean surface, while the blue graph indicates how the DOS of the substrate surface atoms are altered by the adsorbed COT on top. One can clearly tell, that the modification is largest in the case of Cu(100) further confirming a strong interaction between adsorbate and substrate.

Additional to these effects, other phenomena may play a role during the adsorption

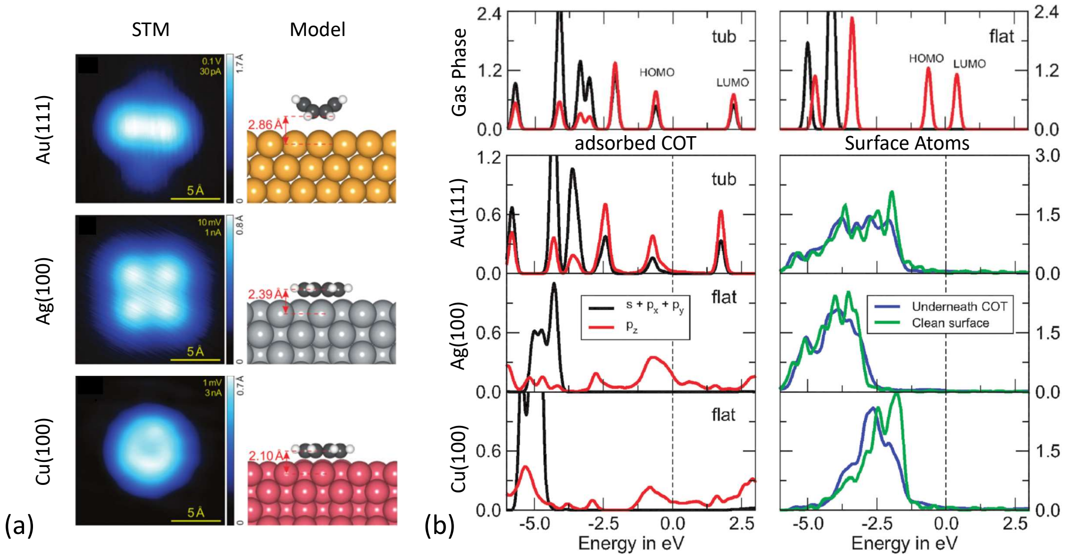

Figure 3.4: (a) STM measurements of COT on Au(111), Ag(100) and Cu(100) besides the respective proposed models. On gold, COT is physisorbed, furthest from the surface atoms and in a tub configuration. With increasing adsorption energy, the molecule lies flat and close to the surface atoms and is chemisorbed. (b) The calculated DOS of COT in gas phase in tub and flat configuration show sharp and discrete molecular orbitals. HOMO and LUMO are marked and perfectly distinguishable. The calculated DOS of COT adsorbed on the surfaces reveal a broadening an shift of the former molecular like orbitals. The graph of the substrate surface atoms shows that the DOS of the metals is altered as well. Taken from [65].

process, e.g. electron transfer from the substrate to the molecule or strain within the molecule due to altered molecular geometry due to adsorption. A previously highly degenerated rotational symmetry can, for example, be forced into a certain position upon adsorption, which may lead to new intra-molecular bonds and/or intra-molecular strain. This strain may also destroy the molecule and the bonds may further influence the electronic structure. Although there are other mechanism how a molecular orbital might become spin-split upon adsorption[2], electron transfer might be of particular importance if the substrate is magnetic and thus the hybrid states may also be spin-split with a different polarization than the substrate ($P_{\text{Hybrid}} \neq P_{\text{Substrate}}$).

Figure 3.5 shows a schematic representation the same scenario as Fig. 3.3 with the exception, that the substrate is a ferromagnetic (FM) metal and the hybridization of the DOS of the adsorbed molecule with the DOS of the FM substrate is spin-

---

[2] Previously spin-degenerate molecular orbitals may split and one may contain more or less electrons $\pm\Delta e$ than the other, while the net charge of the molecule remains the same.

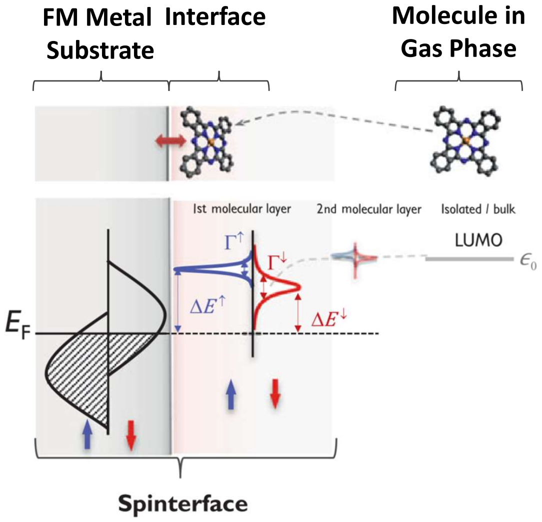

Figure 3.5: Chemisorption as in Fig. 3.3 but with a ferromagnetic metal substrate. The LUMO of the molecule at the interface is broadened and shifted with different values (Γ, ϵ_{eff}) for each electron species. The spin dependent hybridization is still present in the second molecular layer but significantly weakened. Taken from [13].

dependent as well. In the example shown, the LUMO of the exemplary organic molecule splits up with different energy shift and broadening Γ for each spin orientation ($\Delta E^\uparrow = E_\text{F} - \epsilon^\uparrow_\text{eff}$, $\Delta E^\downarrow = E_\text{F} - \epsilon^\downarrow_\text{eff}$, $\Delta\Gamma^\uparrow$, $\Delta\Gamma^\downarrow$). Hence, the first molecular layer is spin polarized with a different polarization as the FM substrate. Obviously the strength of this effect correlates to the strenght of the interaction and thus the coupling strength. Consequently, the effect is attenuated if present at all in the subsequent molecular layers on top of the first molecular layer. The molecular unit on the surface then forms a hybrid-molecular magnet on the surface. This opens the pathway for potential applications in devices with electrodes incorporating the FM substrate and the first molecular layer which both will be subsumed under the term *spinterface* [13]. The idea is that one could use this metal/molecule spinterface to tailor the properties of spintronic devices by combining ferromagnetic metals to organic and potentially easy to handle molecules [66]. The molecules may be tailored to have a DOS which is fitting to the needs of the envisioned application, delivering a toolbox for future applications.

In order to know these needs and thus tailor and combine the materials adequately, it is necessary to understand the described effects and to build a proper model. The effective spin polarization in said hybrid-molecular magnets is:

$$P_{\mathrm{Hybrid}} = \frac{D^{\uparrow}_{\mathrm{Int}} - D^{\downarrow}_{\mathrm{Int}}}{D^{\uparrow}_{\mathrm{Int}} + D^{\downarrow}_{\mathrm{Int}}}, \tag{3.1}$$

with the spin-polarized DOS being expressed by means of a Lorentzian distribution

$$D^{\uparrow(\downarrow)}_{\mathrm{Int}}(E) = \frac{\Gamma^{\uparrow(\downarrow)}/2\pi}{(E - \epsilon^{\uparrow(\downarrow)}_{\mathrm{eff}})^2 + (\Gamma^{\uparrow(\downarrow)}/2)^2}. \tag{3.2}$$

This is the effective DOS of the spinterface for both spin orientations and thus the DOS of the effective electrode [13].

In general two scenarios can be distinguished when tailoring the spin-dependent hybridization properties. These scenarios result from weak or strong coupling strengths correlating with a broad or narrow broadening. In the first scenario, the broadening is larger then the level distance to Fermi energy, i.e. $\Gamma \gg \Delta E$. Then Eq. 3.2 yields

$$D^{\uparrow(\downarrow)}_{\mathrm{Int}} \approx \frac{1}{\Gamma^{\uparrow(\downarrow)}} \propto \frac{1}{D^{\uparrow(\downarrow)}_{\mathrm{FM}}} \tag{3.3}$$

which means, that the effective spinterface DOS is inversely proportional to the original DOS of the electrode [13]. Thus with Eq. 3.1 it is

$$P_{\mathrm{int}} = \frac{\Gamma^{\uparrow} - \Gamma^{\downarrow}}{\Gamma^{\uparrow} + \Gamma^{\downarrow}} \approx -\frac{D^{\uparrow}_{\mathrm{FM}} - D^{\downarrow}_{\mathrm{FM}}}{D^{\uparrow}_{\mathrm{FM}} + D^{\downarrow}_{\mathrm{FM}}} = -P_{\mathrm{FM}}. \tag{3.4}$$

Hence, rather strong couplings mainly lead to a hybrid-molecular magnet that exhibits an inverted spin polarization with respect to the FM substrate. The second scenario $\Gamma \ll \Delta E$ meaning that the molecular levels are only slightly shifted and the broadening is neglectable which is in particular the case if the molecules are weakly interacting with the surface. Then, Eq. 3.2 yields

$$D_{\mathrm{Int}}^{\uparrow(\downarrow)} = \frac{\Gamma^{\uparrow(\downarrow)}}{(\Delta E^{\uparrow(\downarrow)})^2} \propto \frac{D_{\mathrm{FM}}^{\uparrow(\downarrow)}}{(\Delta E^{\uparrow(\downarrow)})^2} \tag{3.5}$$

meaning, that the spinterface DOS is proportional to the original FM DOS but is lifted due to the small denominator. This results in an enhancement of the spin polarization [13] and with Eq 3.1 the spin polarization of the interface may be expressed as:

$$P_{\mathrm{int}} = \frac{\frac{\Gamma^{\uparrow}}{\Delta^{\uparrow 2}} - \frac{\Gamma^{\downarrow}}{\Delta^{\downarrow 2}}}{\frac{\Gamma^{\uparrow}}{\Delta^{\uparrow 2}} + \frac{\Gamma^{\downarrow}}{\Delta^{\downarrow 2}}} > P_{\mathrm{FM}}. \tag{3.6}$$

Such spin-dependent hybridization with FM-Molecule-Hybrid electrodes (i.e. spinterfaces) has already been observed in experiment and in particular in magnetoresistance measurements (MR) [8, 12, 66, 67, 68]. We will take a closer look at one of these devices in the next section as it is of particular interest for this thesis.

3.3.2 Interface Magnetoresistance in Devices

In the last decade first successes in building molecular spintronic devices have been reported. In 2013 Raman et al. designed devices incorporating hybrid molecular magnets, which show a magnetoresistance (MR) of up to 25% which is based on interface effects alone (42% with a Permalloy top electrode), as the devices comprise a single ferromagnetic electrode [12]. The effect will be therefore referred to as interface magnetoresistance (IMR). In the following, the phenomenon of IMR will be presented on the basis of the publication by Raman et al. [12].

Figure 3.6 shows a magnetoresistance measurement of a device with only one ferromagnetic electrode. Raman et al. deposited a 40 nm thick film of non magnetic zinc-methyl-phenalenyl (ZMP) between a ferromagnetic cobalt electrode and a non magnetic copper electrode (Co (8 nm)/ZMP (40 nm)/Cu (12 nm)). The isolated ZMP has no net spin but adsorbed on the metal surface, charge transfer processes through hybridization change the chemical state, so that the molecule becomes a anionic radical with net moment [12]. The planar geometry of the phenalenyl moiety endorses strong overlap of the orbitals and thus a hybridization of the d orbitals of the substrate (mainly d_{z^2}, d_{xz} and d_{yz}) with the p_{z} molecular orbitals, forming a hybrid molecular magnet at the interface. This effect obviously occurs only in the interface region between the first layer of chemisorbed molecules, which interact strongly with the Co so that the DOSs hybridize, while the ZMP layers on top of the first layer are physisorbed only. Therefore the ZMP layer in the stacking sequences in the left and right of Fig. 3.6 consists of an interface and a bulk region. The transport within the device has been measured at 15 mV after the device was cooled down to 4.2 K within a magnetic field of -50 Oe. The field has been swept positively (blue data points) and negatively (red data points). The device shows a large magnetoresistance of 25%. The hysteresis loop corresponds perfectly to the reversal of the Co magnetization (red arrows in the sketches) as the device switches at the coercivity of Co $H_{\mathrm{c}}(\mathrm{Co})=\pm 38$ Oe. This is explained by the switching of the Co electrode at $H_{\mathrm{c}}(\mathrm{Co})$ with respect to the hard magnetic interface layer whose switching field differs from that of cobalt.

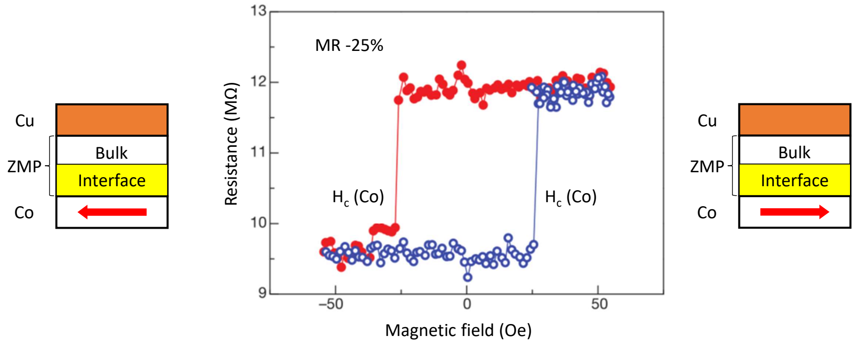

Figure 3.6: Magnetoresistance measurement of a device with the stacking sequence Co/ZMP/Cu at 4.2 K. The magnetoresistance loop corresponds to the switching of the cobalt electrode at the coercivity field of H_{Co}. As there is only a single ferromagnetic electrode involved, the resistance has to arise from an interface effect and in particular from a hard magentic layer forming at the interface (yellow region in the stacking sequence). Taken from [12].

This hard magnetic interface layer switches at a considerably higher magnetic field. Figure 3.7 (a) shows the magnetoresistance curve of another device exploiting IMR. The top electrode here consists of soft ferromagnetic Permalloy (Py), i.e. Co/ZMP (35 nm)/Py. At 4.2 K the bottom Co/ZMP interface layer switches at about ±600 Oe to the low resistance state. The principle of the switching sequence is shown in Fig. 3.7 (b). In the low resistance state at high negative fields, the magnetization direction of the bulk cobalt of the electrode and the hybrid molecular magnet are aligned parallel so that the interface layer favors the same spin species as the electrode delivers. At the coercivity of Co, the electrode switches its magnetization direction while the interface layer remains hard so that the magentization is now anti-parallel to each other. Thus the resistance increases. As the magnetic field increases further, eventually the interface layer switches as well and the resistance drops back to the low resistance value. The same interface switches near room temperature (250 K) at 100 Oe with still a large IMR of 22%.

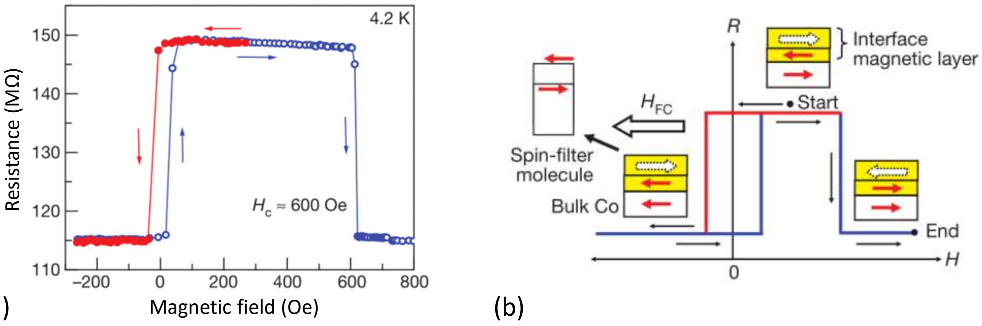

(a) (b)

Figure 3.7: (a) Measurement of IMR in a Co/ZMP/Py device with high external magnetic field 4.2 K. The switching loop around zero is still due to the switching of Co. The switching at $H_{\mathrm{C}} \approx 600$ Oe arises from the switching of the hard magnetic interface layer, hence the device is again in a low resistance state at high applied magnetic field. (b) Model for the switching where the interface magnetic layer comprises the surface hybridized Co atoms and the hybridized first and second organic layer (red and white arrows, resp.). In the low resistance state at negative H values, the magnetization direction of the bulk cobalt is aligned with the magnetization of the first interface magnetic layer. When the bulk Co switches at its coercivity, the device switches to a high resistance state as the interface magnetic layer is magnetically harder than bulk Co. Eventually the interface magnetic layer switches as well and the device is in low resistance state again. Taken from [12].

According to Raman et al. the IMR behavior described above is based on the following model. The adsorbed dimer forms a pair of a magnetic molecule directly adsorbed on the Co and a spin-filter molecule physisorbed on top of the magnetic molecule. The Co electrode delivers spin polarized s-p electrons and thus acts as a spin-polarizer, while the magnetic interface layer has a spin-dependent interface resistance and therefore acts as a spin analyzer preferring a certain species of spin to let through [12]. Therefore IMR is not only explained by the first molecular layer but also by the spin-selective tunneling through the spin-filter molecule with respect to the spin species supplied by the ferromagnetic electrode. Figure 3.8 (a) shows said dimer consisting of a first and a second ZMP molecule. The first ZMP is chemisorbed on the first cobalt layer and becomes a hybrid molecular unit while acquiring a net moment of 0.11 μ_{B} which is anti-parallel to the moment of the hybridized first cobalt layer which results in an anti-ferromagnetic coupling ($J_{\text{Co-ZMP}} < 0$) with the moment of the surface Co atoms is lowered by $0.2\,\mu_{\text{B}}$ per atom [12].

The second ZMP is physisorbed and has no magnetic moment but the π orbitals of the second molecule interact with the π orbitals of the magnetic molecule. Figure 3.8 (b) shows the calculated DOS for both the magnetic molecule (green plot) and the second ZMP (purple plot). It is clearly evident that the DOS of the magnetic molecule shows significantly broadened states and an overall more band-like structure, whereas the DOS of the second ZMP essentially exhibits the characteristic sharp peaks of molecule orbitals. The region of interest around E_{F} is shown in detail in Fig. 3.8 (c). The upper half above the Fermi energy is the (unoccupied) DOS of the second ZMP, while the lower half below the Fermi energy is the (occupied) DOS of the magnetic molecule. Due to said π-π interaction, the lowest unoccupied molecular orbital (LUMO) of the second ZMP is spin-split with a gap of 0.14 eV. Therefore the second ZMP favors the tunneling of one spin species over the other by forming two different barrier heights (spin-down electrons $\phi_{\downarrow}$: 0.73 eV, spin-up electrons $\phi_{\uparrow}$: 0.87 eV). Therefore the second ZMP is considered to act as a spin filter molecule, whose preferred spin transmission direction is always aligned anti-parallel with the magnetization of the interface layer which is also depicted in the scheme in Fig. 3.7 (b). Both effects, the magnetic interface layer due to hybridization and the spin filtering of the second ZMP is responsible for the large magnetoresistance even close to room temperature [12].

Based on these surprising and promising studies, it is worthwhile to investigate further systems of ferromagnetic substrates and organic molecules and, in the long run, even to implement further or new effects in devices. For this purpose, it is particularly interesting to start from the microscopic point of view of the single molecule and to gain an understanding of the smallest unit of a device, namely the single molecule, in order to then proceed to the mesoscopic scale in the form of a bottom-up approach. To open this way further is the motivation for the scope of this work which will be described in the next chapters.

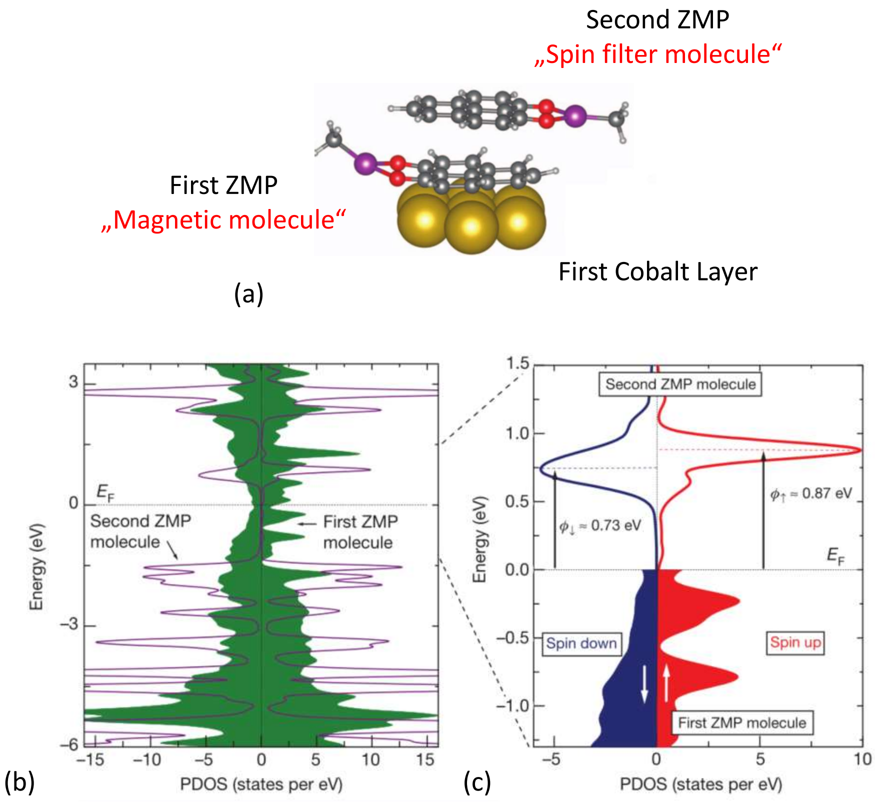

Figure 3.8: (a) Model of the interface magnetic layer as proposed by Raman et al. with the first Co layer hybridizing strongly with the first layer of ZMP and weakly with the second layer of ZMP. (b) Calculated PDOS of the p-states of the first (green) and second (purple) ZMP molecule. The electronic structure is spin-unbalanced around E_{F} due to hybridization with the magnetic substrate. The region of interest ([-1.5,1.5 eV]) is shown magnified in (c). The LUMO of the second ZMP molecule is spin-split by 0.14 eV which constitutes a different barrier height for each electron species tunneling through the second layer ZMP. Taken from [12].

Chapter 4

Experimental Setup and Substrate Preparation

This chapter describes the main experimental setup and the additional methods used in the course of this thesis. Since an important prerequisite for almost all investigations was to grow clean epitaxial Co(0001) films on Au(111), this procedure is seen as a basic experimental requirement and is also presented in this chapter. Since this work is to a large extent a technical work, in which especially the sample preparation and later the device fabrication plays an important role, a description of the necessary instrumental extensions for the device preparation and the epitaxial growth on insulators, as well as the preparation of closed BNTCDI films with exclusively intact molecules is omitted at this point. These topics will be presented within the scope of the results in Chapters 5 an 6, respectively. Therefore, this chapter contains a description of what can be seen as the experimental prerequisite which is necessary for the later chapters.

4.1 Nano Spintronics Cluster Tool - NSCT

The main system for the preparation of the samples and their microscopic examination within the scope of this work was the Nano Spintronic Cluster Tool of PGI-6 at Forschungszentrum Jülich. This system was modified in order to manufacture test devices completely *in-situ*. These modifications are part of the results of the measures taken to produce devices and are therefore described in Chapter 6, as they were not part of the NSCT in the first place. The basic system will be presented in this section. Figure 4.1 shows a schematic overview over the NSCT with marked functional segments.

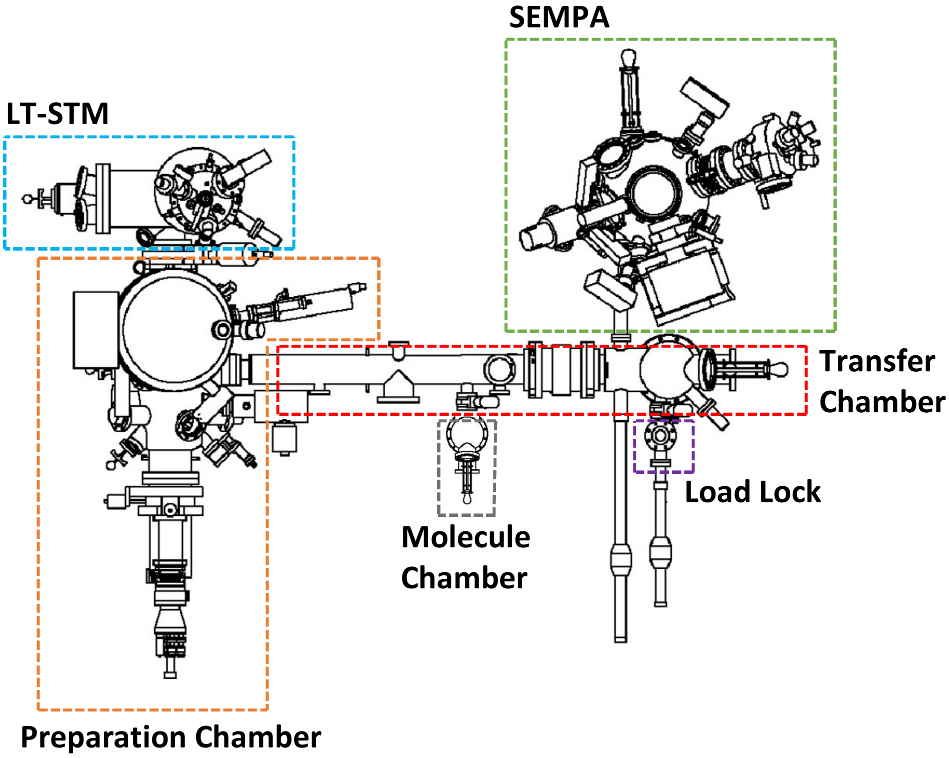

Figure 4.1: Schematic overview of the NSCT with marked functional blocks. Taken from [69] and modified.

The basic idea of NSCT is to prepare microscopy samples and to examine them by different methods without breaking the vacuum and thus to get the clearest possible insight into the physics of the samples and, if necessary, from different perspectives. To this end, NSCT houses an abundance of preparation and analysis tools in hermetic chambers which can be connected within UHV conditions. Basically, one distinguishes between the so-called bottom-up and the top-down approach in sample preparation and examination. The NSCT is designed to be able to follow both approaches. The aim of this work was to transfer from a bottom-up approach (atomic and molecular properties) to larger size scales and corresponding properties (transport, resistance), thus bridging the gap between microscopic and mesoscopic properties.

A common route to prepare samples in solid state physics is to grow epitaxial films on a suitable substrate. Suitable substrates are usually well-defined and ordered single-crystals (e.g. W(110) or Au(111)) on which materials (e.g. Cu, Au, Nb, Cr, Co) can be grown by MBE for subsequent examination. However, other substrates can also be of fundamental importance, for epitaxial growth of metals on insulating substrates see Sect. 6.2. The preparation of the samples mainly happens in the preparation chamber (orange box). Single crystal Au substrates must always be cleaned and annealed to ensure a clean and well-ordered surface. This is done by Ar^+-bombardment (sputtering) and subsequent temperature treatment. For this purpose, a sputter gun and an e-beam heater are located in the preparation chamber. The preparation chamber houses three different evaporators. A electron-beam evaporator from Thermionics provides five different crucibles with different materials and the deposition with rather high rates. In the course of this work, this evaporator has been used to evaporate Au, Cu, Co, Nb and MgO. The second evaporator is a triple rod evaporator from FOCUS which allows the evaporation with extremely low operation pressures. It has been used for a large part of the growth studies of cobalt on gold and for a few attempts of Fe samples. For the deposition of organic materials (i.e. BNTCDI and DE61[1]) an evaporator with glass crucible with an opening cross-section of $4.5\,\mathrm{mm}^2$ has been used. The sublimation took place by resistive heating. An identical evaporator is also present in the molecule chamber (grey box). Furthermore, the preparation chamber is equipped with a low energy electron diffraction (LEED), an X-ray photoelectron spectroscopy (XPS) and an Auger electron spectroscopy (AES) system, as well as means for cooling or heating a sample during preparation ($30\,\mathrm{K} \leq T_{\mathrm{Sample}} \leq 500\,K$).

The majority of the microscopic and spectroscopic investigations were performed by means of the LT-STM from Omicron (blue box) which can be operated with liquid nitrogen (LN_2, $T \approx 77\,\mathrm{K}$) or liquid helium (LHe, $T \approx 4.4\,\mathrm{K}$). The STM has been used to study the growth of different nano-scaled systems and the adsorption of both single molecules and organic monolayers in order to understand the initial state of the formation of the targeted organic barriers in mesoscopic devices (bottom-up approach). STM is used for microscopic studies and STS for spectroscopy (cf. Chapter 2).

NSCT has another analysis chamber (green box) with a scanning electron microscope (UHV Gemini column from ZEISS) with polarization analysis (SEMPA) and a focused ion beam facility (FIB). In this work, the (non-polarized) electron beam microscope (SEM) was used to check the geometry of structures deposited with shadow masks, however, this turned out to be quite challenging due to severe charging ef-

---

[1] Internal name of another precursor molecule which has been deposited on Au(111) at an early stage of this work.

fects on the highly insulating Al_2O_3 and mica substrates as described in Chap. 6. All samples were loaded and unloaded via the load lock (purple box) and transferred between the chambers via a train inside the transfer chamber (red box).

4.2 Other Techniques

In addition to the possibilities of the NSCT and the implemented modifications, additional methods were used in other facilities. An atomic force microscope (AFM) from Asylum Research (now Oxford Instruments) operated at ambient pressure was used to check film and substrate quality on larger scales. (Magneto-)transport measurements were performed *ex-situ* in a 4-probe configuration in a physical properties measurement system (PPMS) from Quantum Design at PGI-4/JCNS that provides temperatures from 1.9 to 400 K and an out-of-plane magnetic field which can be swept during the measurement ($-5000\,\mathrm{Oe} \leq \vec{H} \leq +5000\,\mathrm{Oe}$).

Further transport measurements, in particular during the troubleshooting, have been performed at the cryo transport lab of PGI-6, a 4-probe station at PGI-7 and within a 4-tip STM machine at PGI-6. The SEM of the 4-tip STM system has also been used to further investigate said deposited geometries. Some growth studies demanded a deposition rate which was beyond the capability of the crucible evaporator of the NSCT. For this purpose, some samples were prepared in a facility of PGI-7 by magnetron sputtering. Some samples were transferred back and forth between the systems by means of a vacuum suitcase to prevent contamination.

4.3 Preparation of Epitaxial Co(0001)/Au(111) Substrates

In the scope of this work a major focus lay on the deposition and investigation of BNTCDI molecules on Co(0001). As the envisioned spintronic device would consist of multi-layered electrodes, the usage of a cobalt single crystal for deposition studies was not an option. Instead, the examination should be carried out on epitaxially grown Co layers, so that the results would also be applicable to the targeted cobalt electrodes grown on an insulator to prevent short circuiting. Since a gold film with (111) surface will serve as buffer layer for the bottom electrode of the envisioned devices, Co(0001) has to be grown epitaxially top of the gold. Since the adsorption of BNTCDI on these epitaxially grown Co(0001) layers is relevant for the later device interface, all investigations thereof were carried out on Co(0001)/Au(111). As the preparation of sufficient thick gold layers is very time-consuming within our technical setup, an Au(111) single crystal was used here for time reasons and a thin layer of Co(0001) was deposited on it.

Since cobalt is highly reactive and therefore contaminates very quickly even under UHV conditions, a new cobalt layer for almost every molecule investigation cycle had to be prepared. For this purpose gold was chosen as substrate, so that cobalt was grown on an Au(111) single crystal by MBE. Although it has been shown that electrodeposited cobalt film show the exact same magnetization as films grown by MBE [70], all materials in the presented multi-layer systems were deposited under ultra-high vacuum (UHV) conditions to prevent a covering of the cobalt surface by adatoms. Epitaxial growth of Co(0001) and Co(111) on Au(111) and the magnetism of thin Co films on Au(111) have extensively been investigated [71, 72, 73, 74, 75, 76, 77]. On a Au(111) surface, cobalt grows epitaxially in <111>-direction (fcc) [72] or [78]. It is also well-known that thin cobalt films exhibit a transition from the predominant fcc phase in the ultrathin-film limit below 4 monolayer (ML) [79] to the hcp bulk phase at a thickness of a 0.8-2.0 nm [71, 79]. Thin Co films on Au(111) also show a spin-reorientation transition between out-of-plane to in-plane magnetization at a thickness of about 4.5 ML [72, 75].

Furthermore due to the immiscibility of Co and Au and despite the large lattice mismatch of 14.5% it has been reported that Au und Co tend to form superlattices with abrupt interfaces with Co growing in $< 0001 >$-direction (hcp) in its initial state [80]. Thus, I assume that without any annealing (during deposition or post annealing), the deposited Co layer is essentially discrete with an abrupt interface between Co and Au. Consequently, the thicknesses given in the course of this work are considered to be those of more or less pure cobalt or pure gold, resp. All measurements and considerations regarding the growth of the Co/Au system are based on MBE under UHV conditions. For the sake of completeness, it should be noted that Co can also be deposited electrochemically on Au as shown by Kleinert et al. [81] and is well studied on both Au and Ag [76].

As many other materials the Au(111) surface is well known for the formation of a characteristic surface reconstruction, i.e herringbone reconstruction [82]. Surface reconstructions are common in particular in the case of semiconductors, e.g. Si(111)

7x7 [83]. This phenomenon occurs far less frequently with elemental metals. An exception are the face-centered cubic noble metals of the 6th period, Ir, Pt and Au, where the (100) and (110) surfaces reconstruct. In the case of gold, the (111) surface reconstructs too. In general, surface reconstructions are caused by the particularly low surface energy of hexagonally dense surfaces of these metals and a high tensile stress. Due to its characteristic zigzag shape with sharply pronounced corners ("elbows"), the coordination number for adatoms changes at these corners which has consequently an influence on the initial nucleation of the deposited Co atoms in the sub ML regime. It has been reported by Voigtländer et al. [73] that during initial nucleation and the subsequent growth on Au(111), cobalt nucleates forming polygonal islands. The location and spacing of these islands are determined by the geometry of the underlying herringbone reconstruction. The island height is two atomic layers while growing laterally with increasing coverage until a closed film forms [73].

This is in good agreement with the results of this work. Figure 4.2(a) shows an $100{\times}100\,\mathrm{nm}^2$ STM map of a Au(111) surface of a gold single crystal. After the gold single crystal was transferred into the NSCT-system, it was degassed for 30 min at 700°C to remove the dissolved gasses from the surface and the bulk of the crystal. Afterwards the surface has been sputtered for another 30 min by Ar-ion bombardment with 800 eV ion energy to remove adsorbates and dirt. Subsequently the cleaned crystal has been annealed for 40 min at 700°C to flatten the surface and rearrange the surface atoms. Then, the sample was transferred into the pre-cooled STM in the STM chamber and cooled down to the STM base temperature. The STM had a base temperature of 79 K (LN_2) whilst the STM chamber had a base pressure of $4 \cdot 10^{-11}$ mbar. The resulting surface shows a very well pronounced and ordered herringbone reconstruction, indicating a well ordered and clean Au(111) surface. The visible $(\sqrt{3} \times 22)$ reconstruction consists of periodically occuring regions of hcp and fcc stacking sequencies (see markings in Fig. 4.2(a)).

The herringbone reconstruction is a good indicator for a clean gold surface. On a clean Au(111) surface the first atomic layer is crowded which induces lateral strain and the reconstruction occurs to relieve this strain. To be precise, the unit cell of the herringbone reconstructed surface consists of 23 atoms as a top layer on 22 atoms on the underlying bulk lattice sites. That induces a contraction of 4.5% along the $[1\,\bar{1}\,0]$ direction with stacking faults resulting in wide fcc and narrow hcp regions [85]. The $\sqrt{3}$ direction perpendicular to the compressed $[1\,\bar{1}\,0]$ direction (cf. Fig. 4.2(a)) remains without any compression and the other two $\sqrt{3}$ directions show a partial compression of 3.9% [43]. The pairwise zigzag corrugation lines which appear bright in Fig. 4.2(a) are soliton walls separating the hcp from the fcc areas. The zig zag structure shows an angle of 120° which is energetically favorable to relieve the strain isotropically [85].

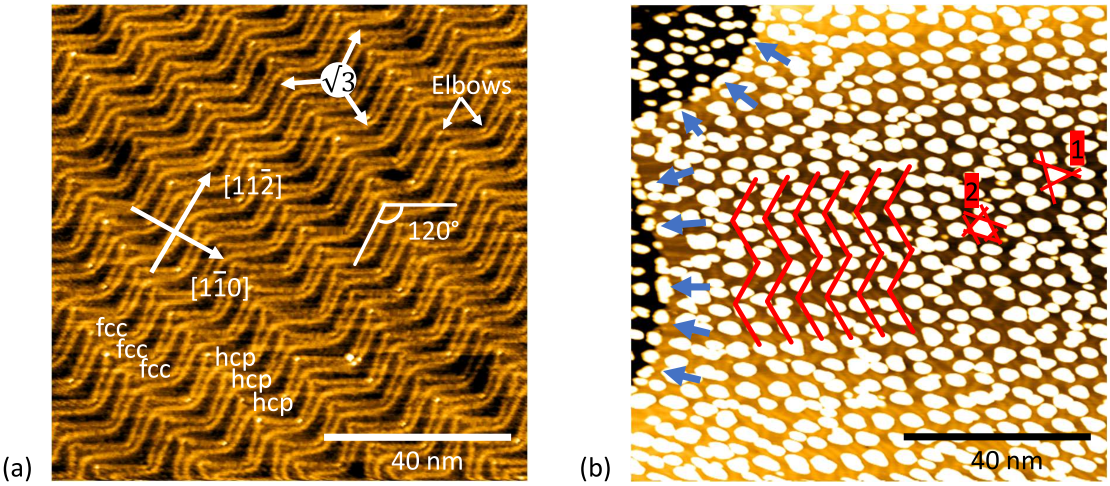

Figure 4.2: (a) STM of a clean and well ordered Au(111) surface of a gold single crystal after the standard preparation cycle. The characteristic herringbone reconstruction separates alternating fcc and hcp regions ($100\times100\,\mathrm{nm}^2$, $V_{\mathrm{bias}} = 50\,\mathrm{mV}$, $I_{\mathrm{t}} = 1.0\,\mathrm{nA}$, $T = 79\,\mathrm{K}$). (b) STM of the same sample after the deposition of Co islands ($100\times100\,\mathrm{nm}^2$, $V_{\mathrm{bias}} = -1.0\,\mathrm{V}$, $I_{\mathrm{t}} = 1.0\,\mathrm{nA}$, $T = 79\,\mathrm{K}$).

Figure 4.2(b) shows a $100\times100\,\mathrm{nm}^2$ STM map of the very same sample as Fig. 4.2(a) after the deposition of ≤ 1 ML Co by MBE from a rod evaporator. After the sample has been warmed up to room temperature in the preparation chamber the following deposition was executed. The evaporation parameters of the rod evaporator were $U = 800\,\mathrm{V}$, $I_{\mathrm{Fil}} = 1.98\,\mathrm{A}$, $I_{\mathrm{Emission}} = 11.5\,\mathrm{mA}$, Flux $= 46.5\,\mathrm{nA}$ with an estimated deposition rate of $\leq 0.2\,\mathrm{ML/min}$. The deposition was controlled by a shutter to last exactly 5 minutes. The pressure in the preparation chamber did not exceed $2\cdot10^{-9}\,\mathrm{mbar}$. After the deposition, the sample has been transferred directly into the STM without any post annealing or other treatment. The conditions in the STM chamber remained unaltered and the sample has been cooled down to liquid nitrogen temperature.

The contrast in Fig. 4.2(b) was intentionally adjusted that hard to emphasize the gold substrate under the cobalt islands. The very bright spots are the cobalt islands. One can clearly see the still apparent herringbone reconstruction. Although it looks somewhat modulated, it is easy to see how the cobalt islands and thus the nucleation centers essentially follow the geometry of the soliton walls of the herringbone reconstruction. The red zig zag lines in Fig. 4.2(b) have an angle of 120° and indicate the underlying geometry structurally. Obviously, the nucleation has a quite regular and ordered distribution. Two mechanism seem to affect and favor the cobalt nucleation position. Firstly, the herringbone reconstruction and secondly the characteristic vicinal character of the gold surface. The blue arrows in Fig. 4.2(b) indicate a step edge that the nucleation centers seem to follow without respect to the reconstruction. Both is in good agreement with the findings of Repain et al. [86]. The same holds for the islands size. The nucleation centers start to form triangular island (red bars 1). The initial nucleation is not distributed evenly which is caused by surface impurities and the particle flux to diffusion ratio [87]. This results in a relatively broad distribution of the lateral sizes of the islands during the first deposition phase and is therefore time dependent. Yet, during growth the islands begin to become polygonal (red bars 2) which evens out the multimodal nucleation resulting in a narrower lateral size distribution, which is in good agreement with Morgenstern et al. [76]. The lateral position of the cobalt islands in Fig. 4.2(b) correspond to the elbows of the herringbone reconstruction. The lateral spacing between the centers of the island is $\approx 5.7\,\mathrm{nm}$ which is perfectly matching with the lateral distance between the elbows of the herringbone.

After studying cobalt growth on gold in its initial stage, the growth of closed cobalt films is of interest. During the course of this work, the deposition rate of cobalt and other evaporation parameters were essentially maintained. In order to achieve a higher coverage which ultimately results in closed films and to achieve different film thicknesses the deposition time was increased or decreased, respectively. Figure 4.3 shows two different samples (top row and bottom row) with closed epitaxial Co films, each grown on a Au(111) surface of a gold single crystal.

Figure 4.3(a) and (b) both show the very same sample with a closed cobalt layer grown epitaxially on a gold single crystal. The gold single crystal has been Ar-ion sputtered with the same parameters as the sample in Fig. 4.2 and annealed subsequently at 620° C to form a clean and well ordered Au(111) surface. After the gold crystal was cooled back to room temperature, the cobalt was deposited. The deposition parameters of the rod triple evaporator were $I_{\mathrm{Fil}} = 1.97\,\mathrm{A}$ and $U = 804\,\mathrm{V}$ with Flux $\approx 55\,\mathrm{nA}$. The deposition time was 90 min, the sample temperature was room temperature and the pressure in the preparation chamber did not exceed $1.19 \times 10^{-10}\,\mathrm{mbar}$ during the deposition. The layer thickness of the deposited Co has been assumed to be in the range of 4-5 nm (see discussion at the end of this

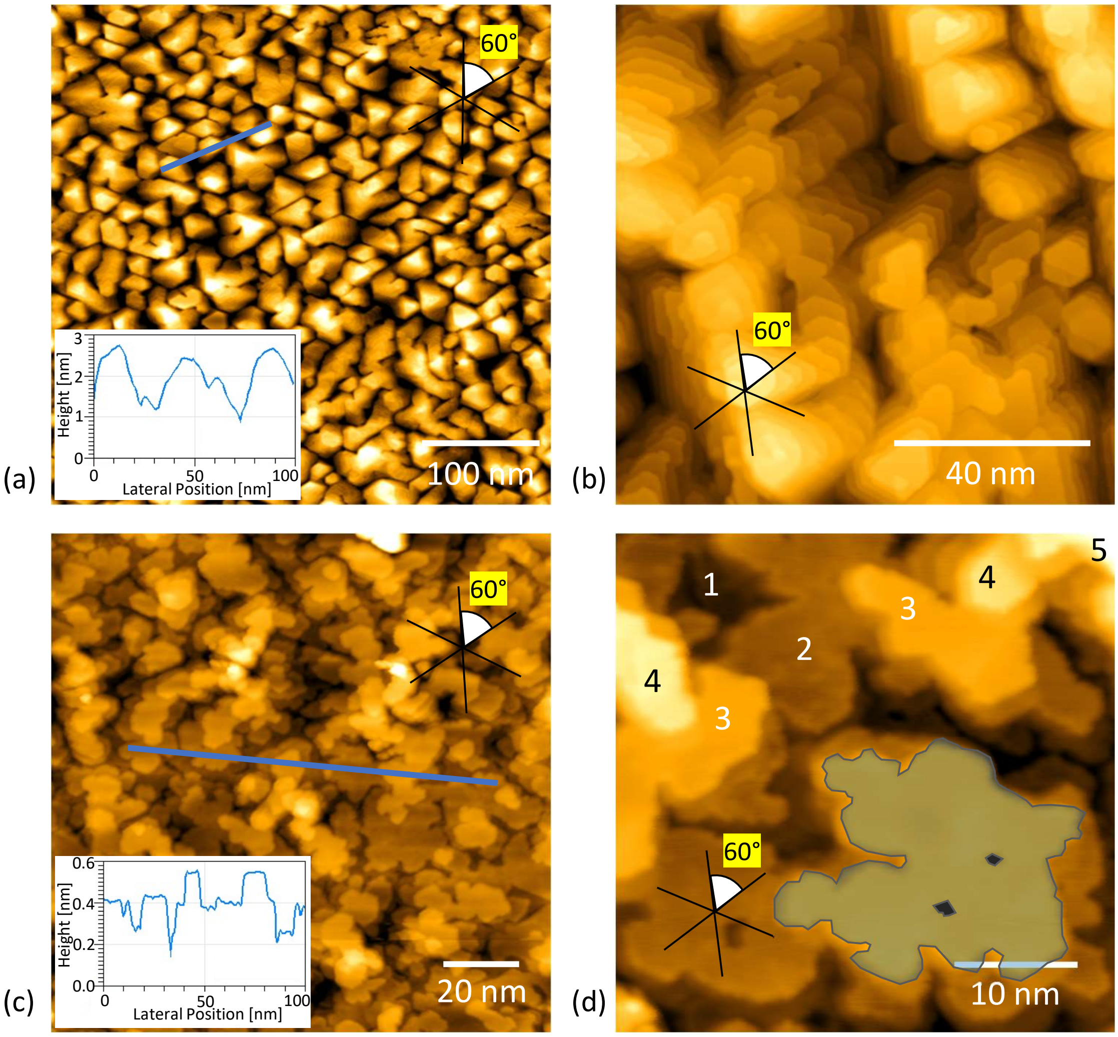

Figure 4.3: (a) STM of closed 4-5 nm Co(0001)/Au(111). The insert shows the linescan marked by the blue bar. ($500{\times}500\,\mathrm{nm}^2$, $V_{\mathrm{bias}} = 900\,\mathrm{mV}$, $I_{\mathrm{t}} = 1.0\,\mathrm{nA}$, $T = 4.8\,\mathrm{K}$) (b) Atomically flat mesas grow layer by layer with ever decreasing area of the top plateaus. ($100{\times}100\,\mathrm{nm}^2$, $V_{\mathrm{bias}} = 1.5\,\mathrm{V}$, $I_{\mathrm{t}} = 1.0\,\mathrm{nA}$, $T = 79\,\mathrm{K}$). (c) STM of $\leq 2.0\,\mathrm{nm}$ Co(0001)/Au(111) reveals a flatter surface with lower corrugation (cf. insert) ($137{\times}137\,\mathrm{nm}^2$, $V_{\mathrm{bias}} = 2.0\,\mathrm{V}$, $I_{\mathrm{t}} = 0.1\,\mathrm{nA}$, $T = 79\,\mathrm{K}$). (d) Zoom into the sample of (c) with large plateau areas (marked) at very few atomic layers (numbered) ($40{\times}40\,\mathrm{nm}^2$, $V_{\mathrm{bias}} = 2.0\,\mathrm{V}$, $I_{\mathrm{t}} = 0.1\,\mathrm{nA}$, $T = 79\,\mathrm{K}$).

Section). Afterwards there was no post treatment whatsoever and the sample has been transferred into the STM chamber "as is" and cooled down to LN_2 temperature. The resulting Co(0001) surface in Fig. 4.3(a), (b) consists of numerous coalesced polygonal cobalt island of a few nanometer height. The insert in Fig. 4.3(a) shows a 100 nm linescan (blue bar) and reveals a corrugation of $\approx 1.8\,\mathrm{nm}$. Figure 4.3(b) shows a much smaller area ($50 \times 50\,\mathrm{nm}^2$) of the very same sample. It becomes apparent that the coalesced cobalt islands consist of evenly grown mesas with flat steps and plateaus. These areas are atomically flat regions of clean (0001)-oriented cobalt and serve as the basis for the targeted interaction of adsorbed organic molecules with the hexagonal ferromagnetic structure.

In order to have an ideal and well-defined interface between Co(0001) and the targeted molecular organic layer of a device, one would like to have an atomically flat, perfectly ordered and in lateral direction infinitely extended uppermost surface. In our efforts to improve a real Co(0001) surface towards this ideal model and to aim for the lowest possible corrugation, I have tried to reduce the layer thickness so that the mesas are surrounded by less deep trenches, thus providing a larger net interaction area for the molecule/metal interface.

Figure 4.3(c) and (d) show a cobalt layer after a much shorter evaporation time to reduce the thickness of the layer and thus to keep the growth in height as low as possible. The underlying gold single crystal was prepared as before by sputtering and annealing, so that a clean and ordered Au(111) surface was obtained as substrate. The deposition parameters of the rod evaporator were $I_{\mathrm{Fil}} = 1.99\,\mathrm{A}$ and $U = 810 - 840\,\mathrm{V}$ with a Flux $\approx$ 59 nA. Adjusting the voltage was sometimes necessary to maintain the flux. Due to wear of the cobalt rod, the distance between filament and the material to be evaporated also varies over time, which further complicates reproducibility and makes readjustment of the voltage necessary. Except the voltage, the parameters were very similar to the samples before and only the deposition time was altered to $t_{\mathrm{deposition}} = 30\,\mathrm{min}$. The sample was kept at room temperature (RT) and the pressure in the preparation chamber did not exceed 1.9×10^{-10} mbar during the deposition. Although an estimation is not easy for the reasons mentioned above, I have assumed a Co layer thickness between 1.6-2.0 nm.

At first glance, it can be seen that the surface texture is different to thicker Co. It is considered that we see essentially the coalescence of the first few layers of cobalt. This has created large monatomically flat terraces with much shallower canyons. The insert in Fig. 4.3(c) shows a 100 nm linescan (blue bar) and shows a corrugation of $\approx$ 0.5 nm. In Fig. 4.3(d) the assumed five atomic layers which can be seen in this $40 \times 40\,\mathrm{nm}^2$ sample section and are marked by numbers. Five atomic layers of cobalt in <111> direction correspond[2] to a thickness of about 1.0-1.5 nm, which is somewhat below our estimated thickness of 1.6-2.0 nm. This can either mean that we do not see all terraces or floors of the Co layer, or that we are below the estimated

---

[2] This depends on the phase of the cobalt film, cf. [76]

layer thickness. An indication of the latter is given by looking at the morphology of the terraces.

The gray-marked area in Fig. 4.3(d) is a monatomically flat plateau and represents the ideal interface for molecule/metal interaction. The area of this terrace is $A = 305\,\mathrm{nm}^2$ and is therefore much larger than the average[3] area of the top layer of the thicker Co films. The morphology is not that of the triangular two-layered cobalt islands of the initial nucleation phase. Obviously, the sample is in the middle of the coalescence phase where the first few mono layers grow together, but no triangular areas have yet formed that grow upwards (cf. Fig. 4.3(a)), as described by [76] and [88] among others. If we compare the results from Fig. 4.3(d) with the STM data of [88], the similarity becomes immediately obvious. Nefedev et al. show a Co(111) surface with four terraces for the case of 1.5 ML Co on gold. Thus, I assume that the sample has between 1.5 and 2.5 nm Co deposited on the gold single crystal. Consequently, the five levels of the cobalt layer are actually the first five layers directly on the gold substrate and thus no quasi bulk cobalt. This is important because it was shown that in the first monolayers during Co growth not only a phase transition from hcp to fcc takes place [89], but also a layer-dependent change in ferromagnetic coercivity [90]. This correlation was confirmed by Monte Carlo simulations with underlying Ising model [91].

Since an exact determination of the underlying monolayers and thus of the physical properties is extremely difficult in practice, I decided to use thicker cobalt layers despite their higher corrugation. Furthermore, despite lower corrugation and larger atomically flat areas, these thin layers have also proven to be unsuitable for the devices in practice. It has been found that on the surface, despite the locally very low corrugation, there are high and steep islands of 2 nm height[4] at larger distances of several hundred nanometers. This makes the surface of Fig. 4.3(c) and (d) unsuitable as substrate for the organic layer of a device. In Sect. 6.2.1 and 6.2.2 the growth of cobalt layers on epitaxially grown Au(111) is discussed using two different substrate systems. The following investigations were carried out on cobalt layers as discussed above, i.e. on gold single crystals.

At this point it is important to emphasize that the flux of the triple evaporator is of course not a reliable and especially not a perfectly reproducible measure of the film

---

[3] Of course, even with thicker films, isolated areas or terraces with very large monatomic surfaces may occur. However, these are exceptional if present at all and are not representative. In the case of thin films of only a few monolayers, however, such large areas are present by default.

[4] Which is significantly higher than the estimated bilayer cobalt islands

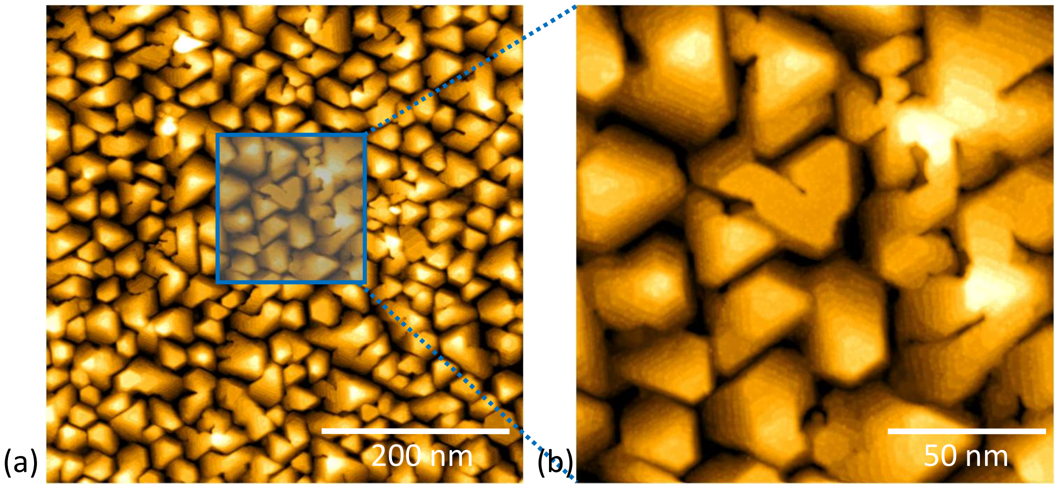

Figure 4.4: (a) Sub-ML coverage of BNTCDI on a closed Co(0001) BNTCDI/4-5 nm Co(0001)/Au(111) (500×500 nm^2, $V_{\text{bias}} = 1.5$ V, $I_{\text{t}} = 1.0$ nA, $T = 4.8$ K). (b) Zoom into the region marked in (a) reveals that BNTCDI is sublimable and evenly distributed over the flat plateau areas of the Co mesas which shall serve as interface region between the ferromagnetic Co and the organic molecules. Depending on the print quality, the molecules can most likely be identified as the "roughened" surface of the largest flat mesa in the center of (b). Since the sections are large compared to the molecules, identification by eye may be difficult. The same area with better visible molecules and adjusted contrast is also shown in Fig. 5.4 (150×150 nm^2, $V_{\text{bias}} = 1.5$ V, $I_{\text{t}} = 1.0$ nA, $T = 4.8$ K).

thickness. Nevertheless, it is the best indicator available for the triple evaporator in combination with the evaporation time. By viewing the STM images it is also quite easy to judge whether the thickness is in the range of only a few monolayers or a few nanometers due to the quite different appearance (cf. discussion above). For this reason, the given thicknesses of Co layers produced in this way have a certain degree of uncertainty though, but are nevertheless given for the sake of completeness. The situation is different for the test devices of Chapter 6, where a quartz balance was available for the crucible evaporator, which monitored the layer thicknesses. Since the appearance of films with monitored and estimated thickness are in good agreement with each other, the deviations in the thicknesses estimated on the basis of the flux are considered to not show any substantial error.

The very same sample as in Fig. 4.3(a) has been used to deposit < 1 ML of BNTCDI molecules. Figure 4.4 shows STM maps of the resulting sample. The deposition parameters, the yield of intact molecules and the characteristics of deposited BNTCDI molecules on Co(0001) will be discussed in Sect. 5.2.

Chapter 5

BNTCDI on Co(0001)

As shown by Raman et al. [9, 12] (see Sect. 3.3.2), certain organic molecules have very interesting properties when deposited on a ferromagnetic, metallic surface as Co(0001) or Co(111). The molecules which were mainly investigated in the course of this work are 2,7-dibenzyl 1,4,5,8-naphthalenetetracarboxylic diimide (BNTCDI) (see Fig. 5.1 for the structure formula). BNTCDI molecules have been deposited by evaporation on epitaxial cobalt films under UHV-conditions. The cobalt film is usually grown on a Au(111) single crystal as described in the previous chapter. For the properties of several stacked layers of BNTCDI in a mesoscopic device, functioning as organic tunneling barrier, see Chapter 6. There, the cobalt films were grown on gold buffer layers which were deposited on insulating substrates as mica or sapphire. If not stated otherwise I used Au(111) single crystals as substrate for the Co layer.

BNTCDI has been chosen due to envisioned applications in spintronic devices, cf. Sect. 3.3.2. The device principle envisioned in the long run will be outlined in Chapter 7. In this regard, BNTCDI can be seen as a precursor molecule to donor-acceptor dyads. In the targeted actual donor-acceptor dyads, it is considered to generate a charge transfer between the different moieties of the dyad by external stimuli. The feasibility of charge transfers in donor-acceptor-dyads have been proven among others by [93, 94, 95]. In this chapter, the feasibility of the intact deposition on epitaxial magnetic surfaces with high yield, the adsorption geometry of both the single molecule and monolayers and the electronic properties of BNTCDI/Co(0001) will be discussed.

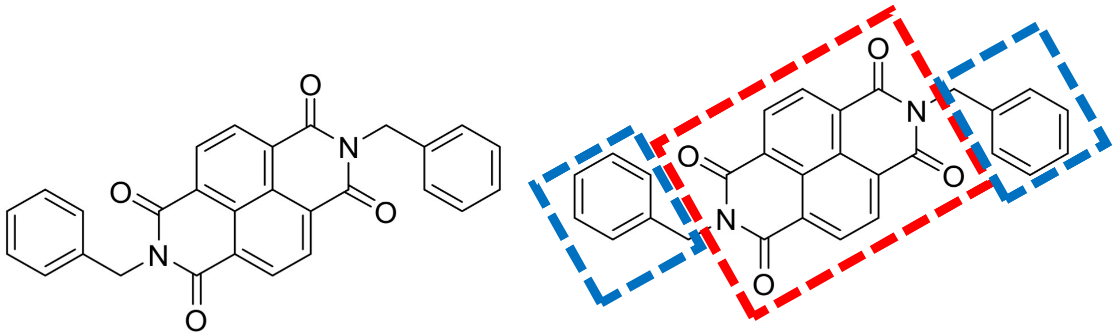

Figure 5.1: left: Structure formula of 2,7-dibenzyl 1,4,5,8-naphthalenetetracarboxylic diimide (BNTCDI), taken from [92]. right: Structure formula with marked backbone (red box) of the molecule. The phenyl groups (blue box) can be considered as placeholders for actual donor molecules. Due to the single bond between the nitrogen atom and the phenyl groups, the phenyl groups are freely rotatable. This circumstance will play a crucial role in determining the adsorption geometry, cf. Sect. 5.2.2 and Sect. 5.3.

5.1 On BNTCDI

All molecules used in the course of this work were synthesized and supplied by the group of Prof. Thomas J. J. Müller from the Heinrich Heine Universität in Düsseldorf. For a detailed information about the synthesis see Chapter 5.3.2 of [92]. For the sake of completeness, the synthesis of BNTCDI will be introduced and the molecule will be described briefly.

As discussed in Sect. 3.3 organic molecules can form magnetic entities on ferromagnetic metals by hybridization [9, 12]. It is considered that in the case of donor-acceptor-dyads a photo induced electron charge transfer (PIET) between the donor and the acceptor moiety may influence the electronic and magnetic properties of this new hybrid magnet making the magnetoresistance addressable by light. Towards such a suitable donor-acceptor dyad, BNTCDI forms a precursor molecule dyad.

More precicesly BNTCDI is a donor-NDI-triade. NDI stands for naphthalenediimides and photoinduced electron transfer in NDIs has already been described in the literature [96], [97]. NDIs in general are a well known class of molecules with a lot of applications. Similar molecules (NDIs) have been investigated before with respect to the adsorption e.g. on Au(111) [98] or on HOPG [99]. The potential of NDIs for wide applications as e.g. semiconductors [100] or organic transistors [101] are subject of a broad discussion.

One of the simplest naphthalenediimides (NDIs) is for example naphthalenetetracarboxylic diimide NTCDI wich is produced from the parent naphthalene via an intermediate compound naphthalenetetracarboxylic dianhydride (NTDA). Similarly, the naphthalene diimide derivative BNTCDI, which is the subject of this project, is to be developed from the commercially available NTCDA (see Fig. 5.2) and primary amines are synthesized.

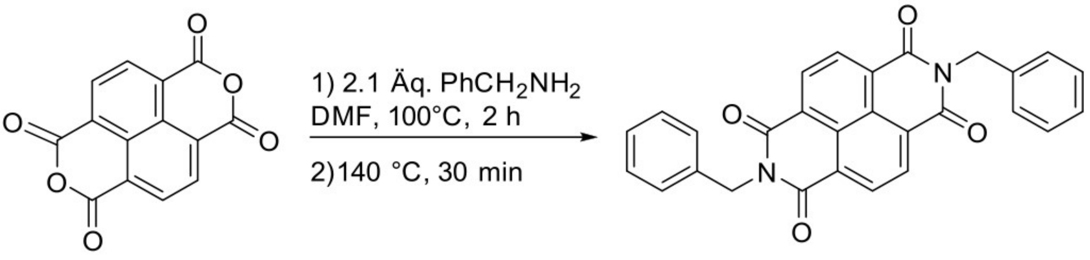

yield: 81 %

NTCDA

NDI derivate: BNTCDI

Figure 5.2: Synthesis of BNTCDI from NTCDA as described in and taken with minimal changes from [92].

To that end, 1,4,5,8-Naphthalenetetracarboxylic dianhydride (NTCDA) (1.34 g, 5.00 mmol) and benzylamine (1.17 g, 10.9 mmol) were dissolved in dimethylformamide (DMF) (20 ml) and subsequently stirred at room temperature for two hours. Afterwards, the resulting mixture was stirred at 100° C (373 K) for 2 h and at 140° C (413 K) for 30 min. The resulting suspension was doused in cold water and the sedimentation was filtered and then dried under vacuum conditions. Purification was performed by recrystallization from dichloromethane. The resulting 2,7-dibenzyl 1,4,5,8-naphthalenetetracarboxylic diimide (BNTCDI) has been supplied in powder form as a cream-colored solid of 1.82 g which equals a yield of 81%. As can be seen in Fig. 5.2, the benzyl groups have been attached at the position of the former oxygen atoms and have been anchored with highly reactive nitrogen atoms. The benzyl groups act as some kind of dummy load for actual functional groups of the future molecule. For details on synthesis, structure determination and chemical characterization of BNTCDI see [92].

The very pure BNTCDI, now in powder form, can be transported under atmospheric pressure and stored at room temperature, dark and dry, for a long time. While the synthesis of molecules is the task of chemists, the physicists want to investigate the interplay between the molecule and the metal substrate. Firstly, the molecules must be transferred into the vacuum in powder form and then deposited on the metal surface. Then the resulting properties of the interaction between the molecule and the metal have to be examined and evaluated first on a microscopic and later on a mesoscopic scale. The same molecules have been investigated on Pt(111) by Ebeling et al. [102]. As platinum is not ferromagnetic and little reactive (compared to cobalt), the molecular properties observed in [102] are considered similar to the gas phase and thus those of the molecule per se. In the following, the same molecule will be investigated on a highly reactive and ferromagnetic Co(0001) surface.

5.2 BNTCDI on Co(0001) - Microscopy

As described in Chapter 4, two evaporators for the deposition of BNTCDI were available. The crucible evaporator in the separate molecular chamber has proven to be the most practical and efficient method. Other than that, the evaporators are essentially the same. However, the use of a separate chamber has immense advantages. On the one hand, the other materials for evaporation i.e. metals stored in the preparation chamber do not become contaminated by sublimated organic material. On the other hand, changing the glass crucibles is much easier, since after aeration it is not necessary to pump, bake and degas the much larger preparation chamber with all its devices and materials, but only the considerably smaller molecule chamber. This separate chamber contains essentially nothing except the evaporator, the pumps, the pressure sensors and a quartz balance. Due to its much smaller size, bakeout and pumping is much easier and faster and almost nothing has to be outgassed, so that operating pressure, i.e. ultra high vacuum, can be reached again very quickly after opening.

Aeration of the molecular chamber becomes particularly necessary when organic material has to be changed, refilled or removed, or when conversions or repairs have to be carried out; which turned out to be necessary very often in the course of this work. Rather rarely it occurs that the organic material in the crucible is used up, since one filling of the crucible is usually sufficient for hundreds of samples. Much more often it may happen that the temperature in the crucible was a little bit too high and the organic material inside does not sublimate at all but changes its structure during baking (cf. Fig. 5.3). The crucible and the material in it have

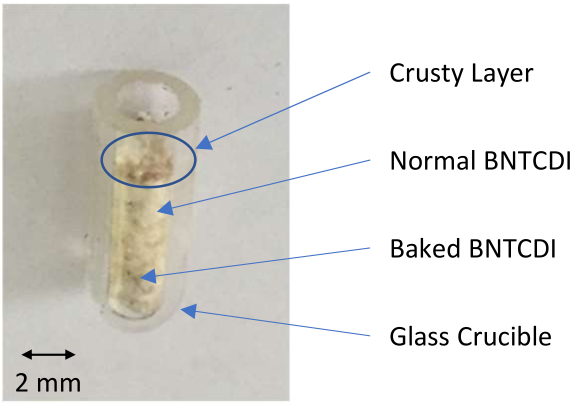

Figure 5.3: The photo shows a glass crucible with an opening cross-section of 4.5 mm^2 as used in the molecule evaporators of NSCT. After a 3 h treatment at 573 K the crucible turned out to be unusable. The BNTCDI stored inside has partially turned brown and has formed a hard crust on the surface. When I got the powder it looked as the white patches in the crucible.

to be replaced subsequently. Due to the advantages mentioned above, the separate molecule chamber was used for most of the deposition cycles of Chapter 6 since extremely long evaporation times where necessary there. The immense advantage for using the evaporator in the preparation chamber is the much faster sample preparation and that the transfer chamber does not have to be passed through. The transfer chamber usually has a slightly higher base pressure than the preparation chamber of $> 1 \cdot 10^{-10}$ mbar.

5.2.1 Evaporation Parameters

First the suitable evaporation parameters must be determined. Evaporation parameters here and in the following are the temperature in the crucible of the evaporator and the net deposition time. It has been found that the evaporator heating has to be started up slowly and step by step and that the suitable sublimation temperature lies within a relatively small temperature interval. As already mentioned, too high temperatures can change the solid organic material in such a way that the crucible subsequently becomes clogged or encrusted and must be replaced. Thus, a proper set of parameters of temperature[1] and exposure time has to be found experimentally. Note that unlike other organic deposition approaches where the sample is cooled during molecule deposition to decrease the mobility of adsorbed molecules

---

[1] Determined by voltage and current of the evaporator heating

[103], the temperature of the sample was always room temperature.

Rate and Coverage

As mentioned in Sect. 4.3, cobalt layers of varying thickness were investigated. Molecules were placed and examined both on thin (a few monolayers) and thick (a few nanometers) layers. The investigation is generally easier on the large areas of the thin layers. However, as already mentioned, they are problematic or completely unsuitable for use in devices. For this reason, the deposition of BNTCDI on thick layers has been investigated as well. During the investigations it turned out, that the deposition rate of BNTCDI was hard to detect by the quartz balances of our system. Therefore, a rate had to be determined from the sublimation parameters that would allow conclusions on the coverage, especially with respect to the targeted closed layers.

Figure 5.4 shows the very same sample as Fig. 4.3(a,b) and Fig. 4.4. Consequently, the preparation parameters for the Co(0001) substrate are as described in Sect. 4.3. After the STM examination of the Co(0001) substrate, the sample was transferred from the STM through the preparation chamber and the transfer chamber into the molecule chamber and warmed up to RT. In the meantime, the molecular crucible evaporator located in the molecular chamber and closed with a shutter was started up. The deposition time was defined precisely with said shutter. In order to prevent the above-mentioned incrustation of the crucible (see Fig.5.3), the evaporator was started up very slowly and step wise. In addition, numerous intermediate examinations had to be performed after each step to avoid accidentally missing the sweet spot and permanently evaporating too hot. Especially because the crucible comes into thermodynamic equilibrium very slowly and if one starts up too fast one has to deal with a very strong temperature offset and the temperature continues to rise uncontrolled. The temperature of the evaporator is set by the applied current and monitored by a thermocouple. The thermocouple was read out by means of a multimeter. The used step size was 10 mA with about 15-20 min waiting before the current was increased further. It turned out later in the course of the measurements that the evaporator can also be started up with 100 mA steps with a waiting time of 1 h each, which accelerated the overall start up and still led to reproducible results.

The parameters used for the sample in Fig. 5.4 were $I = 0.25\,\mathrm{A}$, $V = 6.0\,\mathrm{V}$, $T = 270^\circ\,\mathrm{C}$ (543 K) with a deposition time of $t_{\mathrm{deposition}} = 60\,\mathrm{s}$. The pressure in the molecule chamber increased from a base pressure of $< 5.0 \times 10^{-10}$ mbar up to 1.3×10^{-9} mbar. Although the molecule chamber was equipped with a quartz balance, a rate was hardly detectable at all. Thus, the increase in pressure was the most reliable indicator that a significant evaporation of molecules had begun. Of course, the pressure also increases due to local outgassing and heating, contamination and opening of the chamber valve. It was therefore necessary to check after each step in the STM whether there were actually molecules on the sample. After a large number of runs, one had a feeling for the mixture of temperature and pressure increase in order to deposit molecules reproducibly and without intermediate testing. It also turned out that it is useful to wait at least one hour after setting the final current value (in the above sample 0.25 A). Usually the crucible was then closer to equilibrium and the (evaporation) temperature could be kept more constant.

Figure 5.4 shows a sample after one minute deposition at 270° C. As can be seen in Fig. 5.4(a) the sample is covered quite homogeneously with a sub-monolayer (ML) of BNTCDI molecules. All floors, terraces and plateaus show a certain amount of molecules. The grey marked zone[2] is a monatomically flat plateau and has an area of $869\,\mathrm{nm}^2$ and therefore favorable for STM investigations. Particularly since molecules tend to arrange along step edges due to the changed coordination number. Note that this is an unusually large monatomic area for such a thick Co layer and was specially selected for the study.

Figure 5.4(b) shows a zoom onto the marked plateau of Fig. 5.4(a). When processing the STM measurement, a very hard contrast was chosen in order to distinguish the molecules as clearly as possible from the underlying cobalt. On the surface of the terrace there are 145 molecular units, which were marked by the red transparent bars. With an area of $869\,\mathrm{nm}^2$ this corresponds to a density of $\rho_{270^\circ} = 0.167\,\frac{\mathrm{molecules}}{\mathrm{nm}^2}$ after 60 s at 270° C which equals a rate of $R_{270^\circ} = 2.78 \cdot 10^{-3}\,\frac{\mathrm{molecules}}{\mathrm{nm}^2 \cdot \mathrm{s}}$.

To verify the result, another similarly large area was searched on the same sample and has also been examined for molecular density on the surface. The same procedure has been performed on that even larger area of the same sample. Here are 261 molecular units on a $1437\,\mathrm{nm}^2$ atomically flat terrace (cf. Fig. 5.5(a)). This corresponds to a density of $\rho_{270^\circ} = 0.182\,\frac{\mathrm{molecules}}{\mathrm{nm}^2}$ after 60 s at 270° C which equals a rate of $R_{270^\circ} = 3.03 \cdot 10^{-3}\,\frac{\mathrm{molecules}}{\mathrm{nm}^2 \cdot \mathrm{s}}$, which is slightly above than the findings on the smaller area but statistically comparable. Besides the larger surface area, which leads to different influence of the edge and normal statistical variations, a main problem in

---

[2] Not to be confused with the blue box which is just a guide to the eye and equals the area shown in Fig.5.4(b).

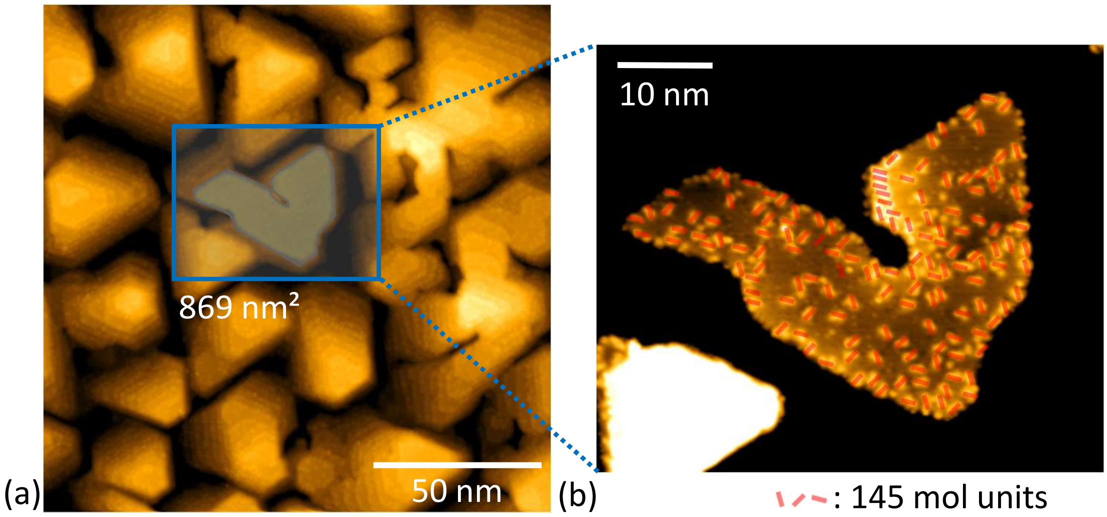

Figure 5.4: (a) STM of the same sample as Fig. 4.4 after deposition of $< 1\,\text{ML}$ BNTCDI. The marked area is the plateau of a mesa and corresponds to $869\,\text{nm}^2$ ($150{\times}150\,\text{nm}^2$, $V_{\text{bias}} = 1.5\,\text{V}$, $I_{\text{t}} = 1.0\,\text{nA}$, $T = 4.8\,\text{K}$). (b) The zoom reveals the coverage of the mesa plateau. Each molecular unit in the area is marked with a transparent red bar.

determining the rate is the identification of the individual molecular units.

Figure 5.5(b) shows a zoom onto the marked area in (a) on the cobalt terrace but without the red transparent molecular unit markers. The high contrast has been chosen to emphasize the shape of the molecular units. It becomes apparent that the shape of these units is not always identical and it is somewhat difficult to determine whether the unit is an actual molecule or just a torn off part such as a benzyl group (cf. Fig. 5.5(b)). This raises the question not only for the rate but also for the yield of intact molecules, which will be discussed later on.

As described in Chapter 4, the NSCT has two molecule evaporators. One in the separate molecule chamber and one in the preparation chamber. Both evaporators are basically identical in construction and use the same glass crucibles for the molecules. However, the chamber geometry, distance between evaporator and sample and the pressure conditions are different. For comparison, Fig. 5.6 shows a thinner Co sample of $\approx 1.6\,\text{nm}$, similar to the film in Fig. 4.3(c) and (d), which was grown in the preparation chamber and on which molecules were subsequently deposited in the preparation chamber as well. The gold single crystal has been treated as usual and the evaporation parameters for the Co rod evaporator were: $I_{\text{Fil}} = 1.99\,\text{A}$ and $U = 810 - 840\,\text{V}$ with a flux of $\approx 59\,\text{nA}$ with $t_{\text{deposition}} = 30\,\text{min}$. The sample was

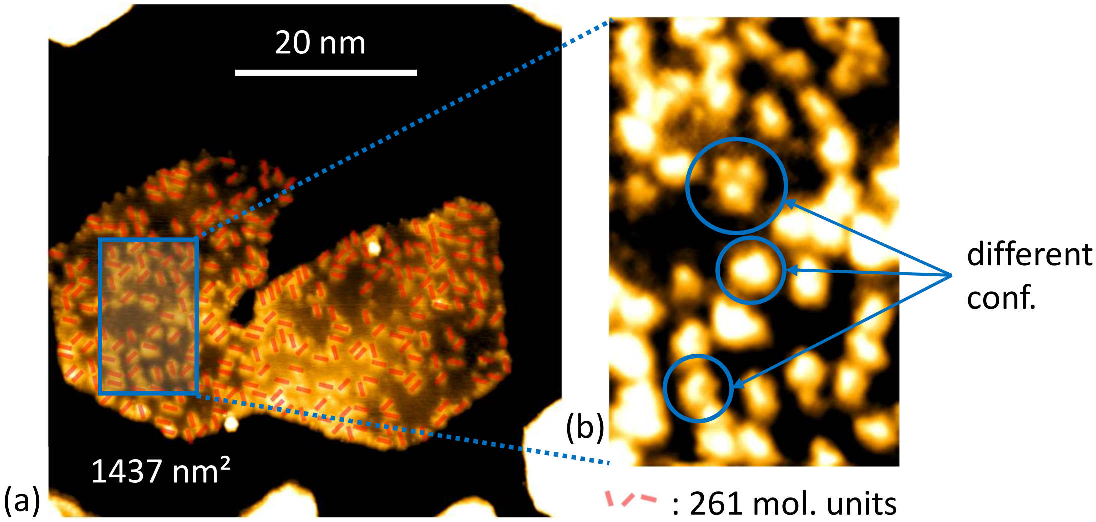

Figure 5.5: (a) STM of another mesa with an area of 1437 nm^2 with a higher coverage of molecular units (marked) ($60\times 60\,\mathrm{nm}^2$, $V_{\mathrm{bias}} = 0.9\,\mathrm{V}$, $I_{\mathrm{t}} = 1.0\,\mathrm{nA}$, $T = 4.8\,\mathrm{K}$). (b) Zoom into the marked area in (a) with intentionally harder contrast reveals that not all molecular units have the same configuration.

kept at room temperature (RT) and the pressure in the preparation chamber did not exceed 1.9×10^{-10} mbar during the deposition.

The parameters used for molecule evaporation in Fig. 5.6 were $I = 0.26\,\mathrm{A}$, $T = 260^\circ - 270^\circ\,\mathrm{C}$ (533 - 543 K) with a deposition time of $t_{\mathrm{deposition}} = 300\,\mathrm{s}$. The pressure in the preparation chamber did not exceeded 4.0×10^{-11} mbar, which is extremely low for a preparation chamber during sample preparation. Note that the thermocouple of the molecule evaporator showed a lower temperature despite the higher current. Overall, the temperature continued to rise for hours, so that the measured temperature in the first hour after setting the final value is approximately between 220° C and 270° C degrees. The exact values are therefore difficult to determine. After about an hour the value was always around 270° C, so this is considered the specified final temperature here and in the following.

As can be seen in Fig. 5.6(a), the surface shows the characteristic flat terraces and not the triangular plateaus of the thicker Co layers. In principle, this makes an examination easier. The two marked areas correspond to a total area of 843 nm^2 and are shown enlarged in Fig. 5.6(b). Here there are 73 molecular units on 843 nm^2 (cf. markings in Fig. 5.6(b)). This corresponds to a density of $\rho_{270^\circ} = 0.087\,\frac{\mathrm{molecules}}{\mathrm{nm}^2}$ after 300 s at 270° C which equals a rate of $R_{270^\circ} = 2.89 \cdot 10^{-4}\,\frac{\mathrm{molecules}}{\mathrm{nm}^2\cdot\mathrm{s}}$.

It is noticeable that this rate is an order of magnitude smaller than that the rate of the evaporator in the molecule chamber, despite having approximately the same temperature. It is obvious that the rate depends very much on the evaporator used and/or the whole configuration (chamber geometry, sample distance and condition of the heater or filaments) and has to be determined each time something is changed. However, it should be emphasized that the rates for the individual evaporators were largely reproducible in the same setup. Therefore, the rates for the individual evaporators determined here will be used in the following. Another factor influencing the rate is the yield of intact molecules on the surface, since it obviously makes a difference whether a molecule breaks and is then counted as several molecular units (which are actually molecular fragments) or not. This holds in particular in the scope of closed layers of intact molecules in the envisioned devices.

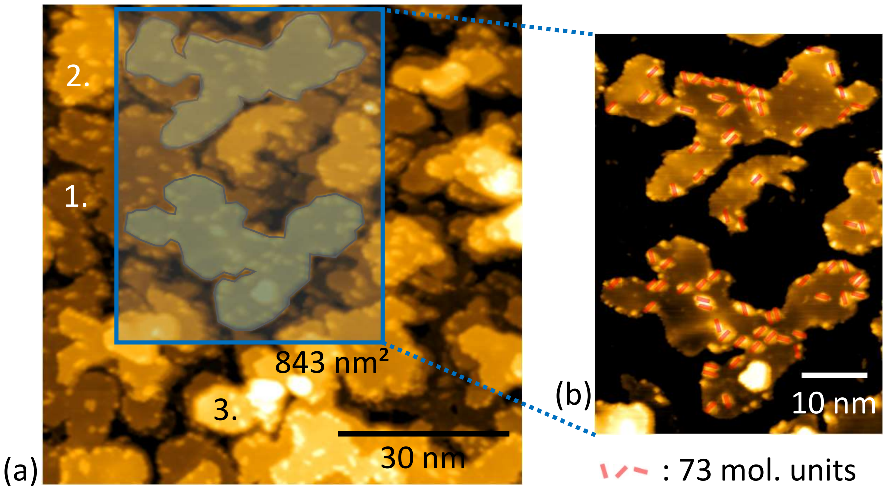

Figure 5.6: (a) STM of a thinner Co film with a BNTCDI coverage quite below 1 ML. Three atomic levels are labeled and offer a general larger potential interface are. The marked area has a total of $843\,\mathrm{nm}^2$. ($80{\times}80\,\mathrm{nm}^2$, $V_{\mathrm{bias}} = 0.7\,\mathrm{V}$, $I_{\mathrm{t}} = 1.0\,\mathrm{nA}$, $T = 78\,\mathrm{K}$). (b) Zoom ($40{\times}57\,\mathrm{nm}^2$) of the investigated area with 73 mol units. Contrast has been adjusted.

Note also that the rate is determined for sub-monolayer coverage only. At >1 ML the determination of the rate or the coverage becomes very difficult if not impossible, because thick layers have extremely high electrical resistances and cannot be mapped with STM without further ado. On the other hand, it has turned out that the molecules adhere much worse to molecules than to clean and highly reactive cobalt. This has obviously a massive impact on the adsorption rate for a coverage beyond 1 ML which turned out to be of great importance for the further course of this work. The problem of non-adhesive molecules will become very relevant for the devices where thick and closed organic layers have to be produced and are crucial for a working tunneling barrier. This problem will be discussed Sect. 6.5. Therefore, here and in the following the rate is not given in $\frac{\text{ML}}{\text{s}}$ as usual, but in $\frac{\text{molecular units}}{\text{area}\cdot\text{s}}$ and the sub ML results cannot be simply transferred or extrapolated to growth in z-direction.

After all, it turned out that the sublimation of BNTCDI demands a quite narrow temperature interval, where 260° C to 270° C seem to work best. As mentioned before, if the temperature is too low, there is no sublimation at all, while if its slightly to high, the crucible encrusts and no deposition is possible either. The rate turned out to not correlate with the temperature as much as expected, thus with respect to the temperature it is an event of type On or Off. On the other hand, the deposition time did not show a strong correlation to the deposited amount either, which is surprising. Samples have been fabricated with only a few minutes deposition time which showed an coverage close to a monolayer while other samples with basically the same deposition time had considerably lower coverage or even only a few single molecules. It seems that the individual batch of molecule flakes (which had to be changed frequently during this work) and the the arrangement of the molecule flakes within the crucible have a much bigger influence on the actual rate than the parameters discussed above.

Since the molecules are in the form of dry flakes when I got them from the chemists, it seems reasonable that the thermal coupling of individual flakes to the crucible wall is better or worse. It is therefore conceivable that a flake on top is poorly coupled and blocks the "exit" of the crucible for sublimed molecules from further down the crucible.

Therefore, suitable parameters must be determined anew for each batch of molecules, in particular with regard to the coverage-time relationship. The temperature-coverage relation seems to have a negligible if any influence. Instead, it seems necessary to stay within the relatively narrow temperature window described above to allow deposition but not to crust the crucible.

Yield of Intact Molecules

Since the functionality of the mesoscopic devices is based on the interaction or tunneling properties between cobalt and the organic molecular layer, it is essential to have information about whether closed layers of intact molecules on the cobalt can be produced at all. As mentioned before that raises the question for the yield of intact molecules on the surface. In general, three configurations can be observed at low coverage, ie. significantly below a monolayer. Most of the observed molecular units turned out to be molecular fragments, which can be recognized by their shape. Mostly intact molecules were also found which are not only symmetric along their longitudinal axis but also mirror-symmetric along their transversal axis showing a $C_{2\mathrm{v}}$ symmetry.

Figure 5.7 shows a STM image of $\ll$ 1 ML BNTCDI on 4.8 nm Co(0001). The molecules were evaporated in the molecule chamber at 270° C. The evaporation parameters were $I = 0.25\,\mathrm{A}$, $V = 6.0\,\mathrm{V}$, $T = 270^\circ\,\mathrm{C}$ (543 K) with a deposition time of $t_{\mathrm{deposition}} = 60\,\mathrm{s}$ with the pressure in the molecule chamber not exceeding 1.3×10^{-9} mbar. At such a low coverage produced with these evaporation parameters there are essentially three configurations of molecular units. In Fig. 5.7(a) these three configurations are marked. The most common configuration for such samples is the fragment of a decomposed molecule. The shape of this unit is mirror-symmetrical with respect to the longitudinal axis. The shape is reminiscent of small fish and there is no doubt that these are not intact BNTCDI molecules. However, it is not quite clear what atomic configuration this fragment has. It seems obvious that one of the phenyl groups is torn off. However, it is not clear whether only the benzene ring is missing or whether the whole phenyl group is broken off maybe together with the nitrogen atom. It may well be that the nitrogen atom is the weak point of the molecule.

The second configuration is labeled as phenyl group in Fig. 5.7(a). It should be noted, however, that the exact atomic configuration is not conclusively clarified here either. Yet it is rather obvious that it is the missing phenyl group or the missing benzene ring of the first configuration, namely the molecular fragment. This assumption is in good agreement with the data even after measuring this second configuration with a line scan. The lateral size of the object is approximately 0.5 nm (5 Å) which is slightly larger than an ideal benzene ring 380 pm ($\approx$ 4 Å). However, the electron distribution of the molecule is not taken into account in that size. Yoon et al. have mapped benzene rings with STM on Rh(111) and have measured a size of 5 Å for flatly adsorbed rings on the surface [104]. Rhodium is chemically similar to cobalt, as it is one period higher than cobalt in the periodic table but in the same group it has a comparable electron configuration. It is a 4d transition metal while cobalt is a 3d transition metal. Furthermore, both surfaces are hexagonal and thus topographically similar as well. For these reasons I consider the results comparable and consider this second configuration as a benzene ring or as a phenyl group.

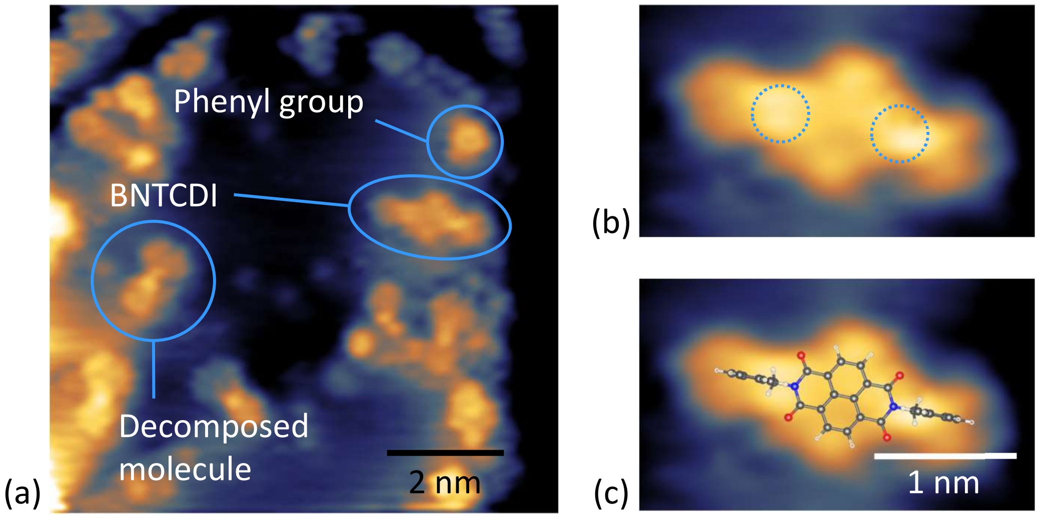

Figure 5.7: (a) STM of BNTCDI/Co(0001)/Au(111) with three different molecular configurations. The marked configurations are labeled with the assumed character of each configuration. ($8{\times}8\,\mathrm{nm}^2$, $V_{\mathrm{bias}} = -1.0\,\mathrm{V}$, $I_{\mathrm{t}} = 1.0\,\mathrm{nA}$, $T = 77\,\mathrm{K}$). (b) Zoom on an intact BNTCDI molecule with two characteristic bright spots (marked) which correspond to the N-H bonds within the molecule. (c) The same zoom with the BNTCDI structure formula [105] which is to scale in order to compare the intramolecular features with the model. The color scale was chosen to emphasize the shape of each configuration.

Finally, the third and final configuration was identified beyond doubt as an intact BNTCDI molecule. The adsorption position and electronic properties of the molecule on Co(0001) will be discussed in detail later. For now, it is sufficient to identify this molecule as an intact molecule. As shown in Fig. 5.7(b), even submolecular resolution has been achieved with STM whereby the internal structure of the molecule becomes visible. The blue circle emphasize two bright peaks with increased conductance which will be discussed later (see Sect. 5.2.2). In Fig. 5.7(c) a size-matched structure formula of BNTCDI has been inserted in order to compare the size and the submolecular features with the model. Both size and shape fit well with the model and the features can be attributed. It is assumed, that the oxygen atoms have a minor influence on the STM measurement, so that the shape, symmetry, structure and size of the measurement fit the model very well. Note that the phenyl groups are considered to point upwards hence the mirror symmetrical shape along the longitudinal axis. In fact, this characteristic makes it difficult to measure BNTCDI properly with STM compared to flatly adsorbing molecules like otherwise comparable NDIs or numerous other flatly adsorbed aromatic molecules. The upright standing phenyl groups are much less stable and the interaction with the tip of the STM is very strong, so that a clean sub-molecular image requires a lot of patience and time.

After the identification of the three configurations of the molecular units, it is not completely clear how the two fragmentary units are composed. Although there are reasonable assumptions, this is of secondary interest for the production of the intended devices and can be investigated in more detail in the future. Investigations on single intact molecules are also possible with the samples shown so far without any problems, because usually at least one intact molecule could always be found somewhere on a clean spot, although it sometimes took some time to find one. However, since the interaction between large quantities of intact molecules (essentially completely closed layers) and the top layer of cobalt is to be used in the intended devices, the samples shown so far with only a few and occasionally occurring intact molecules are useless for the production of devices. Therefore it is necessary to achieve a coverage as high as possible ($\geq$ 1ML) with as many intact molecules as possible. In particular, such films must be reproducible and practicable to fabricate. For this purpose one has actually only a few adjustment screws. One may change the temperature profile applied to the crucible; if the molecules are already destroyed in the crucible during the warm up (instead of upon adsorption) this may help to deposit more intact molecules on the surface and thus to increase the yield. Furthermore, the evaporation time may be increased, which did not show the expected correlation with the coverage (cf. discussion on the rate). It has also turned out in numerous experiments that the warm up speed of the evaporator should be very low in order to obtain particularly good results with a high yield of intact molecules.

Figure 5.8(a) shows a $60 \times 60\,\mathrm{nm}^2$ STM image of a sample of 5 nm Co(0001) grown on an Au(111) single crystal. The molecular evaporator was ramped up over a 2.5 h period. The molecular deposition parameters were: $I = 0.23\,\mathrm{A}$, $T = 258^\circ\,\mathrm{C}$ (531 K) with a deposition time of $t_{\mathrm{deposition}} = 80\,\mathrm{s}$ with the pressure in the molecule chamber not exceeding $1.8 \times 10^{-9}\,\mathrm{mbar}$. Thus, the evaporation temperature was slightly lower than for the above sample, with a slight increase of the evaporation time. The characteristic triangular mesas show the typical step growth of cobalt of this layer thickness. The hard, monochrome and on each layer alternating contrast was chosen with the intent to make all surface steps visible in the same image. Thus, it is easy to see that each terrace is uniformly covered with molecular units of BNTCDI. The total coverage is slightly below a monolayer. Obviously, the coverage has been increased successfully. However, a closer inspection reveals that the molecular units, although homogeneous and identical in appearance, are not mirror symmetric with respect to their transversal axis. All molecular units are of the first configuration (see "fishes" above) and thus molecular fragments. The yield of intact molecules is therefore almost zero on this sample.

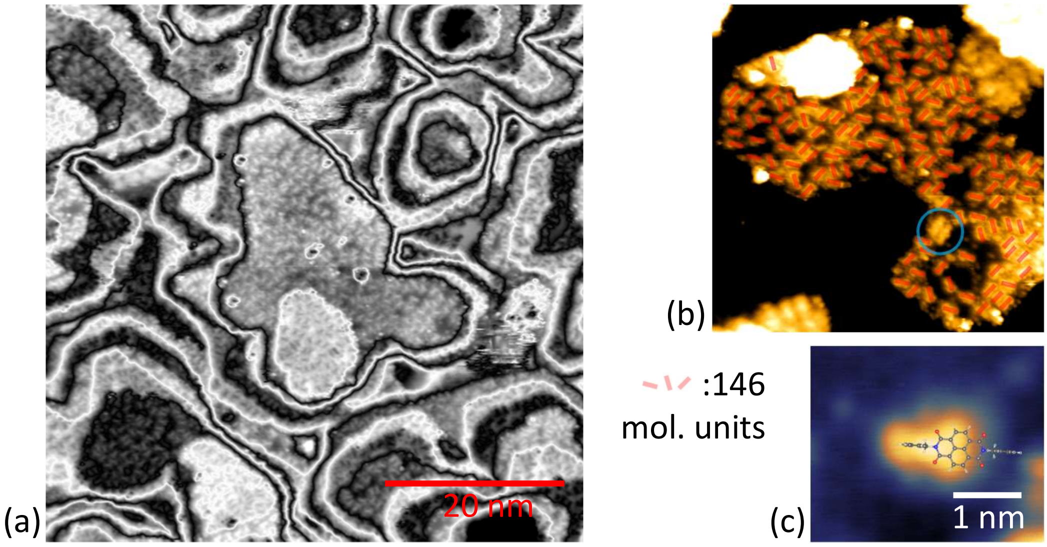

Figure 5.8: (a) STM image whith ultra-hard and alternating contrast to even out the depths of the valleys and to emphasize that the coverage is close to a ML on any layer. Basically all molecular units are of configuration 1 though. The yield of intact BNTCDI molecules is close to zero. ($60\times60\,\mathrm{nm}^2$, $V_{\mathrm{bias}} = 300\,\mathrm{mV}$, $I_{\mathrm{t}} = 500\,\mathrm{pA}$, $T = 79\,\mathrm{K}$). (b) Zoom onto a Co mesa of the same sample with 146 molecular units the mesa surface. The blue circle marks the only two intact molecules on the whole area. (c) Zoom on a molecular unit in configuration 2 with a size-adjusted structure formula and the same color scale as Fig. 5.7 reveals that the molecule apparently breaks in the region of the nitrogen atom ($3.5\times3\,\mathrm{nm}^2$, $V_{\mathrm{bias}} = -100\,\mathrm{mV}$, $I_{\mathrm{t}} = 1.0\,\mathrm{nA}$, $T = 4.6\,\mathrm{K}$).

To examine this in more detail, Fig. 5.8(b) shows a detail image of a cobalt mesa with almost full coverage. At its surface 146 molecular units can be identified. The transparent red bars mark molecular fragments of configuration 1 ("fishes"). The only two intact BNTCDI molecules are marked by the blue circle and are arranged parallel to each other with a slight offset. Measured from this detail image, the yield on this sample with these evaporation parameters is thus less than 1.4 %. The STM image in Fig. 5.8(c) shows a detailed picture of a molecular fragment of configuration 1. The image was adjusted to match with Fig. 5.7(c) in color scale and contrast. The inserted molecular model of BNTCDI is size matched and shows well which part of the molecule is absent. Obviously, a phenyl group is missing completely. It seems that the molecule has broken apart at the nitrogen atom. The nitrogen atom with the phenyl arm above it otherwise contribute to the bright spots in STM (cf.

Fig. 5.7(b)).

Apart from this issue, the experiments have shown that a lower temperature with approximately the same deposition time does not seem to have any effect on the yield of intact BNTCDI molecules. It can be concluded that the molecules do not break in the crucible due to too high evaporation temperature. At even lower temperatures, the molecules were not evaporable at all. As mentioned before, the investigation of thick organic multilayers ($\geq$1ML) with STM is difficult or practically impossible. Nevertheless, it has been found in the experiments that as soon as the first mono layer BNTCDI is closed, the second layer on top of it grows much slower than the first layer that is in contact with cobalt. For this reason, I have switched to significantly increasing the second adjustment screw, namely the evaporation time.

Figure 5.9 shows a STM image of 4 nm Co(0001) grown on a Au(111) single crystal. The molecules have been deposited within a considerably longer time period. The evaporation parameters were: $I = 0.26\,\mathrm{A}$, $T = 260 - 275^{\circ}\,\mathrm{C}$ (533-548 K) with a deposition time of $t_{\mathrm{deposition}} = 26\,\mathrm{min}$ with the pressure in the molecule chamber not exceeding $1.3 \times 10^{-10}\,\mathrm{mbar}$. In spite of the long deposition time, the temperature within the evaporator continued to rise over the entire period, as discussed above. The temperature was therefore relatively high. Nonetheless, from Fig. 5.9 it becomes unambiguously apparent that the long evaporation time resulted in an almost closed monolayer of intact BNTCDI molecules only (yield $\lesssim$100 %). This again underlines that changes in temperature have virtually no effect on the yield of intact molecules. Instead, it has been surprisingly shown that a longer evaporation time increases the yield dramatically. Why that is, is not conclusively clear. Besides variations in the starting material or impurities, a statistical displacement of fragments by intact molecules could be discussed in the future.

The molecules are either already broken in their initial state or are destroyed upon sublimation or adsorption. The latter scenario, however, would also have to apply to long evaporation times, which is obviously not the case. Consequently, molecules seem to show statistically better adsorption than broken molecules/fragments, so that more intact molecules are found on the surface after long deposition times. The reason for this observation is completely unclear though. Coverage per se also does not seem to have a direct effect on yield, since high coverage have been produced with both extremely low and extremely high yields of intact molecules, as shown in Fig. 5.8 and 5.9. In any case, this behavior is favorable for the fabrication of devices, since extremely long deposition times will be necessary for mesoscopically thick layers and a particularly high yield is a basic requirement.

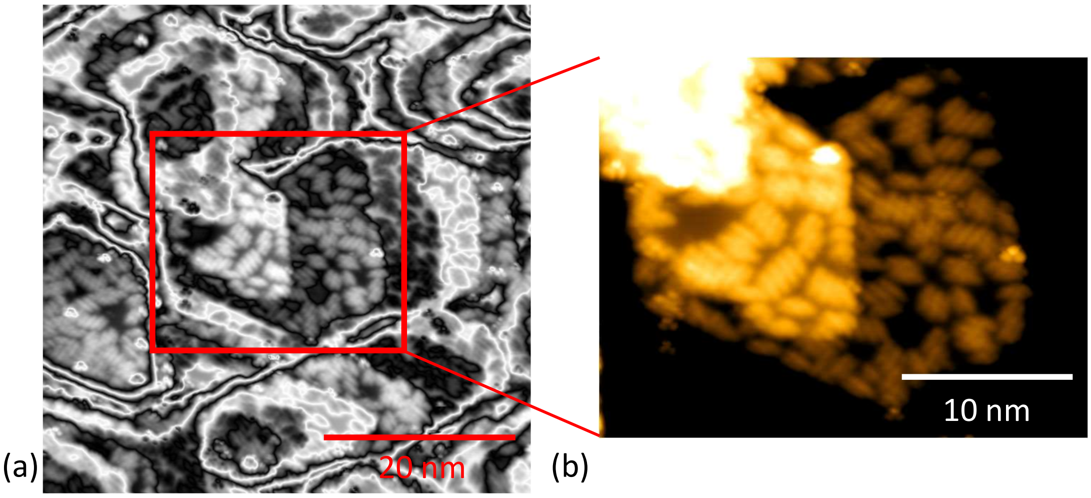

Figure 5.9: (a) STM image with the same contrast as Fig. 5.8(a) of BNTCDI/Co(0001)/Au(111) after 26 min of deposition. The long deposition time increases the yield of intact molecules significantly on all layers ($50 \times 50\,\mathrm{nm}^2$, $V_{\mathrm{bias}} = 1.0\,\mathrm{V}$, $I_{\mathrm{t}} = 10.0\,\mathrm{nA}$, $T = 77\,\mathrm{K}$). (b) Zoom on two cobalt terraces shows almost exclusively intact molecules arranged parallel to each other in packs evenly distributed over the entire surface.

In conclusion, a deposition temperature between $T = 260 - 275°\,\mathrm{C}$ (at $I = 0.26\,\mathrm{A}$) with the sample at room temperature and long evaporation times (several minutes up to hours) provide relatively reproducible results when it comes to monolayer coverage of intact BNTCDI molecules on Co(0001). Similar to the variations with regard to the adsorption rate it is concluded that the varying yield of intact molecules may arise mainly from different batches of the molecule flakes as well and for each batch and also with progressive consumption within a batch the parameters are subject to strong variations. This may explain some varying parameters in the scope of this thesis. Again, the suitable temperature window seems to be quite narrow while the temperature has a minor influence if any on the yield of intact molecules. As a premise, it can be seen that the temperature window determined above was always attempted to be met. As mentioned before an increase in pressure in the molecule chamber was used as an indicator for an incipient sublimation. This is the reason for the partly differing temperature data. Finally, it was tried to change only the deposition time and to keep the temperature during evaporation as constant as possible.

In all probability, the purity of the molecules in powder form, i.e. as I received them from the chemists, also plays a decisive role. However, the extent to which the purity fluctuated or the molecules were possibly even contaminated or destroyed during *ex-situ* treatment is speculative and could only be determined in the future by very time-consuming investigations. Overall, the greatest danger in the choice of evaporation temperature appears to be the aforementioned incrustation of the crucible, not the destruction of evaporable molecules. Thus, care should be taken to ensure a very slow crucible ramp-up speed.

5.2.2 Adsorption Geometry

Within the limits outlined above and considering the problems discussed with regard to the different batches, with increasing experience and "feeling" for the current batch of molecules it has been possible to realize a mostly reproducible deposition of BNTCDI layers close to a monolayer on Co(0001) though. The next goal was to understand the adsorption of the molecules, in order to continue the path from the microscopic unit to the final mesoscopic device and to understand each step as well as possible. For this, the adsorbed BNTCDI will be measured and its adsorption behavior and adsorption position in relation to the underlying Co(0001) will be discussed.

The BNTCDI molecules in the following are sublimed at the previously determined temperatures between 265° C (538 K) and 275° C (548 K) while the substrate is kept at RT. A high-resolution STM image of an isolated BNTCDI molecule on Co(0001) is shown in Fig. 5.10(a). The apparent shape has C_{2v} symmetry very similar to the case of BNTCDI adsorption on Pt(111) reported by Ebeling et al. [102]. In both cases the molecular appearance can be explained by the adsorption of the molecular backbone (naphthalene-diimide part) in a flat manner with the phenyl groups on both sides standing upright and perpendicular to the substrate plane.

Figure 5.10(b) shows a linescan over the BNTCDI molecule as indicated by the dashed line in Fig. 5.10(a). The dashed line also marks the nodal plane of the upward pointing phenyl groups, while the features marked with π are attributed to the lobes of the p_z atomic orbitals of the C atoms of the phenyl groups that form the π-orbitals. Figures 5.10(c) and (d) show the structure formula of BNTCDI from the top view and the side view, respectively. The theoretical size of the BNTDCI, i.e. lateral distance from the outermost hydrogen atom to the opposite outermost hydrogen atom, is 1.83 nm. In contrast to Fig. 5.1, the 3D-model of the structure

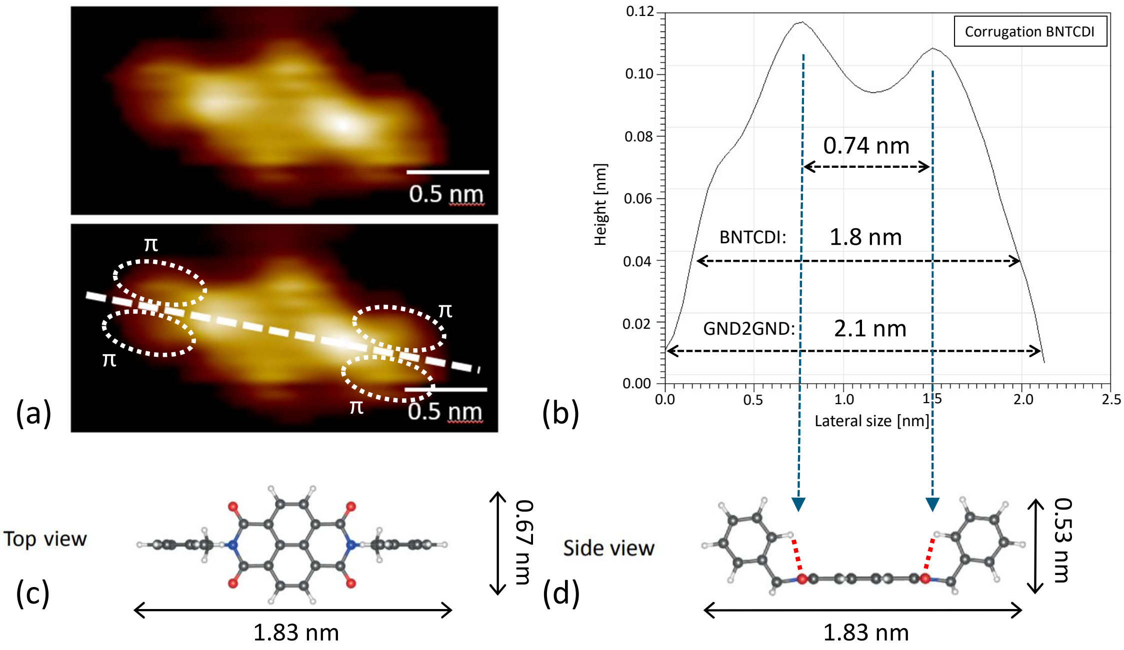

Figure 5.10: BNTCDI adsorbed on Co(0001). (a) STM image of a single BNTCDI molecule deposited on Co(0001)/Au(111) with sub-molecular resolution once with marked linescan position and once without. The C_{2v}-symmetric shape indicates that both phenyl groups stand upright as indicated in the side view in (d) ($2.6 \times 1.6\,\text{nm}^2$, $V_{\text{bias}} = -1.0\,\text{V}$, $I_{\text{t}} = 1.0\,\text{nA}$, $T = 77\,\text{K}$). (b) Corrugation along the dashed line in a). The blue arrows correlate the peaks with their lateral position with respect to the molecule. (c) and (d) Size matched structure formula of BNTCDI (grey: carbon, red: oxygen, blue: nitrogen, white: hydrogen) in top and side view, resp. The red dotted lines mark the N-H bond which correlates to the position of the two peaks in the linescan. Made with VESTA [105].

formula shows the geometry of the BNTCDI molecule as it is assumed to adsorb on Co(0001), i.e. with the phenyl groups standing upwards, resulting in the already mentioned mirror-symmetric (C_{2v}) appearance.

The apparent lateral size of the single adsorbed BNTCDI molecule is 2.1 nm from ground to ground. The actual molecule size of 1.83 nm is marked in the plot (see dimensions in the structure formulas). The two peaks in the middle of the linescan which are separated by a valley are striking and correspond to the two bright spots in the STM. The distance between the peaks measured in our STM investigations lies between 0.72-0.74 nm (0.74 nm in Fig. 5.10(b)) and the depth of the valley is 15-21 pm. Note that both the top view and the side view of the structural formula are size-matched with both the STM image and the linescan. The scale is consistent with the corrugation and with the STM as well, so that the structure formulas can be compared to the data. At first glance, the two peaks could be mistaken for the two upright standing phenyl groups, and thus our model could be considered proven. Yet, the lateral distance between the peaks does not correspond to the distance of the phenyl groups' centers. The blue arrows indicate the position of the peaks in the structure formula in Fig. 5.10(d) and are located laterally between the nitrogen atoms of the naphthoic diimide backbone and the innermost hydrogen atom of each phenyl group. The distance between the nitrogen atoms within the molecule is 0.71 nm. As the phenyl groups are considered to be slightly rotated around the upwards pointing C-C axis and somewhat tilted, the distance of the hydrogen atoms can not be derived from the side view directly. Therefore, I associate the peaks with the region between the nitrogen atom and the innermost hydrogen atom of the corresponding phenyl group indicated by the red dotted lines (hereafter also referred to as N-H bond). The red dotted lines indicate the intramolecular nitrogen-hydrogen bonds which determine both the upright configuration of the phenyl groups and the orientation of the methylene groups with their hydrogen atoms pointing towards the substrate leading essentially to a decoupling of the phenyl groups from the metal. In that manner the overall configuration of the single molecule is determined very similar to the findings of Ebeling et al. [102]. The position of the two peaks in the measured data correspond to the position of said N-H bonds. During our investigations, it turned out, that the position of the two peaks did not depend on the gap voltage, neither in amount nor in sign. Therefore the two peaks can not be explained e.g. by the LUMO (cf. Ebeling et al. [102]) in gas phase despite its resemblance but are present due to the interaction between the molecule and the substrate. As the position is not voltage dependent and strictly correlated to the interplay between the N-H bonds and the underlying substrate atoms, the two peaks can serve as a marker or intramolecular scale.

Now that we have a picture of the adsorption geometry of each individual molecule, one wants to know how the molecule attaches to the underlying cobalt atomic lattice, i.e. the adsorption sites. To this end, I first investigated how several molecules behave with respect to each other and how they arrange at high coverage (close to a ML) in order to draw conclusions about the position and orientation of the underlying cobalt lattice.

As mentioned in Sect. 5.1, the packing and stacking of similar aromatic molecules in crystals [101, 106] and on noble metals [98, 107] depends on subtle details and is subject of intense research. Here, I found that BNTCDI forms a monolayer on Co(0001), before stacking of the molecules occurs. As shown in Fig. 5.11, the

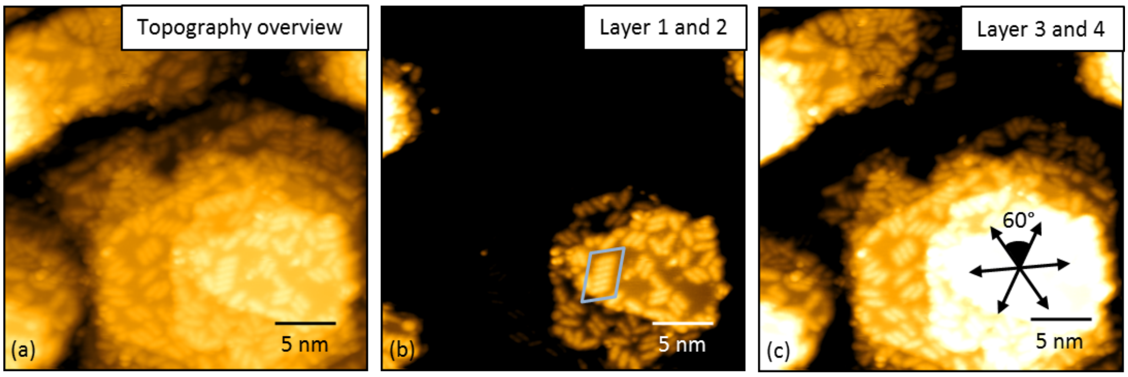

Figure 5.11: STM image of a sub-ML coverage of BNTCDI molecules on Co(0001)/Au(111). (a) The molecules fill up the empty space until the mesa tops and terraces are fully covered, see for instance the very dense molecule packing at the upper image border of (c). There is no indication for molecule stacking before the surface is fully covered. This behavior is the same on all terraces as can be seen when the data of (a) is re-displayed with adapted color scales in order to emphasize the first and second (b) or the third and fourth (c) layer from the top. The grey box in (b) marks five molecules in parallel alignment. The arrows in (c) indicate the three predominant in-plane adsorption orientations of the molecules ($30 \times 30\,\mathrm{nm}^2$, $V_{\mathrm{bias}} = 1.0\,\mathrm{V}$, $I_{\mathrm{t}} = 1.0\,\mathrm{nA}$, $T = 77\,\mathrm{K}$).

molecules adsorb regularly over all terraces until the whole surface is covered. As described in Sect. 5.2.1, we observe mainly intact molecules that are predominantly aligned along three different axes with intermediate angles of 60°. This fits to the three-fold symmetry of the underlying Co(0001) lattice and gives us a first indication of how the molecules orient on the cobalt lattice. Furthermore, the molecules seem to order in arrays with parallel alignment to each other (see grey box in Fig. 5.11(b)), similar to Ref. [100]. Weak intermolecular interactions between oxygen and hydrogen atoms are considered to be the driving force of this alignment [108].

The gray box in Fig. 5.11(b) marks an arrangement of five intact BNTCDI molecules aligned in parallel but shifted along their long axis with respect to each other.The very same array is shown in Fig. 5.12(a) for further investigation.

The Co(0001) mesa shown in Fig. 5.12(a) is covered with several intact BNTCDI molecules. The color scale has been changed with respect to Fig. 5.11 and some post-processing in terms of contrast has been done to image as much as possible of both the molecules and the underlying lattice. As becomes immediately apparent, the molecules do not arrange themselves arbitrarily. Essentially, there are three orientations which can be associated with the threefold symmetry of the cobalt lat-

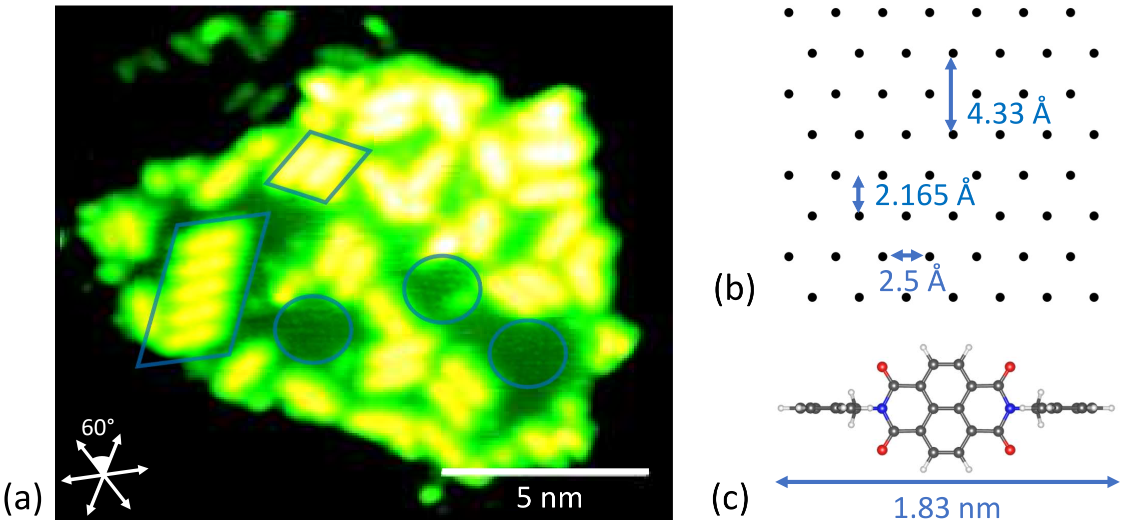

Figure 5.12: (a) The same mesa as highlighted in Fig. 5.11(b). Blue boxes mark arrays with two and five molecules in parallel alignment and the blue circles indicate regions of bare Co(0001). The arrows indicate the three predominant in-plane adsorption orientations of the molecules which are considered to correspond with the three-fold Co(0001) lattice of (b). The goal is to reconcile the structure formula in (c) and the lattice vector in (b) ($15 \times 12.5\,\mathrm{nm}^2$, $V_{\mathrm{bias}} = 1.0\,\mathrm{V}$, $I_{\mathrm{t}} = 1.0\,\mathrm{nA}$, $T = 77\,\mathrm{K}$).

tice. The white arrows at the bottom left of the picture show the three orientations, which are rotated by 120° to each other.

The areas marked with the circles indicate the bare and atomically flat Co lattice between the molecules. For technical reasons it is not possible to show the lattice in the immediate vicinity of the molecules or even below them. As can be seen in the blue diamonds, the molecules are not only arranged parallel to each other, but also with a small, regular offset along their longitudinal axis. This offset is always the same, no matter if there are several (for example five) or only two molecules. It is not easy to determine the exact offset, but it is obvious that the molecules arrange themselves regularly and periodically. These arrays of several (two or more) molecules arranged parallel to each other will be referred to as "packs" in the following. Interestingly enough, packs with more than five parallel molecules are very rare if present at all.

Figures 5.12(b) and (c) depict a scheme of the cobalt lattice with relevant dimensions and the structure formula of the molecule drawn to scale. In the following, the task is to find out how the structure formula from (c) and the lattice from (b) fit together. Since it is impossible to image the lattice directly next to and below the molecules, I seek to relate the intermolecular dimensions between the molecules (i.e. in particular spacing, shift, and orientation) to the Co(0001) lattice. To find out the orientation of the longitudinal axis of the molecules relative to the crystal lattice vectors, the orientations can be compared on the basis of step edges located in the vicinity. Subsequently, the position of the molecules relative to each other is determined as accurately as possible using high-resolution images and compared with the dimensions of the lattice.

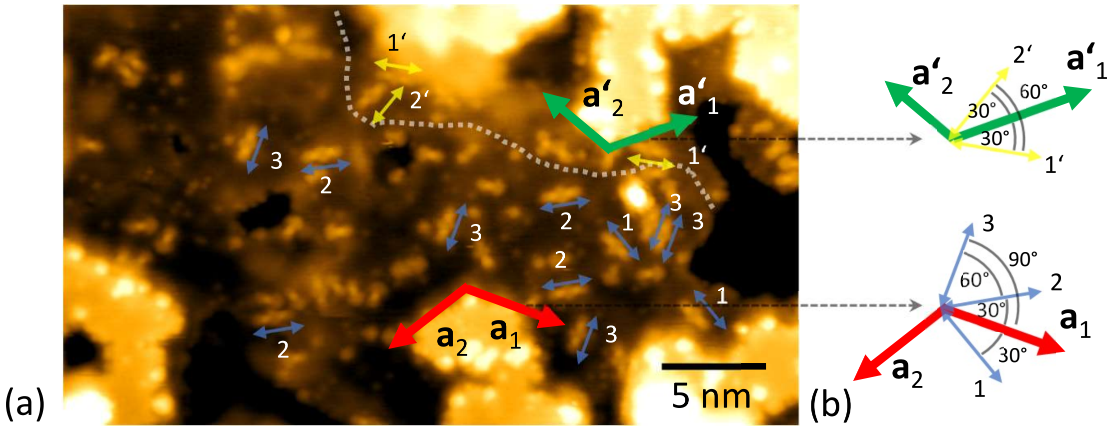

Figure 5.13: Comparison of the orientations of the molecules with the step edges of the Co(0001) surface. (a) STM image of BNTCDI/Co(0001)/Au(111). From the step edges I deduce the lattice vector in (b) ($35 \times 20\,\mathrm{nm}^2$, $V_{\mathrm{bias}} = 700\,\mathrm{mV}$, $I_{\mathrm{t}} = 1.0\,\mathrm{nA}$, $T = 77\,\mathrm{K}$). (b) The lattice vectors and the identified molecule orientations above (green and yellow) and below (red and blue) the dotted line which might correspond to a grain boundary, hence the two sets of lattice vectors.

Figure 5.13(a) shows a STM image of a thin Co(0001) film with large terraces grown on a Au(111) single crystal. The thickness of the Co film is between 1.6 and 2.0 nm ($I_{\mathrm{Fil}} = 1.99\,\mathrm{A}$, $U \approx 830\,\mathrm{V}$, $t_{\mathrm{evap}} = 35\,\mathrm{min}$). Subsequently, a small amount of BNTCDI molecules has been deposited ($I = 0.26\,\mathrm{nm}$, $T = 252°\mathrm{C}$, $t = 2\,\mathrm{min}45\,\mathrm{s}$, $p = 1.3 \times 10^{-10}\,\mathrm{mbar}$). Note that in good agreement with the observations made in Sect. 5.2.1, at a coverage well below a monolayer, relatively many broken molecules can be found on the surface.

The large atomically flat plateau in the center of the image occupies most of the total measured area of $35 \times 20\,\mathrm{nm}^2$. The red and green arrows mark the directions of the step edges adjacent to the large plateau. It is therefore assumed that these arrows can be correlated with the lattice vectors of the Co(0001) lattice $\mathbf{a}_1$, $\mathbf{a}_2$, $\mathbf{a}'_1$, $\mathbf{a}'_2$ (cf. Fig. 5.13(b)). Coming from these lattice vectors, I compare the orientations of the molecules' longitudinal axes in order to draw conclusions about the adsorption geometry with respect to the underlying lattice. Please note, that it turned out that the molecules below the dotted line align in the very same way to the lattice vectors $\mathbf{a}_1$, $\mathbf{a}_2$, as the molecules over the line do with respect to $\mathbf{a}'_1$, $\mathbf{a}'_2$. The origin of this boundary is still an open discussion. The angles $\mathbf{a}_1$ and $\mathbf{a}'_1$' span an angle of about 39° to each other, so that an equivalence cannot be found in the crystal lattice. Instead, a grain boundary is up for discussion, although this has not been answered conclusively. It is nevertheless striking that the molecular orientations are consistently related to the corresponding step edge. Therefore I compare the molecules below the line to the lower step edges and the molecules above the line to the upper step edges. The orientations of the longitudinal axes of all intact molecules are marked with blue arrows below and yelloy arrows above the dotted line.

When comparing the orientations of the molecules to each other, it is noticeable that, as already mentioned above, the molecules are always at an angle of 120° to each other, or 60° degree respectively, depending on the reading. The identifiable orientations of the molecules are labeled with the adjacent numbers (1, 2, 3, or $1'$, $2'$, resp.). The same threefold symmetry applies to the assumed lattice vectors, which, as expected, span an angle of 120° to each other, as well due to the C_3-symmetry of a (0001)-surface. This suggests that the molecules are in a defined relationship with equal symmetry to the underlying lattice vector. However, comparing the molecule orientations with the lattice vectors, above and below the dotted line, shows that the molecules do not arrange parallel to the lattice vectors, but are rotated.

Figure 5.13 (b) shows the angles between the molecules and the lattice vectors as they can be extracted from Figure 5.13 (a). It becomes perfectly apparent that the orientiations 1, 2 and 3 span an angle of said 60° and 120°. The angle between the molecule orientations 1 and 2 with respect to the lattice vector $\mathbf{a}_1$ is 30° though. Thus, the angle between orientation 3 and $\mathbf{a}_1$ is 90°. The same holds mutatis mutandis for orientations $1'$, $2'$ and $\mathbf{a}'_1$. This suggests an adsorption position in that manner that the longitudinal axis of a molecule lies precisely between two crystallographic axes.

To compare this observation with the lattice model, Fig. 5.14(a) shows a hexagonal lattice with marked lattice vectors. The grey diamond marks the primitive cell spanned by the unit vectors $\mathbf{a}_1$ and $\mathbf{a}_2$ (red arrows). If the orientation of the lattice vectors get rotated by 30°, the resulting vectors (blue arrows) point to the group second-nearest lattice sites i.e. the points [1,2,0] and [1,-1,0]. In Fig. 5.14 (b) the lattice vectors $\mathbf{a}_1$, $\mathbf{a}_2$ and $\mathbf{a}_3$ and the rotated vectors $\mathbf{b}_1{:=}2\mathbf{a}_1{+}\mathbf{a}_3$, $\mathbf{b}_2{:=}2\mathbf{a}_2{+}\mathbf{a}_1$ and $\mathbf{b}_3{:=}2\mathbf{a}_3{+}\mathbf{a}_2$ are extracted and the resulting angles are marked to get a better overview and to simplify the comparison with the STM results from Fig. 5.13. The angles between red and blue vectors are 30°, 90° and 150°.

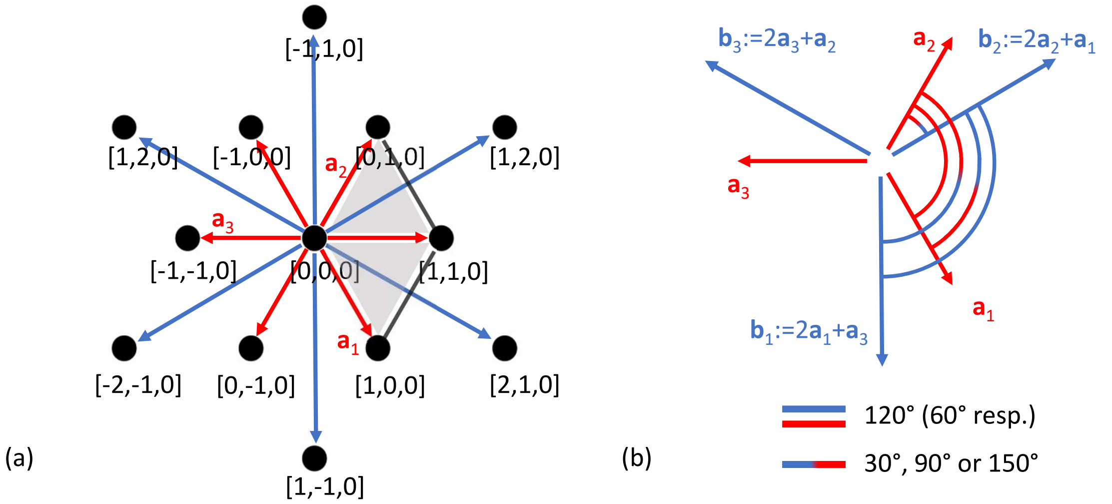

Figure 5.14: (a) Overview of lattice vectors (red) and second neighbor vectors (blue) within a hexagonal lattice. The unit cell is grey. (b) show the possible relations between the vectors of (a). This is for overview purposes only and helps to compare the angles between the presumed orientation of the molecules along the second neighbor vectors with the lattice vectors and thus interpret the measured data. The possible angles that result for the presumed configuration (red/blue) correspond to our observations. Due to the degeneracy, only the angles up to 180° are drawn.

It becomes perfectly apparent, that the angles between the lattice vectors (red arrows), the angles between the molecule orientations (blue arrows) and the angles between the lattice vectors and the orientations fit perfectly with this model. From that I conclude that the molecules orient along the vectors $\mathbf{b}_n, n = 1, 2, 3$.

Now that we have the orientation of the molecules in relation to the underlying lattice vector, the question is how they adsorb with respect to the underlying atoms. Clues to this are provided by the dimensions of two neighboring and parallel molecules, i.e. how they are positioned to each other. Since the molecules arrange themselves in regular and symmetrical packs, it seems obvious that the arrangement to each other can also be related to the lattice.

To this extend, Fig. 5.15(a) shows an STM image of a thin Co(0001) film grown on a sputtered Au(111)-single crystal with several BNTCDI molecules adsorbed on the surface. Besides several molecule fragments and intact single molecules, there

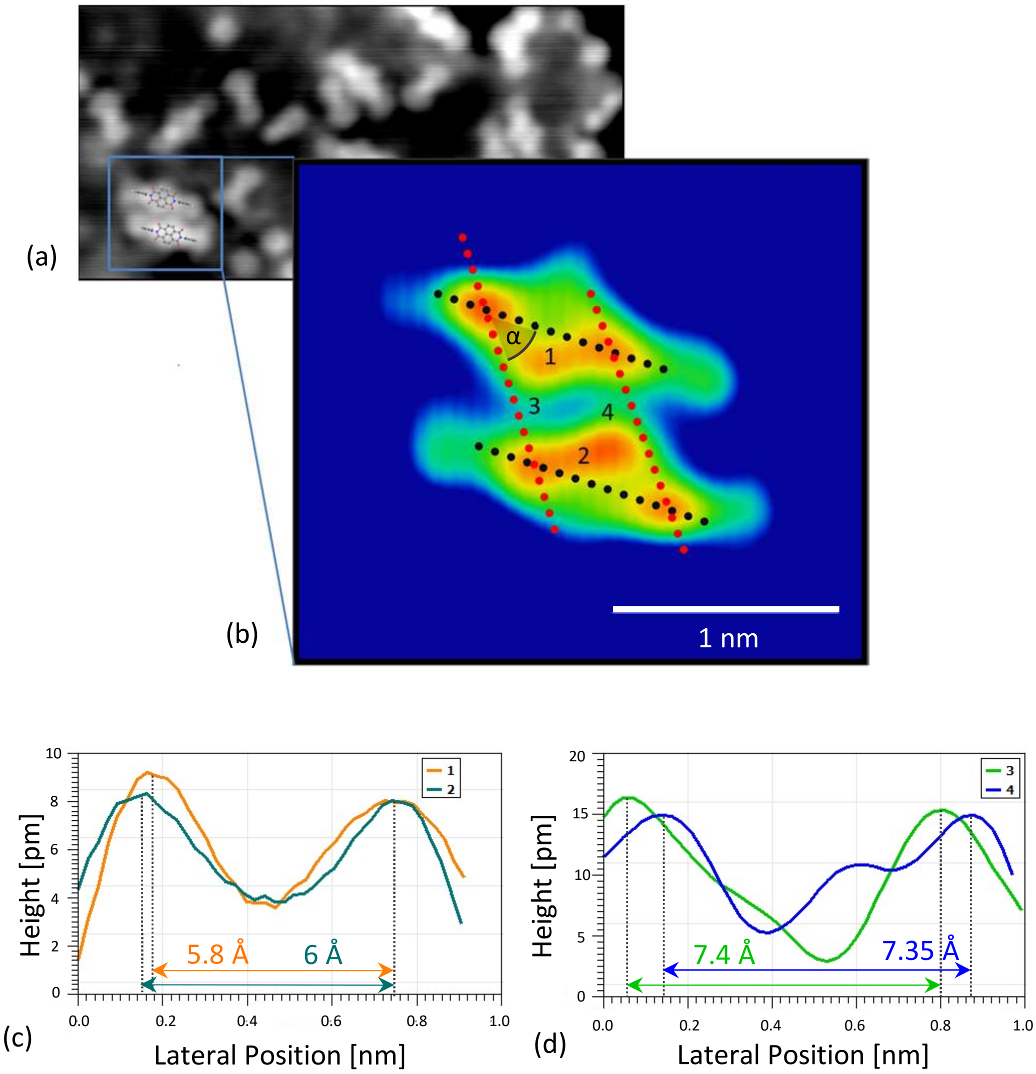

Figure 5.15: (a) High resolution STM image of several packs of two BNTCDI molecules with pronounced intra molecular features and clear boundary in between ($12 \times 6\,\mathrm{nm}^2$, $V_{\mathrm{bias}} = 250\,\mathrm{mV}$, $I_{\mathrm{t}} = 7.0\,\mathrm{nA}$, $T = 4.4\,\mathrm{K}$). (b) Zoom on the marked area in (a) with ultra hard contrast to clearly distinguish the intra molecular features particularly the peaks over the N-H bonds. The position of the linescans are marked and labeled in order to determine the distance between the molecules. The angle α is exactly 60° which further validates the assumed alignment along the lattice. (c) Linescans along the axis of each molecule. The distance between the peaks is considerably too short which is due to a calibration error (see text). (d) Linescans between the N-H bonds of two different molecules. The distances between the peaks has to be corrected by the factor derived from (c).

can be found some packs of two parallel molecules (hereinafter referred to simply as packs). The blue box marks a region with a pack at very good resolution where intra-molecular features can be identified as well as a sharp border between these molecules. Thus in this pack, the two individual molecules can be perfectly distinguished from each other as well as the inner structure of each individual molecule itself. This enables a deep insight in the adsorption geometry and the alignment of BNTCDI on Co(0001).

Figure 5.15 (b) shows a zoom onto the area marked with the blue box in (a). The color scale has been adjusted and an ultra hard contrast has been applied to emphasize the intra-molecular structure and to distinguish between the individual molecules as precise as possible. As mentioned before it is not trivial to measure the distance between two molecules for the lack of defined start and endpoints and angles (i.e. an internal scale). The best reference point that is well defined within each molecule is the peak in the region of the N-H-bond between the phenyl-groups and the backbone of the molecule as discussed in the context of Fig. 5.10. From the relation of these peaks, i.e. four of them in the case of two molecules, I infer the arrangement of the molecules with respect to each other.

The linescan positions are depicted in Fig. 5.15 (b) by the dotted lines and are numbered with 1-4. The black dotted lines 1 and 2 run along the longitudinal molecular axis of each individual molecule further emphasizing that both molecules align perfectly parallel to each other. The red dotted lines 3 and 4 connect the corresponding peaks of the molecules and are therefore parallel to each other as well. Consequently, the red and black dotted lines meet in the center of the peaks and therefore define the position of the molecules with respect to each other properly. Before I analyze the distances, the angle α between 1 and 3 or 2 and 4, respectively, is 60°. Since the angle α also describes the shift between the otherwise parallel molecules, it is very likely that the offset of the molecules to each other corresponds to the underlying lattice (cf. lattice angles Co(0001) as discussed above). As the molecule axis is considered to run along the vectors $\mathbf{b}_n, n = 1, 2, 3$ it is therefore assumed, that the shift or offset runs along the same vectors as well and furthermore exactly by the amount $|\mathbf{b}_n|, n = 1, 2, 3$.

The resulting data from the linescans is shown in Fig. 5.15 (c) and (d) and marked with the corresponding numbers 1-4. The measured distance between the peaks along the molecule axis are 1: 5.8 Å and 2: 6.0 Å. The measured distances between the corresponding peaks of the neighboring molecules are 3: 7.4 Å and 4: 7.35 Å. Based on these values, some problems arise. If one tries to bring the molecules as close together as the measured values for 3 and 4 suggest, then the molecules come so close to each other that they overlap, which is energetically unfavorable. Furthermore even from beholding the microscopy images, that makes basically no sense. So there must be an error within the measured values. After struggling for quite some time with the determination of the error and discussing numerous models, I finally came to the conclusion that the STM machine must have had a calibration error. It turned out that there was indeed an error after a software update. Note that the other measurements are not affected by this error as the update has been performed shortly before the corresponding measurements have been carried out.

Fortunately in Fig. 5.15 (a) and (b) there is a fix reference to determine the error and to correct the data properly. As discussed above concerning Fig. 5.10, the two peaks correspond to the region above the N-H-bonds. A model of a molecule on Co(0001) was recreated using the VESTA software [105] and the distance between the two nitrogen atoms was determined by the software to be 7.1 Å in this model. The measured distance between the peaks is between 7.2-7.4 Å, so slightly shifted toward the outside of the molecule with respect to the nitrogen atom. Therefore it seems justified to assume 7.3 Å as a fixed value or scale within the measurements of Fig. 5.15. I use that value as the basis for the distance between the peaks and derive the calibration error (hence the correction factor) for the measured distances accordingly. The calibration error of about 21.7% or a correction factor of 1.217 respectively, based on the measured value for linescan 2. Table 5.1 shows the corrected values of the distances.

Linescan	**Measured** [Å]	**Corrected** [Å]	**Characteristic**
1	5.80	7.06	intra molecule
2	6.00	7.30	intra molecule
3	7.40	9.01	inter molecule
4	7.35	8.94	inter molecule

Table 5.1: The intra- and intermolecular peak-to-peak distances as measured in Fig. 5.15 and corrected by the calibration error of 21.7%.

Based on these corrected values, an attempt was made to arrange the molecules on the cobalt lattice. Of course, with such small image sections, the measurement inaccuracy must be taken into account (cf. the distances of 1 with 2 and 3 with 4) and a model was sought in which these distances are reasonably related to the lattice below. Consequently, there is some leeway in the values and what seems reasonable from an energetic point of view has to be taken into account, for example symmetry, equal adsorption sites of both molecules, alignment along the lattice vectors and periodicity.

Figure 5.16 shows our proposed model for the adsorption geometry of BNTCDI on

Co(0001) in terms of alignment along the lattice vectors and the relative position to each other. Note that the positioning of the molecule atoms with respect to the underlying Co atoms, i.e. if an atom is on top of or between two underlying atoms (top site, hollow site, bridge etc.), is not uniquely determined by the measured angles and distances, but has been chosen to be symmetric between the left and the right half of each molecule on the basis of the mirror-symmetric STM images. The two molecules have been placed on the underlying scale-adjusted lattice (black dots). The distances are taken from N-H bond to N-H bond with said 7.3 Å within a single molecule. The distance between two corresponding nitrogen atoms of two molecules is derived from this model to be 8.6 Å. The angle $\alpha = 60°$ fits perfectly to the observation in our measurements. The intermolecular peak-to-peak distance in this model is 8.6 Å and thus the corrected measured values are 3.9% and 4.7% too large which is considered to be within the measurement accuracy. This holds in particular if one compares the corrected values of 1 with 2 and 3 with 4 which yields an uncertainty of 3.3% and 1%, respectively, within the same measurement. Thus I conclude that while the molecules align along the vectors $\mathbf{b}_n, n = 1, 2, 3$ ($\mathbf{b}_2$ in Fig. 5.16) as already discussed, they are placed with respect to each other along the same vectors ($\mathbf{b}_1$ in Fig. 5.16) and furthermore with a distance of exactly the amount $2 \cdot |\mathbf{b}_n|, n = 1, 2, 3$. To be perfectly clear, in the model shown in Fig. 5.16 the lattice vectors $\mathbf{b}_1$ and $\mathbf{b}_2$ have been marked. In this example the molecules align along $\mathbf{b}_2$. Starting from molecule 1, molecule 2 is displaced in the direction of the vector $\mathbf{b}_1$ by the exact amount of $2 \cdot |\mathbf{b}_1|$. The resulting shift is in the direction $-\mathbf{b}_2$ by the amount of $1 \cdot |\mathbf{b}_2|$.

Now that I consider the relative position of the molecules to each other and the alignment with respect to the lattice vectors to be understood, it is still up for discussion how the molecules are positioned with respect to the underlying atoms. The model shown in Fig. 5.16 depicts the molecules as adsorbed symmetrically, e.g. the adsorption sites of the left half of each molecule (cf. mirror axis) is the same as the corresponding adsorption sites ot the right half. This assumption was based on the completely symmetrical appearance of the molecules in the STM images. Whether this is the case or the adsorption is in contrast asymmetric is still an open question though. The necessary information can not be extracted from the STM measurements solely, as one has no access to the underlying atoms directly. As the length of BNTCDI is not an integer multiple of $\mathbf{b}_n, n = 1, 2, 3$, if the N-H bond is on top of a Co atom, the other N-H bond is on a hollow site and vice versa. In order to draw conclusion about the adsorption site, I performed spectroscopy and compared the density of states and conductance of each side of the mirror axis of BNTCDI.

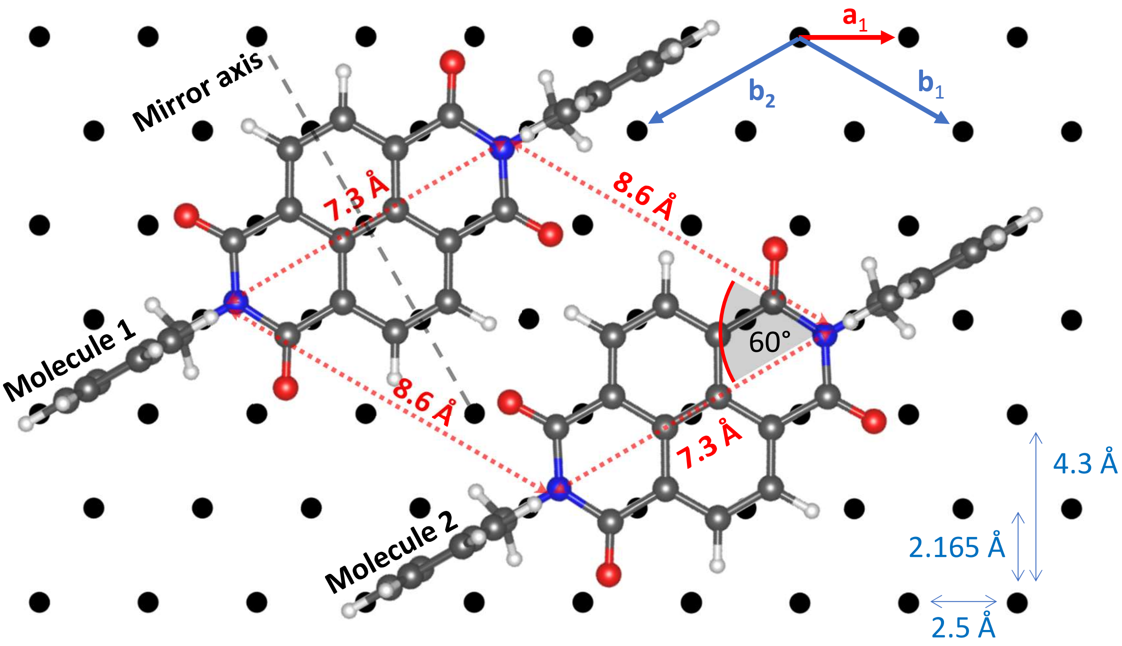

Figure 5.16: Suggested model of a pack of two BNTCDI molecules on Co(0001). The molecule align along $\mathbf{b}_2$ and they are displaced by $2\cdot\mathbf{b}_2$ with respect to each other. In the picture, the left and right half of each molecule occupies the same adsorption site wherein the oxygen atoms (red) are equivalently far away from the Co atoms. The same holds for the nitrogen atoms (blue).

From the comparison I aim to conclude on the adsorption position. To this extend in the next section the corresponding STS data and $\frac{\mathrm{dI}}{\mathrm{dU}}$ maps are presented and from that a model for BNTCDI adsorbed on Co(0001) will be derived.

5.3 BNTCDI on Co(0001) - Spectroscopy

To further understand the molecule/metal interaction between BNTCDI and Co(0001) and to obtain further insights on both the adsorption position and the electronic structure, spectroscopy measurements on BNTCDI molecules adsorbed on Co(0001) were performed in the course of this work.

Firstly, spectroscopy (STS) curves have been taken at different points on a single BNTCDI molecule adsorbed on Co(0001) to compare the symmetry within a single molecule. Subsequently, spectra have been taken at the same corresponding points at different packs of BNTCDI molecules. Therefore the very same sample as in

Fig. 5.15 has been investigated with three different packs. Corresponding spectra have been taken with high resolution over a long time period with several repeats to minimize the spread. Conductance maps of this sample were then created based on the energies determined from the spectra.

5.3.1 Electronic Structure STS

Figure 5.17 shows a 10×10 nm^2 STM image of a Co(0001) surface with a single adsorbed BNTCDI molecule in the middle of the section. Please note that the color scale of the image has been chosen to emphasize the position of the molecule solely. Simply put, it has been found in practice that a good "STM tip" is not necessarily a good "STS tip" and vice versa. In this case, the STM image only serves to determine the positions at which the spectra were recorded. The two regions above the N-H bonds and the flatly adsorbed backbone of the BNTCDI molecule were examined. In particular, the comparison of the spectra above the two N-H bonds of a molecule will be compared to investigate whether the local density of states (LDOS) above both bonds of the perfectly symmetric molecule are identical. If the spectra of these symmetric positions are basically not the same, this may be due to the atomic configuration of the adsorption sites below these positions. This would be a valid indication that the molecules do not adsorb symmetrically, but occupy asymmetric adsorption sites, so that the LDOS is affected differently.

The green, yellow and blue dots mark the positions of the corresponding spectra which are shown in Fig. 5.15 (b) in according colors. The arrows below the STM image point at the position where the spectra are taken within the molecule. The green and blue spectra are supposed to correspond with the area of the N-H-bonds while the yellow spectrum has been taken over the flatly adsorbed backbone of the molecule. The red spectrum represents a measurement on bare Co(0001) grown on Au(111) of the very same sample and serves as a reference.

The spectrum has been taken on < 2 nm Co(0001)/Au(111) at 4.4 K. The probed energy range $E - E_{\mathrm{F}}$ is [-1 eV; 1 eV]. The spectrum is averaged over 10 repetitions (reps.) at an oscillation amplitude of the modulation of $U_{\mathrm{mod}} = 32$ mV. The STM was operated at the setpoint of $U_{\mathrm{sp}} = -0.2$ V and $I_{\mathrm{sp}} = 1$ nA.

The sharp peak at $U_{\mathrm{bias}} = -0.38$ V correlates with an $3d$ cobalt surface state which extents into the vacuum. The exact position of corresponding surface states depends

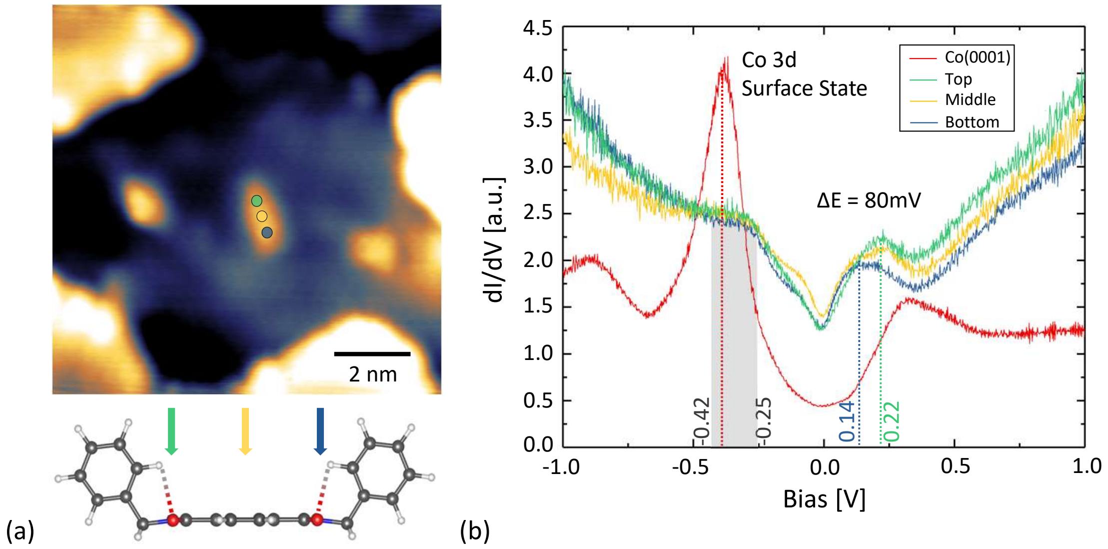

Figure 5.17: (a) STM image of a single BNTCDI on Co(0001). The positions of the spectra shown in (b) are indicated by spots of the corresponding color. ($10 \times 10\,\mathrm{nm}^2$, $V_{\mathrm{bias}} = -1.0\,\mathrm{V}$, $I_{\mathrm{t}} = 1.0\,\mathrm{nA}$, $T = 4.4\,\mathrm{K}$). (b) Spectra taken at the two bright spots over the N-H bonds (according to their position in the STM image "Top" and "Bottom") and in the middle of the backbone ("Middle"). For comparison a pectrum taken on bare Co(0001) is shown for reference (not matched on the ordinate). The sharp peak at -0.38 V corresponds to a Co 3d surface state. The marked energies correspond to the features as indicated by the dotted line and the grey energy interval, respectively.

on several factors as contamination, film thickness (layers of islands), tip distance and the crystallographic orientation of the surface and has been studied before. These corresponding surface states with d symmetry have been located inter alia at -0.43 eV [109], -0.31 eV [110] and -0.3 eV [111]. Thus I identify this peak with a Co surface state with d symmetry as well. Note that the spectrum was taken in the very same sample state, i.e. that molecules have already been sublimated in the preparation chamber and thus the surface is most probably somewhat contaminated.

The yellow, green and blue spectra are the spectra taken on the molecule at positions marked in Fig. 5.15(a). The features and in particular said 3d surface state of Co can not be clearly identified or are absent in the molecular spectra. There are shoulders in the range of [-420 mV; -250 mV] (grey area in Fig. 5.15(b)) though. This shoulders are considered to correspond to the Co surface state which is in the same energy range. This may indicate that the features of the metal spectrum are shifted and/or suppressed by the adsorbed molecule. On the other hand, no sharp and discrete molecular states can be observed either. From this I conclude that BNTCDI chemisorbs on Co(0001) and the orbitals hybridize forming hybrid orbitals. This is crucial pillar for the envisioned utilization of interface effects as hybrid molecular magnetism in aspired devices (cf. Sect. 3.3).

In the $U_{\text{bias}} \geq 0\,\text{V}$ range, the molecular spectra show a feature at $U_{\text{bias}} = 140\,\text{mV}$ (blue spectrum) and $U_{\text{bias}} = 220\,\text{mV}$ (green spectrum), respectively, while the yellow spectrum comprises features at both energies. This feature is shifted by 80 mV in the blue spectrum with respect to the green spectrum or in case they are two different features, the two spectra are $\Delta E = 80\,\text{mV}$ apart. Since the molecule is completely symmetrical, this shift or difference is considered to arise from a different underground or, better, from different adsorption sites of the upper and lower N-H bond positions. This could be a first indication for an asymmetric adsorption position as discussed in the previous chapter. Inspired by this observation, I aimed to compare the spectra also of molecules in packs and to draw conclusions about the adsorption position.

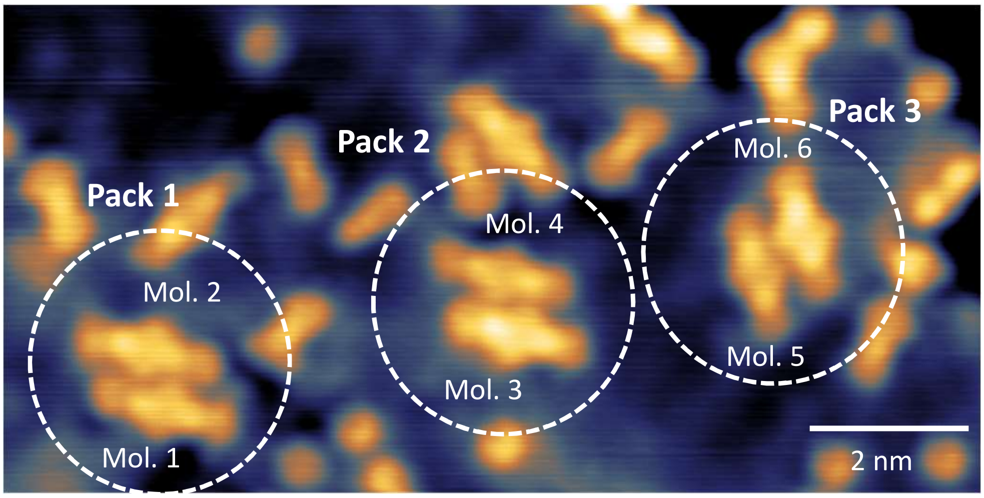

Figure 5.18: High resolution STM image of three packs of two BNTCDI on Co(0001). The three packs consist of two molecules each (labeled), and the relevant intramolecular features are perfectly visible in each molecule. ($12 \times 6\,\text{nm}^2$, $V_{\text{bias}} = 250\,\text{mV}$, $I_{\text{t}} = 7.0\,\text{nA}$, $T = 4.4\,\text{K}$)

Figure 5.18 shows a $12 \times 6\,\text{nm}^2$ section of the very same sample as Fig. 5.15. In fact, the molecule pair 1 is the exact pair as shown in Fig. 5.15(b). Note that in all packs the intramolecular resolution has been achieved very well and at the same time the area or the border between two parallel molecules can be identified very distinctly and sharply. During the many and extensive measurements at this position during the measurement campaign, the STM tip remained stable and the images were consistently reproducible for hours, despite the fact that both numerous STM and spectroscopy measurements were performed at this very position. Both topographic and spectroscopic results were very stable and had good resolution. Consequently, this position with the according set of data is ideally suited for the study of the correlation between the spectra and the morphology of BNTCDI on Co(0001).

Spectra were taken on all six molecules of the three packs at the same positions as in Fig. 5.17. Special attention was paid to the energy range where the 3*d*-Co peak used to be or rather where the shoulders appear on the peak positions (i.e. [-420 mV; -250 mV]) in order to compare the results of each peak position of one molecule and draw conclusions about the adsorption behavior of the molecules. All spectra are averaged over six scan cycles and taken with a modulation of $U_{\mathrm{mod}} = 16\,\mathrm{mV}$ at the setpoint of $U_{\mathrm{sp}} = -0.1\,\mathrm{V}$ and $I_{\mathrm{sp}} = 1\,\mathrm{nA}$.

Figure 5.19 shows the spectra taken on the discussed positions on the six molecules of the three packs of Fig. 5.18. The numbering and naming of the packs and molecules follow the order according to Fig. 5.18. In (a), the first pack (Pack 1) is highlighted in the STM image and the labelling of the spectra is listed. The corresponding spectra are shown in (b) and (c). Each plot shows the three spectra taken at the three positions of each molecule. (b) shows the three spectra of the lower molecule (Mol. 1), here the red spectrum (M1r) has been taken on the right bright spot or peak in the area over the right N-H bond. The blue spectrum was recorded accordingly on the left N-H bond. The yellow spectrum was recorded between the two bright spots, i.e. in the region of the flat adsorbed backbone of the BNTDCI molecule. (c) shows the equivalent spectra for the upper molecule (Mol. 2). The energy range previously associated with the Co 3*d* surface state or the shoulders of the assumed hybrid states [-420 mV; -250 mV] are marked in all plots and serve as a guide to the eye. (d)-(i) show the same data mutatis mutandis for the other packs (Pack 2 & 3) with the other four molecules (Mol. 3-6).

The spectra of all molecules show basically similar behavior, so in the following I will focus in particular on the spectra of the first pack, i.e. (a) and (b). There are outliers like in particular the spectra in (i), where the following considerations apply only to a limited extent. In particular, since the spectra M6b, M6t and M6m have a very similar shape and the features can only be guessed. However, this measurement is considered an exception, which is related in particular to the fact that the tip in the STS measurements must be positioned extremely precisely in order to measure exactly the area of the bright spots. Slight deviations in the positioning lead to considerable distortions of the measurement, which explains the very similar spectra in (i), since it is assumed, that the bright spots were not met exactly.

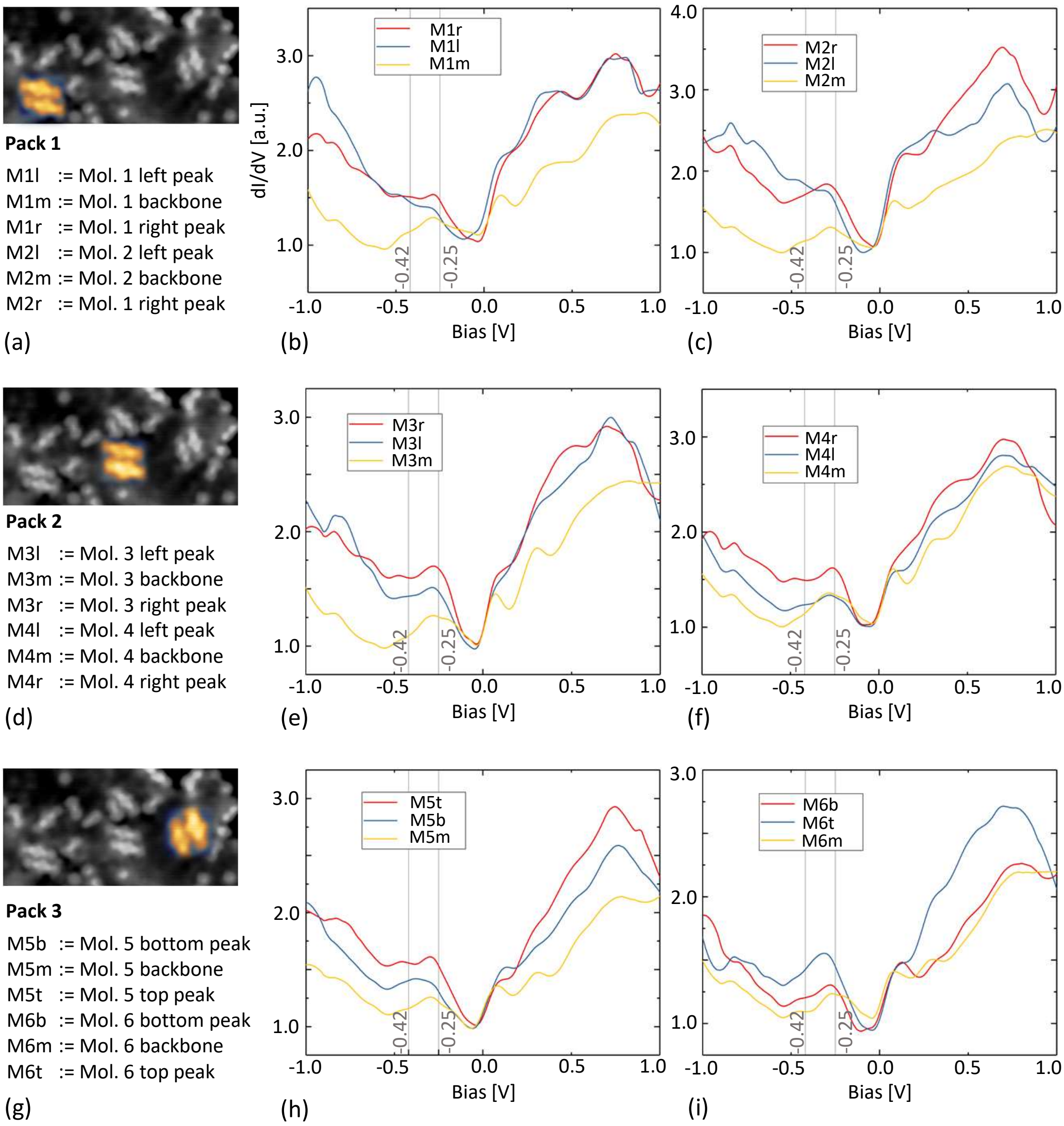

Figure 5.19: Overview of the spectra taken on Mol.1-6 of Pack 1-3. The position of each spectrum is labeld below the STM image of each pack (a, d, g). Each plot shows three spectra on one molecule (b, c, e, f, h, i). The naming of the molecules follows the pattern of Fig. 5.18, while the indications (left, right, top, bottom) correspond to the relative position in the STM. The particular pack being examined in the each row is highlighted in the STM image for easy reference. (STS performed at $U_{\mathrm{mod}} = 16\,\mathrm{mV}$, $U_{\mathrm{sp}} = -0.1\,\mathrm{V}$, $I_{\mathrm{sp}} = 1\,\mathrm{nA}$).

In the energy range of the $3d$ cobalt surface state we see two features in the spectra of the bright spots (blue and red). These features are essentially not present on the backbone (yellow spectrum) or can only be guessed at. In this energy range the spectra of the two bright spots do not have the same course. In (b) and (c) the two spectra of the bright spots (red and blue) even run asymmetrically diametrically or anticyclically to each other. That is, the feature at about $U_{\text{Bias}} = -250\,\text{mV}$ is more pronounced for both molecules in the red spectra, whereas the ratio is reversed at higher energies in the range of $U_{\text{Bias}} = -420\,\text{mV}$. Here the blue spectrum is more intense than the red spectrum at both molecules, so that an inversion occurs (in the case of (b) the inversion occurs at an energy slightly higher than -0.42 V though). Although it is in general very difficult to compare STS measurements quantitatively, we see that the spectra of the two bright spots are not qualitatively the same. In addition, all measurements were performed carefully and directly one after the other at a low temperature (4.4 K) without any disturbances. There were no measurable tip changes, so I assume that the tip did not change over hours. Therefore, I consider the measurements to be quantitatively informative as well. In the spectra of packs 2 and 3 the same features in the same energy range can be identified in the form of peaks or shoulders. Here we do not see the inversion as in (b) and (c) but also a very different curve than the spectra of the backbone (yellow). Furthermore the spectra of the two bright spots also have quantitatively a different curve concerning the intensity. On one bright spot the intensity is always higher than on the other spot in the energy range of interest. They are not identical between [-420 mV; -250 mV]. On the other hand they perfectly overlap over large regions of the remaining energy scale, in particular above and below the Fermi energy at $U_{\text{Bias}} = 0\,\text{mV}$, which is another indication that the spectra can also be compared quantitatively. As the molecules are perfectly symmetrical I correlate the different electronic structure to the not (mirror) symmetrical adsorption sites of the left and right half of the molecule and in particular to the adsorption site of the N-H bonds. This finding can be considered as a quintessence of the spectroscopy measurements in this chapter. If the two features indeed correlate with the Co $3d$ surface state, then the two features may be spin-split and the different sites within each molecule could be exploited in future applications.

From the overall shape of the spectra I conclude that BNTCDI chemisorbes on Co(0001) and forms hybrid states with the metal. From the non-identical spectra on the two bright spots on each molecule in particular in the range of said two features I conclude that the adsorption sites are not identical, indicating an asymmetric adsorption geometry of BNTCDI on Co(0001). As mentioned above, it is necessary to place the tip very precisely above the positions in question. I assume that this was successful essentially well with the measurements in Fig. 5.19. To investigate this further and in particular to get a laterally resolved view of the distribution of states at the energies in question, $\frac{dI}{dV}$-maps are an extremely useful tool as this technique makes precise positioning of the tip obsolete.

5.3.2 dI/dV-Maps

To verify the above considerations regarding the asymmetry of the states, $\frac{dI}{dV}$-maps were recorded at the energies in question. More precisely, at -420 mV and -250 mV (occupied states) and at the energies 140 mV and 220 mV (unoccupied states) determined in Fig. 5.17(b). Fortunately, for reasons of comparability and consistency of the spectroscopic data, I managed to record these maps on exactly the same spot of the same sample with the same tip as used for the measurement of the adsorption geometry and for the spectroscopy above. The duration to take one map was approx. 1.5 h, which made it all the more surprising that there were no disturbances and the tip remained stable for hours.

Figure 5.20 shows the resulting maps for the designated energies. The images on the left ((a), (c), (e), (g)) show the maps in gray scale, with the STM images of packs 1-3 superimposed at the corresponding positions for easy reference. These images just serve as a guide to the eye for the actual maps on the right side ((b), (d), (f), (h)) with the typical color scale. The white boxes highlight the positions of the packs. In the boxes one can clearly identify the lateral local distribution of the states within the molecules at the probed energies. The conductance is significantly increased in the area of the N-H bonds, resulting in the red spots in these areas. The backbone and the upstanding phenyl groups, on the other hand, show significantly reduced conductance, resulting in the green and blue areas, respectively.

From the local distributions it becomes very clear that the states at the position of the two N-H bonds of each molecule are not symmetrical or identical on both sides of a molecule. In practically all cases, one sees a considerably higher intensity on one side than on the opposite side within each molecule. This asymmetry is particularly clear for all packs for the unoccupied states (compare, for example, Pack 1 at 140 mV or Packs 2 and 3 at 220 mV), but for Pack 1 also for occupied states, e.g. for Pack 1 at -250 mV. Especially for Pack 1, one can clearly see that the right spot is more intense than the respective opposite left spot at both molecules. This observation is in good agreement with the observations at the corresponding

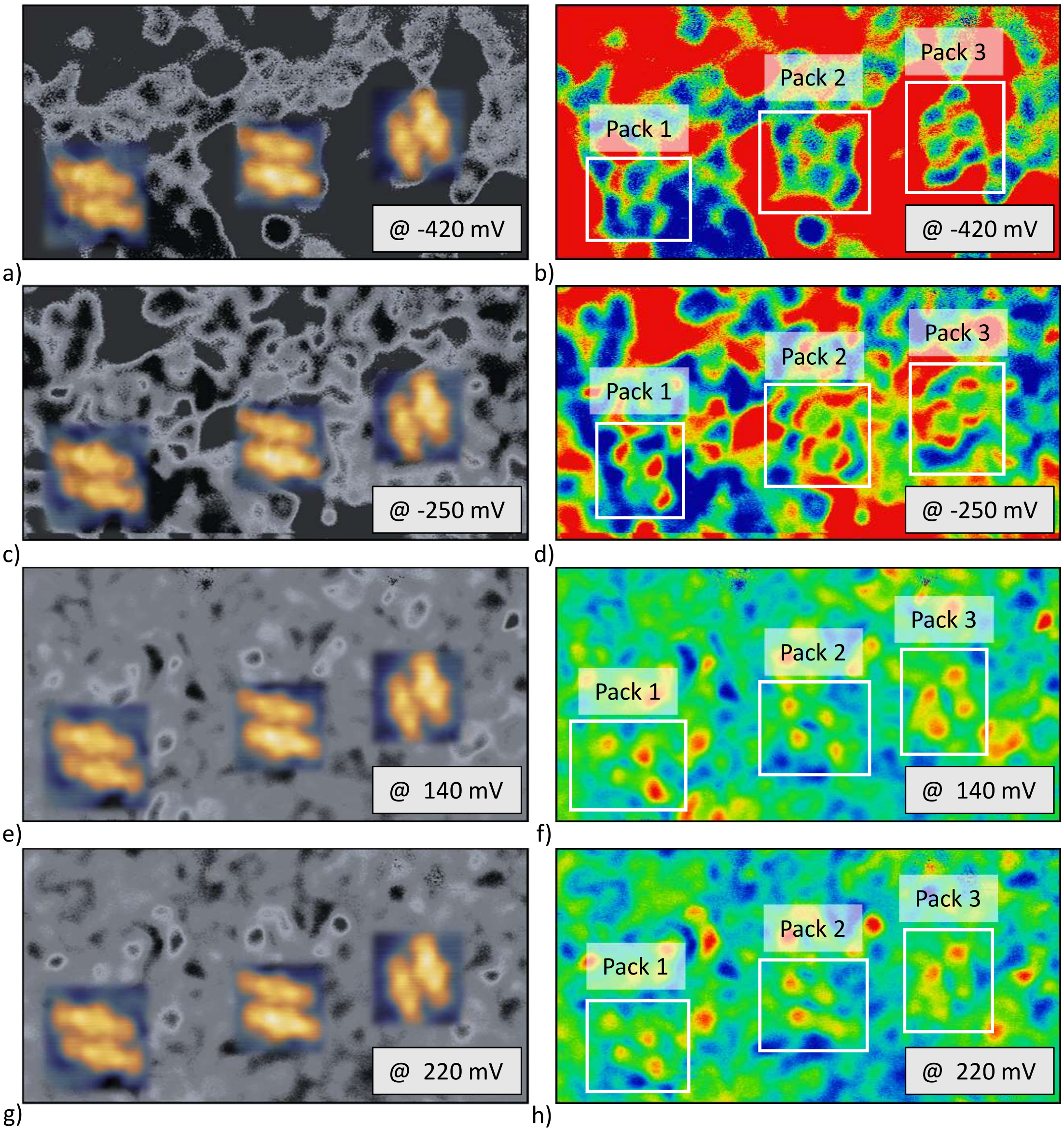

Figure 5.20: $\frac{dI}{dV}$-maps of the same position as the STM and STS measurements in Figs. 5.18 and 5.19. The left column shows the same maps as the corresponding maps of the right column but with grey scale. At the positions of the molecule packs, there are overlays of the STM images for easy reference. Additionally the position of the packs in the right column are marked with boxes (a-b) -420 mV, (c-d) -250 mV, (e-f) 140 mV, (g-h) 220 mV.

STS measurements discussed above. The considerations made in this regard are thus further confirmed by the present results and I conclude, that both mirror sides of each molecule hybridizes differently with the states of the underlying Co(0001). The maps thus also show that the quantitative consideration of the spectra was justified and is reflected in the asymmetry of the states in the maps.

For the reasons discussed above, I conclude that, unlike it is suggested by Fig. 5.16, the adsorption position is not the same for both mirror halves of the BNTCDI molecule. In the following, I refer to this as an asymmetric adsorption position, where the atoms of one half do not occupy the same type of adsorption sites as the corresponding atoms of the other half, with respect to the underlying cobalt atoms.

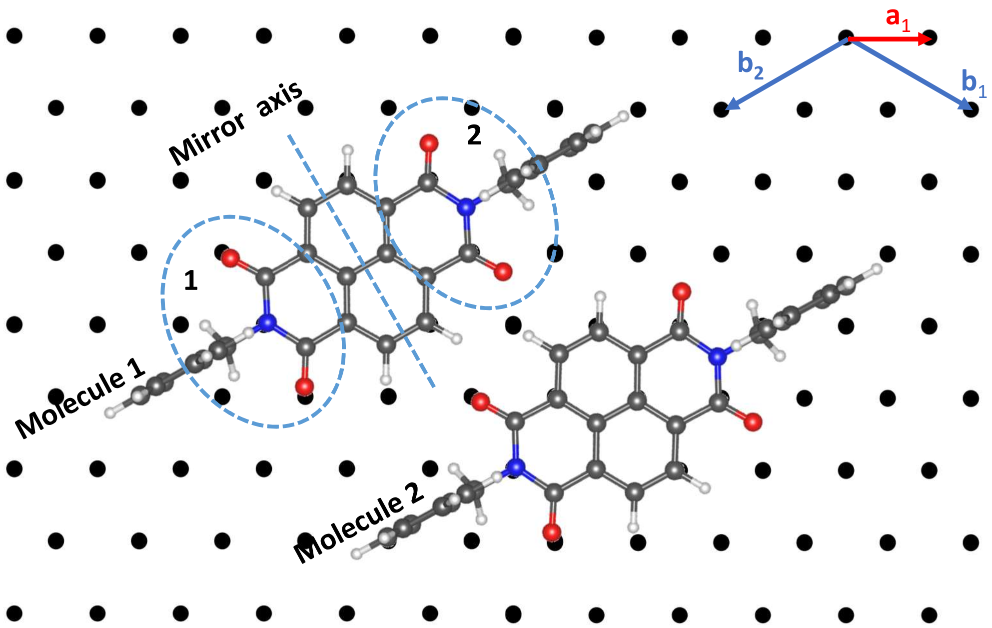

Figure 5.21: The model we derived from our measurements discussed in this chapter and propose for BNTCDI/Co(0001). The left (1) and right (2) half of each molecules do not sit on equivalent adsorption sites. Two neighboring molecules in a pack have equivalent adsorption sites. All molecular dimensions (not plotted) and orientations with respect to the substrate lattice are the same as in Fig. 5.16.

Figure 5.21 shows the model we drafted and propose for the adsorption of BNTCDI on Co(0001), based on the above discussion. At this point, I would like to thank in particular Nicolae Atodiresei (PGI-1/IAS-1) for the fruitful discussions and advice during the course of this thesis, especially with regard to the adsorption geometry and the associated model. The distances and relative orientations of the two molecules with respect to each other are identical as before and in agreement with the model shown in Fig. 5.16. The orientation of the longitudinal molecular axis with respect to the lattice vectors of cobalt also remains the same. The difference, however, is in the adsorption sites to the right and left of the molecular mirror axis. In the region to the left of the molecular axis of the upper molecule, the reactive oxygen atoms essentially bind directly on top of the underlying Co atoms. The same holds for the nitrogen atom (cf. 1 in Fig. 5.21) and in particular for the N-H bond above it. It is assumed that the hybridization and therefore the electronic structure is different from the N-H bond on a hollow site (cf. 2 in Fig. 5.21) and therefore results in an asymmetric DOS on both sides, which is in good agreement with our measurements above. Note that in this model the carbon atoms of the molecules are alternately directly above a Co atom and on a hollow site, while in the model shown in Fig. 5.16 the Co atoms are exactly in the region between two carbon atoms ("underlying bridge position").

Now we have a model where the spacing and orientation fit and the adsorption position has been explained using spectroscopy, delivering a consistent and well defined picture on the adsorption of BNTCDI on Co(0001). The assumed different adsorption sites of the N-H bonds with specific electronic features opens the pathway for their exploitation and invites for further investigation in the future, in particular with respect to a possible spin-splitting of the two features discussed above.

Chapter 6

Building Mesoscopic Devices with Organic Tunneling Barriers

In Sect. 4.3 I investigated the initial growth of epitaxial Co(0001) on Au(111) single crystals and in Chapter 5 the feasibility and parameters of the deposition of BNTCDI on Co(0001) and the adsorption of the molecules on the grown metal substrates. On the basis of these results I conclude that it should be possible to prepare a closed barrier layer of BNTCDI molecules on top of an epitaxial cobalt electrode incorporated in a targeted mesoscopic device. To this extend I aimed at the deposition of multiple layers of BNTCDI to avoid short-circuiting, wherein only the first layer of molecules is considered to interact with the cobalt directly though.

In this chapter the route to the fabrication of such devices will be discussed. It should be noted that major parts of this chapter were published in Ref. [127] which have been largely adopted here. The focus is on the technical fabrication of suitable electrode and barrier geometries as well as the stacking sequence and growth conditions of the individual layers. For this purpose, the Nano Spintronic Cluster Tool (NSCT) described in Chapter 4 had to be modified. In particular, the preparation chamber had to be equipped with a device for shadow masks, wherein shadow masks can be changed *in-situ*, since the whole preparation cycle has to be carried out under UHV conditions. The molecular chamber also had to be equipped with a device to define the barrier geometry. In addition, suitable stacking sequences and film thicknesses had to be investigated. In contrast to the findings of Chapter 4 and Chapter 5, the cobalt substrate/electrode has to be grown on an insulator so that top and bottom electrode are not short-circuited laterally. Therefore, a gold single crystal may not serve as an easy-to-prepare substrate, but Au(111) has to be grown epitaxially on an insulator itself. Eventually, possibilities had to be found to investigate layers grown on an insulator in the STM as well as to remove finished devices from the UHV system without contaminating them in order to perform subsequent ex-situ transport measurements. Finally, both the successful proof of principle and a test device fabricated with an organic barrier of BNTCDI will be presented followed by an error discussion and an outlook for future applications.

As mentioned and discussed in the sections *Rate and Coverage* and *Yield of Intact Molecules* of Sect. 5.2.1, the rate and the yield of intact molecules turned out to be not perfectly reproducible. As mentioned in said sections, it appears that the individual batches and the specific arrangement of the molecule flakes in the crucible play the crucial role in determining these parameters. At this point, it is important to mention that massive problems with the sublimation of BNTCDI molecules from different batches were encountered during the course of this work. This resulted in no BNTCDI being successfully deposited at all for over one year. During troubleshooting and while a technique for enabling electrode geometries was developed and established, several batches of molecules were used and strong efforts were made to successfully deposit BNTCDI (again). These processes have taken a lot of time and caused the long time span between the results of Chapters 5 and 6. The construction measures and in particular the large number of molecule batches ultimately led to the use of evaporation parameters in this chapter which may appear inconsistent with Sect.5.2.1, as suitable parameters had to be found basically for each batch. Last but not least, this has led to the fact that it took a long time before the extremely long evaporation times (cf. Sect. 6.3) were even tried out.

6.1 Technical Feasibility

As mentioned in Chapter 4, a main focus of this work was the design and fabrication of devices. The NSCT as described in that chapter had, despite its extensive analytical and preparation possibilities, so far no equipment to manufacture devices. In order to fabricate the targeted devices, an electrode geometry had to be realized that allows the stacking sequence to be measured *ex-situ* by means of transport measurements. At the same time, the preparation had to take place completely under UHV conditions for the layers had to grow epitaxially and as clean as possible. Furthermore, the individual steps had to be examinable by means ot LT-STM.

For this purpose, the system had to be modified. In particular, suitable sample holders, shadow masks and shadow mask holders had to be realized, which entailed several conversion measures in the molecule and preparation chamber, after which the chambers of the system had to be restored to UHV each time. Since these conversion measures are part of the results of this work, their discussion takes place in the following sections.

6.1.1 STM on Insulating Substrates

Samples grown on insulators cannot be examined by means of STM without further ado since the tunneling current of the STM flows over the sample, the sample plate and the sample holder. However, since the prepared Co(0001) surfaces are highly reactive, they cannot be removed from the vacuum after preparation in order to be contacted subsequently, since in this case the surface would be instantaneously contaminated and thus become unusable. For this purpose (with reference to Fig. 6.1) insulating substrates (2) (e.g. mica or sapphire) were mounted on a standard omicron sample plate (1). A mask (3) of several millimeters width was mounted on the sample to cover its middle area. The sample plate was then placed in a preparation system where a film of 50-100 nm gold (4) was deposited on it. No special preparation parameters were taken into account, since the gold had not be grown epitaxially but only serve for electrical contacting. The sample was then taken out of the system and the mask (3) was removed so that the surface of the middle area (5) is still uncovered insulating material flanked on both sides by gold contact pads.

A metallic aperture (6) with a circular recess was then screwed onto the sample so that the contact pads were in electrical connection with the sample holder via the aperture and screws (not shown). Only then, the sample plate was re-inserted into the NSCT. After subsequent heat treatment to outgas the materials and to remove adsorbates, the sample could be prepared according to need. The metal films (7) grown in this way overlap the contact pads so that the region of interest (8) was in electrical connection with the sample plate and could therefore be examined by means of the (LT-)STM operated in the dedicated STM chamber with a base pressure around $1 \cdot 10^{-11}$ mbar. As usual, STM measurements were performed either with liquid nitrogen (LN_2) or liquid helium (LHe) cooling resulting in a sample temperature of about 78 K or 4.6 K, respectively. This procedure was used to perform the growth studies on insulators to determine suitable growth parameters for the targeted electrodes.

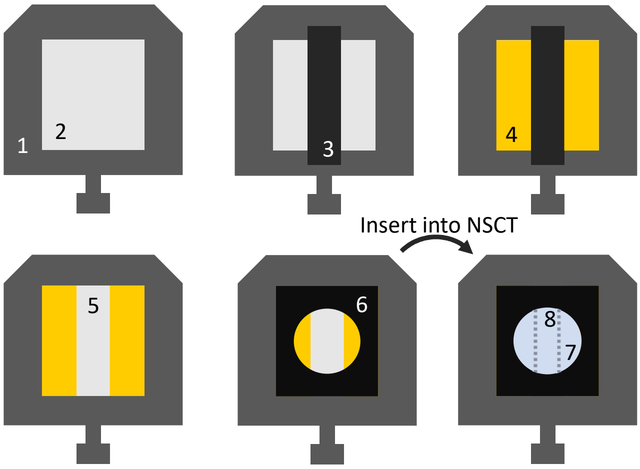

Figure 6.1: Scheme of our procedure in order to investigate epitaxial films grown on insulating substrates. References: 1 sample plate, 2 insulating substrate, 3 mask, 4 gold film, 5 middle area, 6 metallic aperture, 7 metal film, 8 region of interest.

6.1.2 Device Geometry

Besides the growth studies on insulating substrates, the devices/electrode geometry had to be enabled. The geometry of the bottom and top electrodes and the area to be covered with the organic film were defined using shadow-masks. To this end, openings were laser-cut according to the required lateral geometries with dimensions down to 100 μm into standard sample plates from Omicron that then served as shadow-masks.

To be able to place the shadow masks over the sample properly and exchange them *in-situ*, I designed a special sample plate holder with two mounts stacked on top of each other, which was attached to the sample manipulator in the preparation chamber. Figure 6.2(a) shows a CAD drawing of the manipulator head with said sample plate holder with a dummy shadow mask and a sample inserted. The sample is placed in the lower mount (beige) and the shadow-mask in the upper (bronze). The sample plate holder and thus the inserted sample and mask could be rotated around their surface normal via a mechanism of the manipulator, so that it was possible to insert the sample from one side and the mask subsequently from the opposite side. This had the design advantage that the gripping head of the wobble stick did not touch the tab of the other sample plate inserted. In this way, the mask and sample could be placed very close to each other. After both units were inserted in the sample plate holder, the entire assembly could be tightened by means of screws (not shown) which engage in the holes from above. In this way, the manipulator could be rotated in all directions without the risk of one or both units falling out. This was particularly necessary because the crucibles of the evaporators were located underneath the manipulator and one of the two opposite units would otherwise slip out when rotating around the manipulator axis. For this purpose, an *in-situ* screwdriver was fabricated that could be operated like a sample plate with the wobble stick. When doing so, special care must be taken to ensure that the tab does not snap off, which in the worst case has resulted in further venting of the chamber.

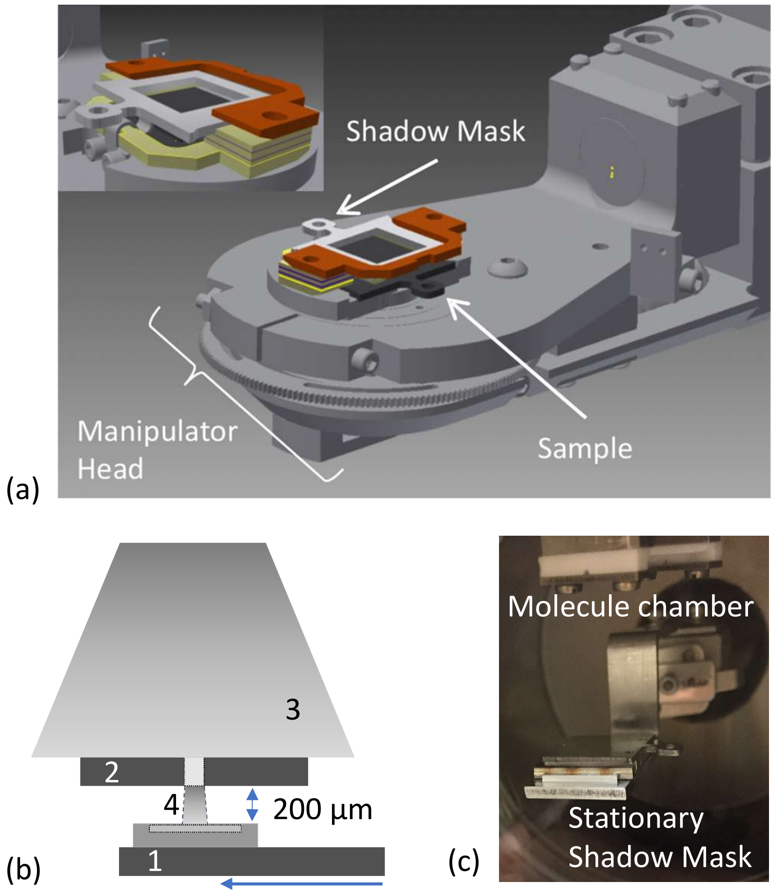

Figure 6.2: (a) CAD drawing of the sample plate holder with two stacked mounts mounted on the manipulator head. Shadow-masks are inserted in the upper mount from the left side and can be exchanged ad libitum. The sample is inserted in the lower mount from the right side; (b) Schematic cross-section in side view: The sample plate 1 with the sample is positioned below the shadow mask 2. The distance between sample and shadow mask is 200 μm so minimize the divergence of the material beam 4 which is cut out of beam 3 coming from the evaporator. (c) Photo of the stationary shadow mask with fixed geometry in the dedicated molecule chamber.

Figure 6.2 (b) shows a schematic cross-section of a sample placed under a shadow mask. Due to the special sample plate with an integrated podest which slightly lifts the sample, a constructive distance between sample surface and mask of only about 200 μm has been achieved. Thus a material beam with very low divergence-induced spread between mask and sample was realized. Another sample plate holder, but with a stationary, non-exchangeable shadow-mask is installed in the molecule deposition chamber (Fig. 6.2 (c)). The stationary shadow mask also served as the holder for the sample, wherein the sample plate could be placed upside down. For reproducible alignment of the sample, stoppers were mounted on the base of the shadow masks. Since the sample was essentially lying freely in the mount, particular care had to be taken as soon as the wobble stick was to release the sample.

In the end, besides snapping tabs of screw drivers, the rotation mechanism turned out to be a major weak point of the manipulator, which was translated to the outside via an axle inside the manipulator over its entire length, resulting in enormous torques when the rotation was actuated. This was exacerbated in particular by the fact that the ball bearings immediately below the sample plate holder turned out to be broken and had to be replaced by friction bearings, causing the rotation to get stuck repeatedly and consequently causing further spikes in torque. As a result, the manipulator (and thus a significant part of the entire NSCT) had to be completely disassembled several times, as said axle and said ball bearings/friction bearings had to be repaired or replaced. In case the route of building devices should be followed further, this may be taken into account when designing the preparation environment.

6.1.3 Proof of Principle

After the modified manipulator head was assembled, the first functional tests were carried out. For this purpose, a first set of shadow masks (cf. Fig. 6.3 (b)) was designed, with an electrode width of 500 μm, so that the overlap area has lateral dimensions of $500\times500\,\mu\text{m}^2$. Muscovite mica was chosen as insulating substrate, which was laser cut into $10\times10\,\text{mm}^2$ sheets and was annealed for 30 minutes prior to preparation (heating current 6 A). Since no gold was available in the system at this time, the bottom electrode was made of copper ($R_{\text{Dep}} = 0.2\,\text{Å/s}$, $d_{\text{Film}} = 30\,\text{nm}$, $p = 1.8\cdot10^{-8}\,\text{mbar}$), the layer of BNTCDI ($I_{\text{Fil}} = 0.25\,\text{A}$, $T \geq 265°\,\text{C}$, $t = 20\,\text{min}$, $p \leq 1.2\cdot10^{-9}\,\text{mbar}$)[1] and the top electrode of chromium ($R_{\text{Dep}} = 0.2\,\text{Å/s}$,

---

[1] See discussion of evaporation parameters in Sect. 5.2.1 and the beginning of Chapter 6

$d_{\mathrm{Film}} = 30\,\mathrm{nm}$, $p = 1.8 \cdot 10^{-9}\,\mathrm{mbar}$)[2] for test purposes. Subsequently, a layer of MgO ($R_{\mathrm{Dep}} = 0.25\,\mathrm{Å/s}$, $d_{\mathrm{Film}} = 15\,\mathrm{nm}$, $p = 1.8 \cdot 10^{-8}\,\mathrm{mbar}$) was evaporated over the entire sample as a capping layer.

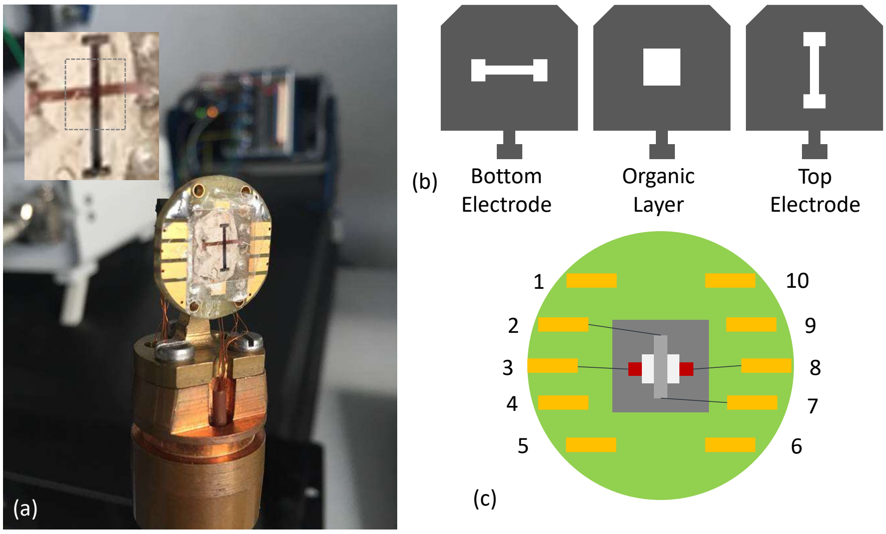

Figure 6.3: (a) The first proto device (Muscovite Mica/Cu/BNTCDI/Cr/MgO) that has been fabricated with the described technique. (b) An exemplary scheme of shadow masks that allows the contacting of the electrodes and the measurement of the resistance through the organic layer. (c) Scheme of a device glued on a carrier with bonded connections for transport measurements.

Figure 6.3(a) shows this very first proto-device. If one looks closely, the organic barrier is faintly visible to the naked eye in the region marked with a gray box in the small section in the upper corner of the picture. After dismounting from the vacuum system, the sample was carefully glued on and bonded to a carrier. Each electrode was connected at both ends with silver wire to a contact of the carrier according to Fig. 6.3(c) so that the resistance could be measured along the electrodes ($2 \leftrightarrow 7$, $3 \leftrightarrow 8$) as well as through the organic layer ($3 \leftrightarrow 2$, $3 \leftrightarrow 7$, $8 \leftrightarrow 2$, $8 \leftrightarrow 7$). Subsequently the resistance has been measured at room temperature to determine if the barrier is closed or not.

The measured resistances were $R_{\mathrm{Bottom}} = 8\,\Omega$ and $R_{\mathrm{Top}} = 21\,\Omega$ for bottom and top electrodes, while the resistance through the organic layer was considerably higher with $R_{\mathrm{Organic}} = 400\,\Omega$. Assuming metallic behavior (Ohm's law) and a layer thickness of $d_{\mathrm{Organic}} = 1\,\mathrm{nm}$ and with the given area $A_{\mathrm{Organic}} = 0.25\,\mathrm{mm}^2$ this yields a

---

[2] Note that Cr is a reactive material acting as getter and thus the pressure during and after evaporation of chromium tends to be lower compared to e.g. Cu

resistivity of

$$R_{\mathrm{Organic}} = \rho_{\mathrm{Organic}} \cdot \frac{d_{\mathrm{Organic}}}{A_{\mathrm{Organic}}} \Rightarrow \rho_{\mathrm{Organic}} = 400\Omega \cdot \frac{0.25\ \mathrm{mm}^2}{1 \cdot 10^{-9}\ \mathrm{m}} = 100 \frac{\mathrm{G}\Omega\mathrm{mm}^2}{\mathrm{m}} \quad (6.1)$$

Comparing this to the resistivity of the metals involved ($\rho_{\mathrm{Cu}} = 0.018\frac{\mathrm{G}\Omega\mathrm{mm}^2}{\mathrm{m}}$, $\rho_{\mathrm{Cr}} = 0.026\frac{\mathrm{G}\Omega\mathrm{mm}^2}{\mathrm{m}}$) reveals that the resistivity through the barrier is significantly larger and does not resemble a metallic conductor even after such a short evaporation time of the organic material ($t = 20\,\mathrm{min}$).

Overall, the result was promising and I concluded that it is possible to fabricate closed organic barriers on top of Co(0001) electrodes with the established technique.

6.2 Growth and Morphology of Co(0001) Electrodes

Now that a proof of principle has been successful, Co(0001) electrodes must be grown and studied on an insulating substrate using shadow mask techniques. In the course of this work two approaches[3] have been explored to achieve an epitaxial Co(0001) surface on an insulating substrate. Since the fabrication of devices and especially the preparation of electrodes on insulators are part of the results of this thesis, the required parameters are mentioned and discussed in this chapter at the appropriate place instead of in Chapter 4.

The first system consists of a commercially available mica [muscovite, $KAl_2(OHF)_2(AlSi_3O_{10})$] sheet as insulating substrate and a Au(111) buffer layer grown on top [112, 113, 75]. The second system consists of a c-cut sapphire plate crystal [$Al_2O_3(0001)$] as insulating substrate and also a Au(111) buffer layer [114]. In this case, however, a very thin Co(0001) seed layer is needed to improve the adhesion of the Au buffer layer [115]. Both systems yield substrates, on which Co can be grown in an epitaxial manner. Note that for the device fabrication, the Au buffer layer of both systems is part of the bottom electrode and thus must be deposited through the corresponding

---

[3] During the extensive troubleshooting process in the course of this work, actually many different systems were fabricated and tested. But these two systems were the starting point from which I proceeded. A small overview of other systems/stackings can be found in the error discussion in Sect. 6.5.

shadow-mask. In the following Sections, the preparation and the resulting Co(0001) film quality for both systems will be presented.

As confirmed in Sect. 4.3 cobalt nucleates at the kinks of the herringbone reconstruction [76] or step-edges of the Au(111) surface [116]. The thus formed nanoclusters grow to double-layer islands, which coalesce with increasing film thickness until they form a continuous cobalt film showing a mesa-type topography. For the application as bottom electrodes in the envisioned molecular spintronic devices, I focused on Co films with thicknesses of 3-5 nm, which have in-plane magnetization and domain sizes in the μm regime [72]. This Co thickness is also well above the fcc-hcp phase transition. Therefore, the film's normal is along <0001> or *c*-direction of the Co hcp phase [71].

6.2.1 Mica Substrate

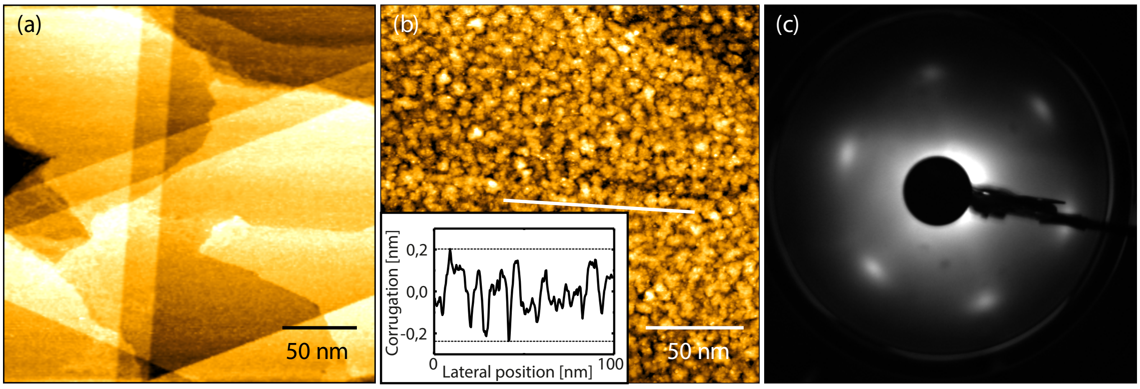

Figure 6.4: Co film on the Au(111)/mica substrate system. (a) STM of the (111) surface of a 100 nm thick Au film grown on mica ($250 \times 250\,\mathrm{nm}^2$, $V_{\mathrm{bias}} = 500\,\mathrm{mV}$, $I_{\mathrm{t}} = 1.0\,\mathrm{nA}$, $T = 77\,\mathrm{K}$). (b) STM of the Co(0001) surface of a 3.3 nm thick film grown on the Au(111) surface shown in (a). The inset shows a line section along the white line ($190 \times 190\,\mathrm{nm}^2$, $V_{\mathrm{bias}} = 700\,\mathrm{mV}$, $I_{\mathrm{t}} = 1.0\,\mathrm{nA}$, $T = 4.6\,\mathrm{K}$). (c) LEED pattern of the Co(0001) film taken at 131 eV electron energy.

Buffer Layer

Laser-cut mica sheets of $10 \times 10\,\mathrm{mm}^2$ are cleaned in a supersonic bath with acetone and isopropanol for 20 min each and subsequently cleaved along the (001)-plane. After immediate transfer into UHV on an Omicron sample plate, the sample is annealed at 810 K for more than 6 h. The growth of gold on mica is well-known and depends on both the evaporation parameters [117] and the substrate temperature [118]. Although gold can be grown by evaporation in a single-step process [119], a two-step process was used to increase the terrace area and decrease the surface roughness [120, 121]. The first deposition step requires a high deposition rate exceeding 2.5 Å/s and a moderate temperature of 573 K, whereas for the second deposition step the rate is reduced by a factor of 5 to about 0.5 Å/s and the temperature is increased to 883 K. The initial step at high rate and lower temperature induces a high density of nucleation centers and many small grains resulting in gold islands. This three-dimensional growth occurs due to the high interface energy between gold and mica and leads to a low lateral conductivity of the film [121]. The second evaporation step at low rate and increased temperature fills up the remaining ditches and leads to a two-dimensional growth mode with flat and large terraces, thereby improving the lateral conductivity of the film [121]. Since the high deposition rate cannot be achieved with the evaporators in the preparation chamber of the NSCT, the deposition was performed in a separate vacuum system by magnetron sputtering. First, a 75 nm thick Au film was sputtered with a rate of 2.7 Å/s and a substrate temperature of 573 K. Then the temperature was increased to 883 K for the sputter deposition of 25 nm Au at a rate 0.5 Å/s in the second step. Accordingly, the total film thickness amounts to 100 nm. After completing the deposition, the temperature is held for 3 h and then decreased step-wise to room temperature (RT) within 3 h. After the transfer through air into the preparation chamber, the sample has been annealed for 1 h at 470 K to remove possibly physisorbed adsorbates. An STM image of the resulting surface is shown in Fig. 6.4(a) and reveals large atomically flat terraces and the characteristic triangular shape of step-edges, very similar to the results in Ref. [121]. The surface morphology is also similar to that of flame-annealed gold films [122, 123] or the (111) surface of a gold single-crystal prepared by cycles of Ar^+ ion-beam sputtering and annealing [124] as discussed in Sect. 4.3.

Co Deposition

I deposit Co from the rod evaporator, according to the findings of Sect. 4.3, although here the Co films were deposited on epitaxially grown Au(111) instead of single crystals. For the investigation of the Co growth on the grown substrates I used a flux of ≈55 nA which has been assumed to correspond to a deposition rate of ≈0.44 Å/min (cf. discussion in Sect. 4.3). The substrate was kept at RT, and the pressure did not exceed $2 \cdot 10^{-10}$ mbar during deposition providing maximum cleanness. In contrast to the Co(0001) surface of Sect. 4.3, the resulting Co(0001) surface exhibits a grainy

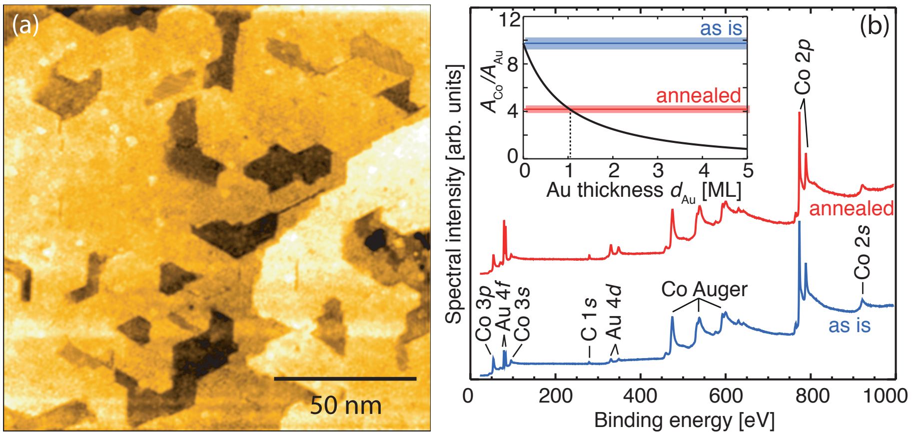

Figure 6.5: Co film on the mica/Au(111) substrate system after post-annealing. (a) STM image of the same sample as in Fig. 6.4 after annealing at 670 K for 1 h. Obviously, the surface morphology has changed considerably and now exhibits large atomically flat terraces. ($150 \times 150\,\mathrm{nm}^2$, $V_{\mathrm{bias}} = 700\,\mathrm{mV}$, $I_{\mathrm{t}} = 0.9\,\mathrm{nA}$, $T = 4.6\,\mathrm{K}$). (b) XPS spectra of the Co film before (blue) and after (red) post-annealing. The latter shows much stronger Au contributions. Inset: Model calculation for a segregated Au film of thickness d_{Au} on the Co surface and comparison with the experimental data. The width of the red and blue lines indicate the estimated error of 5% due to uncertainties in the background subtraction and the choice of the integration interval.

structure (Fig. 6.4(b)) with a lateral grain size of a few nanometers and height variations of less than 0.4 nm (inset of Fig. 6.4(b)). The corresponding LEED pattern in Fig. 6.4(c) confirms the crystallographic (0001) orientation of the surface and the epitaxial growth of the Co film.

Influence of Post-annealing

As the cobalt surface did not resemble the expected mesa like morphology, it was considered to smooth the surface after preparation. A common procedure to improve the surface roughness is to post-anneal a film after deposition. Yet, in the case of Co films on Au this technique turned out to be inapplicable due to Au segregation at the Co surface. Figure 6.5(a) shows an STM image of the Co film in Fig. 6.4(b,c) after annealing at 670 K for 1 h. While the surface clearly shows an altered morphology with a significantly lower roughness and large, more than 50 nm wide terraces, the chemical composition of the surface has changed as well. Figure 6.5(b) shows XPS spectra taken in the ”as is” state after Co deposition (blue) and after post-annealing at 670 K (red), each normalized to the Co $2p_{3/2}$ peak area. Both spectra show clear Co and Au signals and no contamination except a weak C $1s$ peak. However, the

Au signals are much stronger after annealing, as is best seen for the Au $4f$ peak. The XPS peak areas A_{Co} and A_{Au} of the Co $2p_{3/2}$ and Au $2f_{7/2}$ signals, respectively, integrated after subtracting Shirley backgrounds yield a reduction of the peak area ratio from $A_{\mathrm{Co}}/A_{\mathrm{Au}} = 9.76$ before annealing to $A_{\mathrm{Co}}/A_{\mathrm{Au}} = 4.12$ after annealing. Cobalt and gold are immisible below 695 K (solubility <0.05 at.%) [125], but the surface free energies of Co(0001) $\gamma_{\mathrm{Co}} = 2709\,\mathrm{mJ/m^2}$ [126] and Au $\gamma_{\mathrm{Au}} = 1626\,\mathrm{mJ/m^2}$ [126] at RT differ significantly, and the (endothermic) interface free energy of the Au/Co(0001) interface $\gamma_{\mathrm{int}} \approx 138\,\mathrm{mJ/m^2}$ [127] is relatively low. Therefore, the difference between the total free energies of a Co film and a Co film covered by Au atoms

$$\Delta\gamma = \gamma_{\mathrm{Co}} - \gamma_{\mathrm{Au}} - \gamma_{\mathrm{int}} \tag{6.2}$$

is positive and promotes the segregation of Au at the Co surface due to Au diffusion (e.g. along grain boundaries) at elevated temperature [128]. Annealing at 470 K did not change the surface morphology imaged by STM nor the chemical composition measured by XPS. This indicates that Au diffusion sets in at a temperature between 470 and 670 K. Furthermore, the lattice mismatch between Au and Co of 14% facilitates embedding of Co atoms under the first layer of Au during the initial stage of Co growth on Au [129, 130].

In order to quantify the thickness d_{Au} of the segregated Au layer, the XPS peak areas A_{Co} and A_{Au} have been calculated using a continuum model. The Co signal stems from the Co film with thickness d_{Co} (here $d_{\mathrm{Co}} = 3.3\,\mathrm{nm}$), which is located in the depth interval $[d_{\mathrm{Au}}, d_{\mathrm{Au}} + d_{\mathrm{Co}}]$ below the surface:

$$A_{\mathrm{Co}} = s_{\mathrm{Co}} T_{\mathrm{Co}} \int_{d_{\mathrm{Au}}}^{d_{\mathrm{Au}}+d_{\mathrm{Co}}} \exp(-\frac{\zeta}{\lambda_{\mathrm{Co}}}) d\zeta, \tag{6.3}$$

whereas the Au signal comprises contributions from the segregated film and the substrate

$$A_{\mathrm{Au}} = s_{\mathrm{Au}} T_{\mathrm{Au}} \left[\int_{0}^{d_{\mathrm{Au}}} \exp(-\frac{\zeta}{\lambda_{\mathrm{Au}}}) d\zeta + \int_{d_{\mathrm{Au}}+d_{\mathrm{Co}}}^{\infty} \exp(-\frac{\zeta}{\lambda_{\mathrm{Au}}}) d\zeta \right]. \tag{6.4}$$

Here, $s_{\mathrm{Co}} = 12.2$ and $s_{\mathrm{Au}} = 9.79$ are the XPS sensitivity factors given in Ref. [131], $\lambda_{\mathrm{Co}} = 4.9\,\mathrm{ML}$ and $\lambda_{\mathrm{Au}} = 7.7\,\mathrm{ML}$ the photoelectron attenuation lengths according to the universal mean-free path curve [132] for the Co $2p_{3/2}$ and the Au $4f_{7/2}$ lines, respectively. $T_{\mathrm{Co,Au}}$ are the electron analyzer transmission probabilities that are proportional to the inverse of the square root of the kinetic energy of the respective photoelectrons.

The inset in Fig. 6.5(b) shows the calculated ratio $A_{\mathrm{Co}}/A_{\mathrm{Au}}$ as a function of d_{Au} (black line) in comparison with the experimentally determined values before (blue) and after (red) post-annealing. The matching of the $A_{\mathrm{Co}}/A_{\mathrm{Au}}$ value before annealing with the model at $d_{\mathrm{Au}} = 0$ corroborates the absence of Au on the surface after the deposition, and the crossing of the red line with the model curve indicates a Au segregation layer with a thickness of about 1 ML. Hence, the Co surface is largely covered with Au, which hinders the interaction and hybridization of Co $3d$-states with adsorbed molecules. Therefore, post-annealing is not feasible for this system and for our purpose.

6.2.2 Sapphire Substrate

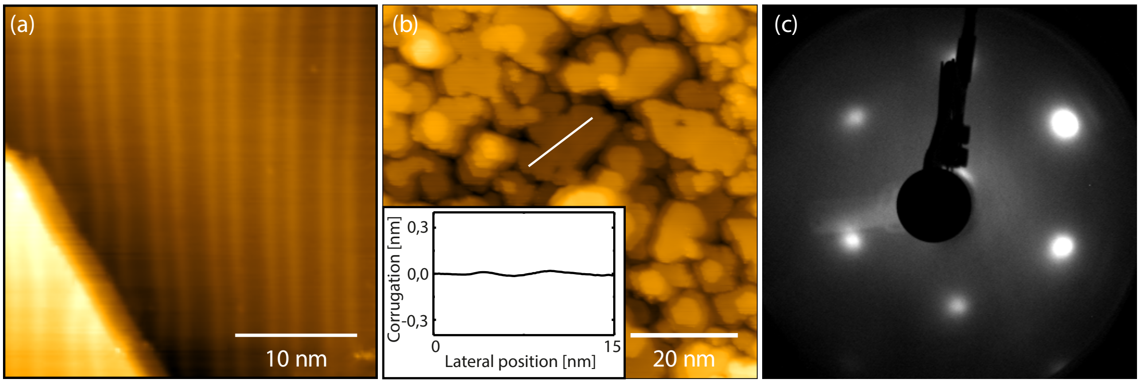

Figure 6.6: Co film on the Au(111)/Co/sapphire substrate system. (a) STM of 50 nm Au(111) grown on a sapphire substrate using a 1 nm Co seed layer. The characteristic herringbone reconstruction is clearly visible ($30 \times 30\,\mathrm{nm}^2$, $V_{\mathrm{bias}} = -700\,\mathrm{mV}$, $I_{\mathrm{t}} = 1.0\,\mathrm{nA}$, $T = 78\,\mathrm{K}$). (b) STM of 4.8 nm Co(0001) grown on the buffer layer depicted in (a). Co forms atomically flat mesas as indicated by the line section shown in the inset ($70 \times 70\,\mathrm{nm}^2$, $V_{\mathrm{bias}} = -700\,\mathrm{mV}$, $I_{\mathrm{t}} = 1.0\,\mathrm{nA}$, $T = 78\,\mathrm{K}$). (c) LEED of the Co(0001) film taken at 156 eV electron energy.

Buffer Layer

A laser-cut sapphire plate crystal with a thickness of 1 mm is cleaned in acetone and isopropanol for 20 min each in a supersonic bath. After the transfer into the vacuum system the crystal is annealed for 1 h at 1123 K to remove adsorbates that remain after chemical cleaning [133]. Afterwards the substrate temperature is reduced to

473 K before the evaporation of cobalt from the rod evaporator starts. The Co seed layer is grown with a rate of 0.04 – 0.06 Å/s to a thickness of 1 nm. The gold film of 50 nm thickness is deposited at the same substrate temperature and with the same rate. After the deposition is finished the temperature is raised to 973 K and kept for 1 h resulting in a flat Au(111) surface with the characteristic herringbone reconstruction as shown in Fig. 6.6(a). Note that the clearly visible reconstruction indicates a clean and well ordered surface.

Co Deposition

After cooling the sample down to RT the cobalt film is grown as in Sect. 6.2.1 to a thickness of 4.8 nm. The corresponding STM topography image and LEED pattern shown in Fig. 6.6(b,c) prove that the film is in fact epitaxially grown with a (0001) surface and consists of mesas with atomically flat tops (see inset of Fig. 6.6(b)). The diameter of the mesas is in the range between a few up to several tens of nanometers. The mesa height is up to 6-8 atomic layers.

6.3 Organic Layer Deposition

As the fabrication of a clean and well defined Co(0001) surface was successful and the surface being essentially identical to the Co(0001) surface grown on a gold single crystal (cf. Sect. 4.3), molecules were evaporated and deposited on the epitaxially grown Co(0001) electrodes in a manner completely analogous to the findings described in Sect. 5.2. In order to produce closed layers with relatively high dielectric strength, only the evaporation time was increased successively during the course of our investigations. The evaporation time[4] has been increased up to 66 h which turned out to be necessary to ensure a closed organic layer without short circuiting. This turned out to be a major obstacle as the NSCT in the current configuration only allows to produce one device at a time. With respect to the extremely low yield of non-short-circuited devices, the route to a proper test-device configuration turned out to be very time consuming as the low yield of non-short-circuited samples made the fabrication of numerous different stacking sequences necessary.

---

[4] cf. corresponding discussion in Sect. 5.2.1 and the beginning of Chapter 6

6.4 Test Device Fabrication and Transport Measurements

In order to demonstrate the feasibility for the presented method of preparing epitaxial Co(0001) bottom electrodes (Sect. 6.2.2) and the *in-situ* deposition of an organic layer of BNTCDI molecules (Sect. 5.2), I fabricated test devices with the layer sequence sapphire/2 nm Co(111)/50 nm Au(111)/5 nm Co(0001)/$\approx$ 5 nm BNTCDI/30 nm Cu/2 nm MgO, see Fig. 6.7(a).

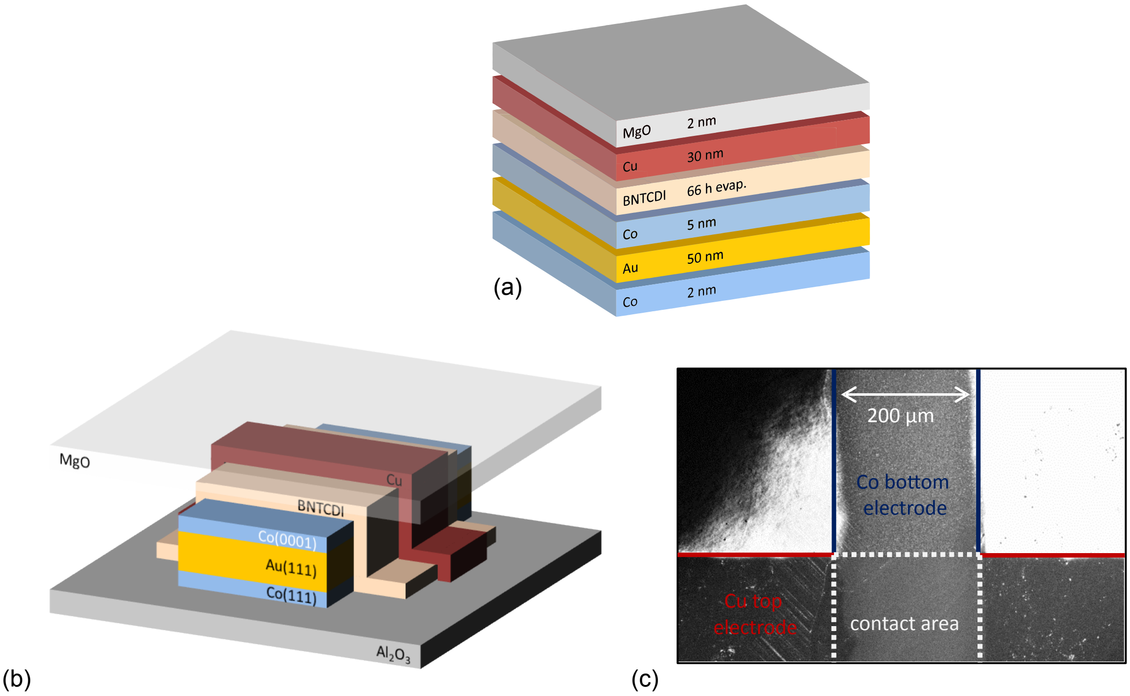

Figure 6.7: Test device. (a) Stacking sequence of the layers. (b) 3D scheme of a single junction. The bottom Co(0001) electrode (blue) and the top Cu electrode (red) can be contacted at both ends, thus enabling 4-probe transport measurements. (c) SEM image of part of a junction taken with 10 kV beam energy. The strong contrast variation on the uncovered sapphire (top left and top right areas) is due to beam-induced charging effects.

The Co/Au/Co bottom electrode has been deposited according to the recipe in Sect. 6.2.2. The BNTCDI organic barrier layer has been evaporated according to the findings described in Sect. 5.2, but with a significantly longer deposition time of 66 h. As mentioned in Sect. 6.3 and in contrast to the expected deposition time of Sect. 6.1.3, this turned out to be necessary, because shorter evaporation times always yielded short-circuited devices due to leaky organic barriers. I relate this observation to a weak intermolecular interaction resulting for the molecules arriving at the surface after completion of the first ML and with a kinetic energy corresponding to the temperature of the crucible (540 K) in a rather low sticking coefficient. The thickness of the BNTCDI layer in the test junctions has been estimated to be of the order of 5 nm. As a top electrode 30 nm Cu has been deposited by evaporation with a rate starting at 0.01 Å/s and slowly increasing to 0.04 Å/s, while the sample is kept at RT. The pressure during Cu deposition did not exceed $5{\cdot}10^{-10}$ mbar. Finally, a 2 nm MgO capping layer has been deposited by evaporation from a crucible with a rate of 0.01 Å/s at RT.

In order to enable transport measurements a set of shadow-masks as described in Sect. 6.1.2 has been used for the fabrication of junctions with the schematic geometry shown in Fig. 6.7(b). The sapphire (Al_2O_3) substrate measures $1\times1\,\mathrm{cm}^2$ and is 1 mm thick. Both top and bottom electrodes have a lateral width of 200 μm and a length of 6.5 mm. The area of the organic layer is $3.5\times3.5\,\mathrm{mm}^2$. The resulting contact size, which is basically the overlap of all layers, is about $200\,\mu\mathrm{m}\times200\,\mu\mathrm{m}$ and is visible in the SEM image in Fig. 6.7(c). The sharp and pronounced edges indicate a small divergence of the shadow-mask deposition resulting from the small mask-to-sample distance of only 200 μm.

Thus fabricated test devices were then removed from the UHV system and transported through ambient conditions to the PPMS machine, where transport measurements have been performed in the 4-probe configuration to eliminate contact resistances. The measurement current was $I = 1\,\mu\mathrm{A}$ and the voltage was limited to $U_{\mathrm{limit}} = 10\,\mathrm{mV}$ to avoid electrical breakdown of the junctions. During all measurements the sample temperature was kept at 10 K.

As will be discussed in Sect. 6.5, the yield of closed barriers, i.e. non-short-circuited junctions was very low. A few test devices were non-short-circuited, i.e. their resistance clearly exceeded the resistance of the bottom and top electrode leads of about 10 Ω. A specific test device showed at 10 K a resistance R of 600 Ω. Assuming Ohmic (metallic) behavior the resistivity ρ becomes

$$\rho = \frac{RA}{d} = 4.8 \cdot 10^9\,\mu\Omega \cdot \mathrm{m}, \tag{6.5}$$

where $A = 0.04\,\mathrm{mm}^2$ is the contact area and $d = 5\,\mathrm{nm}$ the estimated thickness of the molecular layer. This resistivity value is orders of magnitudes larger than for conventional metals (e.g. $\rho_{\mathrm{Co}} = 0.06\,\mu\Omega{\cdot}\mathrm{m}$), and even too large for a poor metal. Note that this statement remains valid even if the thickness of the organic layer

$d = 5\,\mathrm{nm}$ is underestimated by one or even two orders of magnitude. Therefore, the resistance-area product

$$R \cdot A = 24\,\mathrm{M\Omega} \cdot \mu\mathrm{m}^2 \tag{6.6}$$

represents a more suitable characterization of the transport across the organic interlayer. In fact, $R \cdot A = 24\,\mathrm{M\Omega} \cdot \mu\mathrm{m}^2$ is a reasonable value for tunneling through an insulating barrier [134] or hopping transport through an organic layer (see compilation of organic junction resistances in the supplementary information of Ref. [135]).

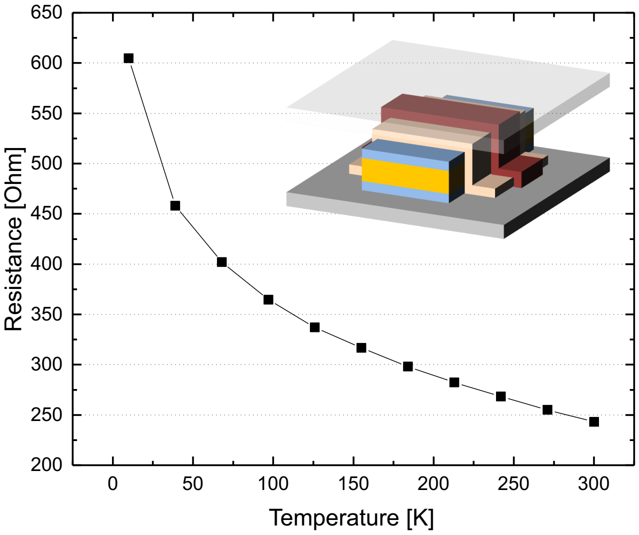

Figure 6.8: Temperature dependence of the resistance. The black dots mark experimental data points, whereas the line serves as guide for the eye.

Further evidence for non-metallic behavior and in favor of tunneling or hopping transport stems from the temperature dependence of the device's resistance shown in Fig. 6.8. The resistance is strongly temperature dependent and decreases with increasing temperature, both in clear contrast with the small and positive temperature coefficient α of metals $\rho(T) = \rho(T_0) \cdot [1 + \alpha(T - T_0)]$, where for instance for copper $\alpha_{\mathrm{Cu}} = 0.004\,\mathrm{K}^{-1}$. In general, a negative α indicates non-metallic conduction. For transport across insulating barriers, however, Oliver et al. [136] have shown that a negative α is a necessary, but insufficient condition to exclude parasitic current flow through pinholes in the barrier layer. According to their model, conductive shorts through pinholes quickly overcome the intrinsic tunneling or hopping conductance in the case of a barrier material with a large $R \cdot A$ product, making the condition $\alpha < 0$ for high-resistive barriers a well-working criterion to exclude a significant impact of pinholes [136]. The $R \cdot A$ product of the present Co/BNTCDI/Cu contact is about four orders of magnitude larger than the $R \cdot A$ products ($< 100\,\Omega \cdot \mu\mathrm{m}^2$) in Ref. [136]. Hence, I conclude that the intrinsic charge transport mechanism through the BNTCDI layer dominates the transport properties in the test device at hand.

After the successful fabrication of a non-short-circuited tunnel junction from organic molecules, the next step would be to investigate the transport properties of the test-devices with respect to their magnetic properties. Raman et al. [9] measured an IMR through a cobalt electrode and an organic junction by sweeping an *in-plane* magnetic field (see Sect. 3.3.2). Unfortunately, the PPMS machine used for this work could only provide an *out-of-plane* magnetic field of ±5000 Oe, so the test-devices presented here could not be investigated for corresponding magnetotransport properties. Measurements with said *out-of-plane* magnetic field did not detect magentotransport. This could and should be made up for in future experiments.

6.5 Failures and Trouble-shooting

The yield of working (i.e. non-short-circuited) devices turned out to be rather poor. The reasons for the high failure rate have been discussed intensively during the course of this work. Numerous different stacking sequences have been fabricated and tried in order to improve the barrier quality and thus rise the yield. Figure 6.9 shows just a selection of some stacking sequences which have been tried, several times each. Starting from the two main underlying approaches described above (mica/Au/Co and sapphire/Co/Au/Co), besides the variation of film thicknesses, the reduction of the device area and the adjustment of evaporation parameters, the following considerations are worth mentioning, as they did not lead to a higher yield of intact tunnel junctions so that they might not necessarily need to be pursued in the future in order to achieve the desired results.

Overall, the preparation of Au was rather difficult and time consuming. In the beginning it was hardly possible to achieve any rate at all, then the crucible had to be changed several times due to contamination or destruction, furthermore the necessary high rates of gold were always in the range of the performance limit of the evaporator. Copper was on the whole easier to handle in our system. It was therefore tried to switch to Cu to be able to grow electrodes easier and faster. Thus, copper was also tried as a buffer layer for the bottom electrode, as Co/Cu is a well studied system [137, 138] and copper can be grown on both mica [139] and sapphire

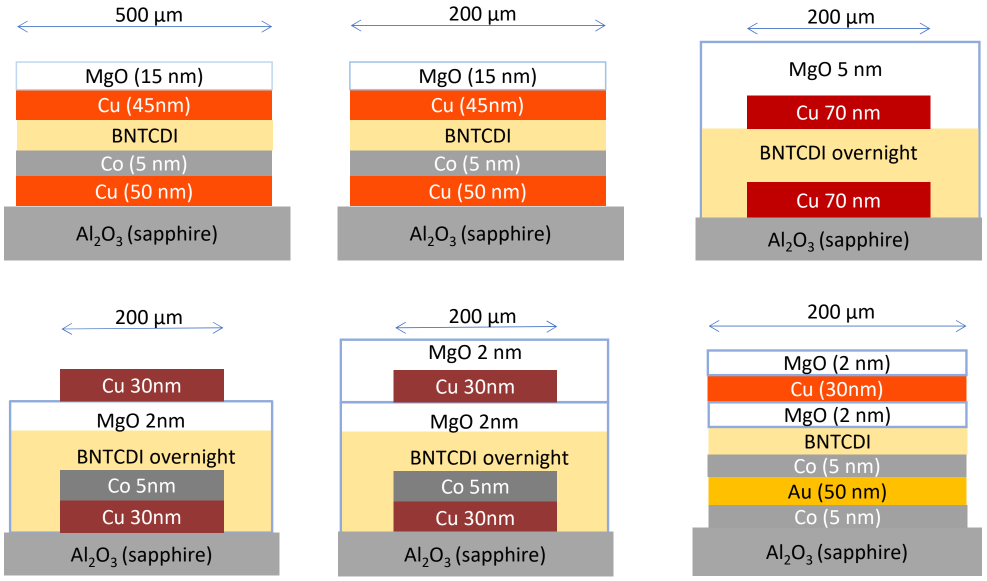

Figure 6.9: Schematic overview over a selection of stacking sequences which have been fabricated during the attempt to increase the yield of closed and non-short-circuited organic tunneling barriers. The layers which extend over the device area indicate that the deposition was performed without a shadow mask and thus over the whole sample area. After numerous attempts, the most successful route is to increase the deposition time of BNTCDI considerably up to several days. Other approaches worth pursuing further are reducing the device area and improving the gold buffer layer quality.

[140, 141].

Another major problem turned out to be the presumed short evaporation time due to the first proto-device (cf. Sect. 6.1.3). It is completely unclear why it was possible to establish a high resistance between the two electrodes so early. Starting from the initially assumed very short 20 min, the evaporation time of the organic barrier was slowly increased bit by bit until eventually almost three full days were necessary to deposit the organic film. The path to such long deposition times might seem logical in a ex post view, but is not obvious when considering that monolayers of BNTCDI could be prepared in a few minutes. The first extreme case was to run the evaporator overnight (up to 24 h) in order to produce a closed film. Eventually, after numerous failures, only quick and dirty Cu electrodes were deposited without stacking of electrode materials, in order to be able to check the organic film as quickly as possible. Finally, the molecules were even deposited without shadow mask, i.e. over the entire sample surface, in order to exclude the possibility that the geometry was faulty and to speed up the production of the proto-devices, which at that point already took several days including sample mounting, outgassing, preparation, bonding and subsequent *ex-situ* transport measurements. To avoid bad electrical contact, I also tried to omit the MgO capping layer. All without finding the source of the error or increasing the yield.

Attempts to improve the barrier quality of the molecular layer by a thin MgO layer between BNTCDI and the Cu top electrode [142] did not improve the yield either. Thus, one can exclude the formation of conducting filaments due to Cu atoms migrating from the top electrode into the BNTCDI film similar to the observation in Ref. [143] as a reason for the observed short circuits.

In addition to short-circuited test devices, there were also test devices with extremely high resistances both through the organic film and along the electrodes. It turned out that the problem was partly due to mechanically broken electrodes and partly due to destruction of the electrodes during the bonding process. The former is mainly relevant for mica, since mica is much more flexible than the used sapphire plate crystals and thus an electrode could easily be damaged by bending. The latter occurred especially when the bonding process was difficult and lengthy, which seems to occur randomly. Figure 6.10(a) shows a SEM image of a test device with extremely high resistance along the bottom electrode measured within a 4-tip STM machine with integrated SEM. The area in the red box is shown at higher magnification in Fig. 6.10(b). It becomes perfectly apparent, that the electrode is mechanically damaged after several attempts of bonding.

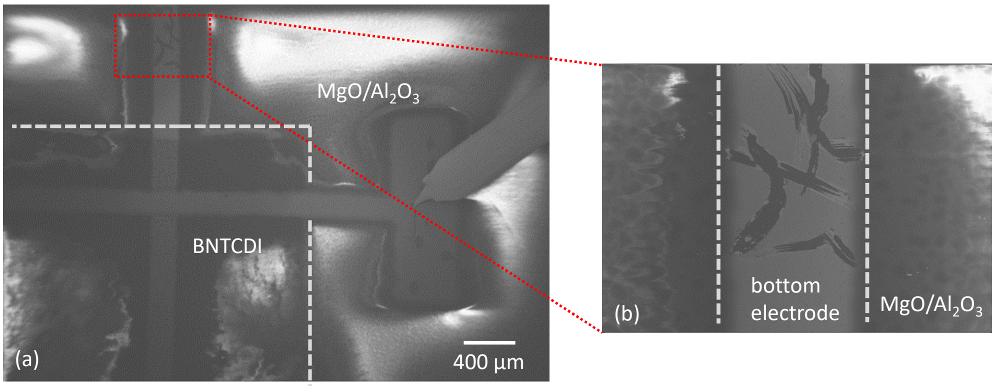

Figure 6.10: (a) SEM of a proto-device during troubleshooting taken with 4.0 kV beam energy in a 4-tip STM machine. The top electrode is contacted with on of the STM tips for transport measurement. (b) Zoom on the marked area of the bottom electrode reveals clear evidence of mechanical destruction which occurred during the attempt to bond the proto-device *ex-situ* with Ag wire.

The problem of the encrusted crucible due to too high evaporation temperature was already discussed in Chapter 5 and resulted in the fact that no molecules could be deposited at all. In this context, it paid off that in addition to the molecule evaporator in the preparation chamber, a suitable evaporator was available in the separate molecule chamber and a shadow mask device was also installed there. This molecule chamber could be vented and pumped down again very quickly, so that it was ready for use again within a few days. As already mentioned, this was necessary a number of times and has led to the fact that the estimated evaporation rate or the required deposition time can vary considerably between the different batches. This has to be taken into account especially with respect to the times given in the last chapters. However, this strong dependence on the batch only became apparent over time, so that initially reproducible behavior was assumed during this work. This led to incorrect assumptions regarding the required time (cf. e.g. Sect. 6.1.3 in comparison to 66 h in Sect. 6.3).

Finally, the transport measurements were performed on different equipment. Among them the mentioned cryo transport lab (PGI-6), the PPMS (JCNS-2), a 4-probe transport station (PGI-7) which was used to circumvent the bonding process as the tips could be placed directly on the electrodes, the same holds for said 4-tip STM (PGI-6) and even quite trivially a simple multimeter were used to measure the resistance. This was done, besides the individual advantages and disadvantages of each measuring station, in order to eliminate malfunctions or voltage spikes inherent to each machine that might have destroyed the barrier before it was measured.

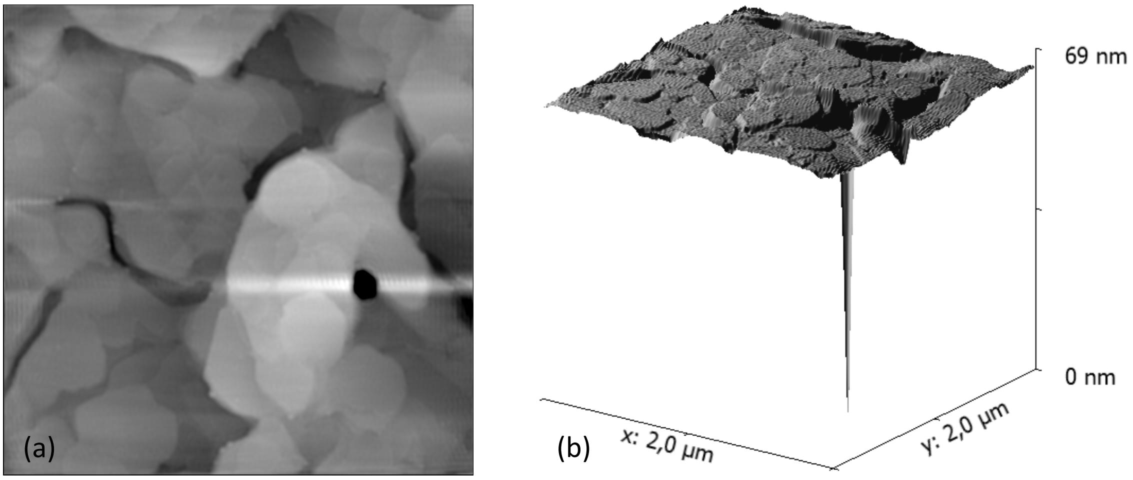

Figure 6.11: Large-scale ($2{\times}2\,\mu\mathrm{m}^2$) AFM image of a 100 nm thick Au buffer layer grown on mica, showing a narrow and deep hole. (a) Topview and (b) 3D sideview of an area comprising a hole.

Most of the routes discussed in this section did not affect the yield of closed barriers. Besides too thin and thus leaky organic barriers mentioned above, I found that narrow, but deep holes in the Au buffer layer, most likely formed during the growth between percolating grains, are a major problem. These holes were detected by large-scale AFM imaging. An example is shown in Fig. 6.11. The imaged depth, which is limited by the AFM tip shape, is about 60 nm and, thus, indicates that the hole possibly penetrates through the whole 100 nm thick Au buffer layer. The sharp edges of such holes cause pinholes and short-circuits in the subsequently deposited Co/BNTCDI/Cu layer structure. Thus, short-circuiting remains a challenge. According to our experience, very long molecule evaporation times and down-sizing of the junction area as much as possible are the most successful means to obtain working junctions in (test) devices. Future efforts need to address in particular the origin of the holes in the Au(111) buffer layer in order to develop strategies to avoid them.

Chapter 7

Conclusion

An entirely *in-situ* preparation cycle enabling the fabrication of organic spintronic devices involving molecular layers has been presented. Emphasis was put on the preparation of epitaxial and contamination-free Co(0001) electrodes on insulating substrates, which are key for the fabrication of junctions, where the electrodes are not only passive supports, but active functionality-enabling parts of the device, e.g. due to chemical bonding and electronic hybridization between the electrode material and the molecules at the very interface. A major goal of this work was to bridge the gap between a small microscopic functional unit (a single adsorbed molecule) and a mesoscopic structure that can be studied by transport measurements. Therefore, microscopic studies in UHV were performed in the course of this work, which served as the foundation for later mesoscopic ex-situ measurements.

Therefore, the precursor molecule BNTCDI, which was mainly used for this work, was investigated for its sublimability and suitable evaporation parameters were attempted to be determined. For this purpose, thin epitaxial Co(0001) layers were deposited on a clean Au(111) single crystal, the former serving as substrate for BNTCDI. Co(0001) was chosen because of the desired interaction between a ferromagnetic metallic surface and organic molecules, particularly reported in Ref. [9, 12, 13]. The Au(111) single crystal was chosen because epitaxially grown gold was to act as a buffer layer in the targeted devices.

It turned out that a constant and reproducible rate and yield of intact BNTCDI is mainly dependent on the individual batch of molecules, while the temperature window for sublimation to take place is rather narrow $T \approx 260 - 270^\circ$ C and has, if any, only a negligible influence on the deposition rate and the yield of intact molecules. As already mentioned, the crucible was refilled several times in the course of the work. Since the material was present in the form of dry flakes, the exact temperature coupling between crucible and material cannot be reproduced with absolute accuracy. In the course of this work, there were also considerable periods of time during which no deposition was possible, at all. Between the STM measurements in Sect. 5.2.1 and the test-device of Chapter 6 lies more than a year and several batches of molecules, which is the reason for the partially incongruent data regarding the rate/evaporation time. In conclusion, the most sensible way is to keep the temperature within the evaporator crucible as constant as possible within the temperature window and to determine the rate anew for each batch of molecules. Within one batch, the results were then essentially reproducible and consistent even though the filling level would decrease over time, again affecting the parameters discussed. Of course, this topic is a potentially remediable problem in industrial production compared to filling the crucibles by hand.

After BNTCDI was successfully deposited on an epitaxial Co(0001) surface, the adsorption and especially the adsorption geometry of BNTCDI on Co(0001) was investigated and a model for the adsorption position was developed. For this purpose, said BNTCDI/Co(0001)/Au(111) samples were investigated by STM and STS. Using STM it was found that the two phenyl groups stand upright pointing away from the substrate, which gives BNTCDI a symmetrical appearance in STM images. It was also found that die intramolecular N-H-bonds appear as bright spots in STM images indicating a higher conductance in this region. Furthermore, an alignment of the molecules along the vectors $\mathbf{b}_\mathrm{n}, n = 1, 2, 3$ of the crystal lattice underneath was determined. It remained open though whether the molecules adsorb mirror-symmetrically with respect to the crystal lattice or not.

Since STM does not allow direct access to the lattice atoms in the immediate vicinity of the molecules, spectroscopic studies were performed at the two clearly localizable sites (said N-H bonds). Based on the STS curves, an asymmetry between the LDOS of the two bonds of a single molecule was inferred. Differences in the curves were determined in the occupied and unoccupied states at energies -420 mV, -250 mV, 140 mV and 220 mV, the first two values being particularly close to a known Co $3d$-surface state. It was also concluded from STS curves that the flatly adsorbed backbone of BNTCDI chemisorbs on Co(0001).

Since STS measurements are extraordinarily dependent on the exact positioning of the tip, which may be difficult due to drift and machine inaccuracy and in particular is impossible to check in practice, it is difficult to assess whether the measured spectra actually correspond to the specific H-N bonds of the molecule. Complicating matters further, the assumed asymmetry in the STS curves was not yet fully validated and clearer evidence was needed as to whether or not there is actually an asymmetry in the LDOS.

For this purpose, $\frac{\mathrm{d}I}{\mathrm{d}V}$-maps were generated for said energies and it turned out that that the determined energies indeed exhibit an intramolecular asymmetry in the region of the N-H-bonds. Advantageously, $\frac{\mathrm{d}I}{\mathrm{d}V}$ circumvent the problem of an accurately placed STM tip so that it was concluded that the two N-H-bonds of one adsorbed molecule indeed have differing LDOSs. In my opinion, this is due to a non-equivalent adsorption position of both N-H-bonds with respect to the underlying lattice. Finally, a final adsorption model was proposed based on the obtained findings.

The next step was to use the microscopic findings to fabricate a first test device. The first step was to develop and establish a way to enable electrode geometries and then to realize a tunneling barrier in an organic junction. The NSCT was extended by the possibility of *in-situ* exchanging shadow masks, and the possibility of growing ordered structures on insulating substrates was established. In order to grow electrodes, the growth of Co(0001) had to be realized on Au(111) films grown on insulating substrates. Both was successfully performed and investigated on muscovite mica an c-cut sapphire. The deposition of closed layers of intact BNTCDI molecules was investigated and implemented as well and a test device with a high-resistance barrier which showed no metallic behavior was fabricated. The next step would be to examine the fabricated test devices within an external in-plane magnetic field for magnetotransport.

The advantage of the presented approach in comparison with other techniques like nanotransfer printing [144] is the fact that rather reactive, but magnetically appealing materials such as cobalt can be employed to exploit molecule-ferromagnet interface properties that only develop at clean and well-defined interfaces under UHV conditions. The presented Co(0001) electrode layers on both the mica- and sapphire-based substrate systems fulfill the demands for clean, epitaxial, well-ordered, and flat surfaces. Further optimization is only needed to avoid the narrow and deep holes in the buffer layers in order to improve the yield of the fabrication process. It seems that emphasis has to be put on the bottom electrode/barrier system which appears to be the main origin of short circuiting. Other error sources have been investigated and discussed and do not seem to play a significant role.

During the studies numerous different systems have been tried e.g. with copper instead of gold buffer layers. Yet the presented systems turned out to be better suited as I had to deal with less short-circuiting of the test devices. Still the exact same approach could be useful by using copper as there are approaches of making molecule/copper interfaces ferromagnetic [145]. Both the mica and the sapphire substrate systems are suitable for proposed applications and can be fabricated without breaking the vacuum to ensure maximum cleanness and magnetic ordering of the Co/molecule interface, while simultaneously delivering an almost inert buffer layer. Yet, mica is easier to prepare and available at low cost. The sapphire system has the advantage of a firm and solid substrate though, which makes *ex-situ* handling and treatment more practical and convenient. For the future, this system seems the more promising approach.

The path taken could be followed further in order to bridge the gap between the microscopic single-molecule properties and the spin and charge transport behavior of organic (inter)layers. In particular, further investigation of the regions above the discussed N-H bonds of BNTCDI with respect to the different adsorption positions (on top of a Co atom vs. on top of a hollow site) may be rewarding.

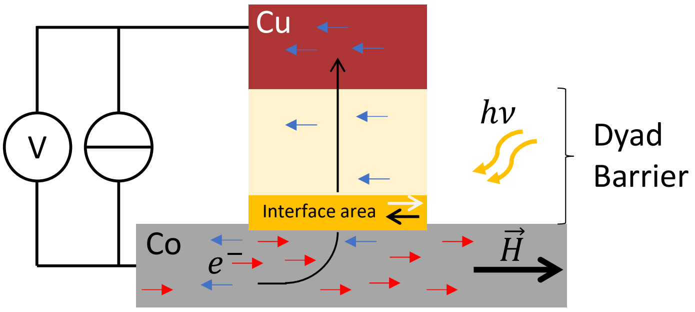

Input		Output
$h\nu$	$\vec{H}$	
1	1	R_{+m}
1	0	R_{-m}
0	1	R_{+M}
0	0	R_{-M}

Figure 7.1: Envisioned device principle. The device on the left is in the low-resistance state ($R_{+\mathrm{M}}$). Due to the applied magnetic field, the Co electrode is aligned parallel to the preferred transmission direction of the molecular spin-filter layer (white arrow). Similar to the discussion in Sect. 3.3.2, a reversed magnetic field can switch the device to the high-resistance state ($R_{-\mathrm{M}}$). If the barrier were to consist of donor-acceptor dyads and if light were to be used to generate a light-induced charge transfer that would influence the electron configuration within the interface area (e.g. switching from high (M) to low (m) magnetization), it might be possible to obtain four resistance states ($R_{\pm\mathrm{M}}, R_{\pm\mathrm{m}}$). The multi-valued truth table of the envisioned logical gate is shown on the right side.

If magnetic investigations may be performed and if necessary BNTCDI can be further developed to confirm a hybrid magnet with its own coercivity on the surface and a spin-split DOS near the Fermi energy, actual functional spintronic devices could be produced in the NSCT. If the chemists succeed in extending the BNTCDI basis into a donor-acceptor dyad with a functional donor moiety (instead of the lateral phenyl rings) and an acceptor part (backbone), it seems conceivable to induce a charge transfer from the donor to the acceptor moiety for example by photo-induced electron transfer (PIET) as shown in [93, 94]. In the long run, this dyad could be further developed in such a way that this charge transfer may influence the hybrid magnet with respect to its DOS and thus affects the spin-dependent tunneling barrier. In this way one would have an interface, which could be addressed functionally by a magnetic external field (by switching the cobalt substrate) and additionally by applying electromagnetic radiation (charge transfer), resulting in a total of four resistance states. Thus a spintronic device would be created, which could be used not only as a logical unit (1/0) but as a logical gate (see Fig. 7.1). This route is in any case worth to be explored further.

In the future, it could be worthwhile to realize even smaller geometries with several devices per sample/shadow mask, so that more devices can be produced in each preparation cycle, since the slow production per device together with the low yield turned out to be a major problem. In this case, however, the already difficult bonding of each electrode becomes even more challenging, so that alternative transport measurement methods may be considered, e.g. with the 4-tip STM.

In any case, the main task in the future will be to increase the yield of closed tunneling barriers. The path that has been paved in this work shows the route that is worth pursuing. Today the yield may still be far to low for technical applications. After all, back in the early days of semiconductor technology, transistors had reject rates of over 98%, too [146].

Bibliography

[1] C. Joachim, J. K. Gimzewski, and A. Aviram. Electronics using hybrid-molecular and mono-molecular devices. 408:541–548, November 2000.

[2] A. R. Rocha, V. M. García-Suárez, S. W. Bailey, C. J. Lambert, J. Ferrer, and S. Sanvito. Towards molecular spintronics. *Nat. Mat.*, 4:335–339, 2005.

[3] S. Sanvito. The rise of spinterface science. *Nat. Phys.*, 6:562–564, 2010.

[4] D. Gatteschi, R. Sessoli, and J. Billain. *Molecular Nanomagnets*, volume 5 of *Mesoscopic Physics and Nanotechnology.* Oxford University Press, New York, 2006.

[5] L. Bogani and W. Wernsdorfer. Molecular spintronics using single-molecule magnets. *Nat. Mater.*, 7:179–186, 2008.

[6] M. Mannini, F. Pineider, P. Sainctavit, C. Danieli, E. Otero, C. Sciancalepore, A. M. Talarico, M. A. Arrio, A. Cornia, D. Gatteschi, and R. Sessoli. Magnetic memory of a single-molecule quantum magnet wired to a gold surface. *Nat. Mater.*, 8:194–197, 2009.

[7] V. Heß, F. Matthes, D. E. Bürgler, K. Y. Monakhov, C. Besson, P. Kögerler, A. Ghisolfi, P. Braunstein, and C. M. Schneider. Adsorption phenomena of cubane-type tetranuclear Ni(II) complexes with neutral, thioether-functionalized ligands on Au(111). *Surf. Sci.*, 641:210–215, 2015.

[8] M. Callsen, V. Caciuc, N. Kiselev, N. Atodiresei, and S. Blügel. Magnetic Hardening Induced by Nonmagnetic Organic Molecules. *Phys. Rev. Lett.*, 111:106805, 2013.

[9] K.V. Raman. Interface-assisted molecular spintronics. *Appl. Phys. Rev.*, 1:031101, 2014.

[10] M. Cinchetti, V. A. Dediu, and E. Hueso. Activating the molecular spinterface. *Nat. Mat.*, 16:507–515, 2017.

[11] S. Schmaus, A. Bagrets, Y. Nahas, T. K. Yamada, A. Bork, M. Bowen, E. Beaurepaire, F. Evers, and W. Wulfhekel. Giant magnetoresistance through a single molecule. *Nat. Nano.*, 6:185–189, 2011.

[12] K. V. Raman, A. M. Kamerbeek, A. Mukherjee, N. Atodiresei, T. K. Sen, P. Lazić, V. Caciuc, R. Michel, D. Stalke, S. K. Mandal, S. Blügel, M. Münzenberg, and J. S. Moodera. Interface-engineered templates for molecular spin memory devices. *Nature*, 493:509–513, 2013.

[13] M. Galbiati, S. Tatay, C. Barraud, A. V. Dediu, F. Petroff, R. Mattana, and P. Seneor. Spinterface: Crafting spintronics at the molecular scale. *MRS Bulletin*, 39:602–607, 2014.

[14] T. Esat, R. Friedrich, F. Matthes, V. Caciuc, N. Atodiresei, S. Blügel, D. E. Bürgler, F. S. Tautz, and C. M. Schneider. Quantum interference effects in molecular spin hybrids. *Phys. Rev. B*, 95:094409, 2017.

[15] K. A. Prior, K. Schwaha, and R. M. Lambert. Surface chemistry of the non-basal planes of cobalt: The structure, stability, and reactivity of Co(10-12)-CO. *Surf. Sci.*, 77:193–208, 1978.

[16] M. C. Biesinger, B.P. Payne, A. P. Grosvenor, L. W. M. Lau, A. R. Gerson, and Smart R. St. C. Resolving surface chemical states in XPS analysis of first row transition metals, oxides and hydroxides: Cr, Mn, Fe, Co and Ni. *Appl. Surf. Sci.*, 257, 2011.

[17] N. Atodiresei and K. V. Raman. Interface-assisted spintronics: Tailoring at the molecular scale. *MRS Bull.*, 39:596–601, 2014.

[18] S. G. Lipson, H. Lipson, and D. S. Tannhauser, editors. *Optical Physics*. Cambridge University Press, 1998.

[19] G. Binnig, H. Rohrer, Ch. Gerber, and E. Weibel. Tunneling through a controllable vacuum gap. *Appl. Phys. Lett.*, 40:178, 1982.

[20] G. Binnig, H. Rohrer, Ch. Gerber, and E. Weibel. Surface Studies by Scanning Tunneling Microscopy. *Phys. Rev. Lett.*, 49:57, 1982.

[21] H.-J. Güntherodt and R. Wiesendanger. Scanning Tunneling Microscopy Vol. 1. *Springer Series in Surface Science*, 20, 1992.

[22] R. Wiesendanger and H.-J. Güntherodt. Scanning Tunneling Microscopy Vol. 2 and 3. *Springer Series in Surface Science*, 28 and 29, 1993.

[23] S. Chiang. Scanning Tunneling Microscopy Imaging of Small Adsorbed Molecules on Metal Surfaces in an Ultrahigh Vacuum Environment. *Chem. Rev.*, 97:1083–1096, 1997.

[24] Ph. Ebert. Atomic structure of point defects in compound semiconductor surfaces. *Curr Opin Solid State Mater Sci.*, 5:211–250, 2001.

[25] R. Strohmaier, J. Petersen, B.Gompf, and W. Eisenmenger. A systematic STM study of planar aromatic molecules on inorganic substrates I. Submolecular image contrast. *Surf. Sci.*, 418:91–104, 1998.

[26] G. Gamov. Zur Quantentheorie des Atomkernes. *Z. Physik*, 51:204–212, 1928.

[27] E. U. Gondon and R. W. Gurney. Wave Mechanics and Radioactive Disintegration. *Nature*, 122:439, 1928.

[28] L. Nordheim. Zur Theorie der thermischen Emission und der Reflexion von Elektronen an Metallen. *Z. Physik*, 46:833, 1927.

[29] L. Ivanova, S. Borisova, H. Eisele, M. Dähne, A. Laubsch, and Ph. Ebert. Surface states and origin of the Fermi level pinning on nonpolar GaN($1\bar{1}00$) surfaces. *Appl. Phys. Lett*, 93:192110, 2008.

[30] Ph. Ebert, L. Ivanova, and H. Eisele. Scanning tunneling microscopy on unpinned GaN($1\bar{1}00$) surfaces: Invisibility of valence-band states. *Phys. Rev. B*, 94:085316, 2003.

[31] C. J. Chen, editor. *Introduction to Scanning Tunneling Microscopy.* Oxford University Press, 2008.

[32] R. Wiesendanger. Spin mapping at the nanoscale and atomic scale. *Rev. Mod. Phys.*, 81:1495, 2009.

[33] V. Hess. *Scanning tunneling microscopy of single-molecule magents and hybrid-molecular magents: Two approaches to molecular spintronics.* PhD thesis, Forschungszentrum Jülich, 2016.

[34] G. Binnig, H. Rohrer, C. Gerber, and E. Weibel. 7 × 7 reconstruction on Si(111) resolved in real space. *Phys. Rev. Lett.*, 50:120–123, 1983.

[35] S. Wanjelik, O. Stolboushkina, S. Königshofen, and M. Getzlaff. Initial step of hydride formation in single crystalline gadolinium thin films and islands studied on the nm-scale. *J. Alloys Compd.*, 645:221–224, 2015.

[36] A. Einstein and L. Infeld, editors. *The Evolution of Physics: The Growth of Ideas from Early Concepts to Relativity and Quanta.* Camebridge University Press, 1938.

[37] M. Getzlaff, editor. *Surface Magnetism.* Springer-Verlag Berlin Heidelberg, 2010.

[38] J. Bardeen. Tunneling from a many-particle point of view. *Phys. Rev. Lett.*, 6:57, 1961.

[39] J. Tersoff and D. R. Hamann. Theory of the scanning tunneling microscope. *Phys. Rev.* ***B***, 31:805, 1985.

[40] J. Tersoff and D. R. Hamann. Theory and Application for the Scanning Tunneling Microscope. *Phys. Rev. Lett.*, 50:1998, 1983.

[41] V. M. Hallmark, S. Chiang, J. F. Rabolt, J. D. Swalen, and R. J. Wilson. Observations of atomic corrugations on Au(111) by scanning tunneling microscopy. *Phys. Rev. Lett.*, 59:2879–2882, 1987.

[42] S. Chiang, R. YJ. Wilson, Ch. Gerber, and V. M. Hallmark. An ultrahigh cacuum scanning tunneling microscope with interchangeable sample an tips. *J. Vac. Sci. Technol. A*, 6:386–389, 1988.

[43] C. Wöll, S. Chiang, R. J. Wilson, and P. H. Lippel. Determination of atom positions at stacking-fault dislocations on Au(111) by scanning tunneling microscopy. *Phys. Rev. B*, 39:7988, 1989.

[44] G. Binnig and H. Rohrer. Scanning tunneling microscopy - from birth to adolescence. *Rev. Mod. Phys*, 59:615–625, 2011.

[45] V. A. Ukraintsev. Data evaluation technique for electron-tunneling spectroscopy. *Phys. Rev. B*, 53:11176–11185, 1996.

[46] J. A. Strocio and W. J. Kaiser, editors. *Scanning Tunneling Microscopy.* Academic Press, Inc., 1993.

[47] R. Wiesendanger, editor. *Scanning Probe Microscopy and Spectroscopy Methods and Applications.* Cambridge University Press, 1994.

[48] C. Hess. Introduction to scanning tunneling spectroscopy of correlated materials. In E. Pavarini, E. Koch, J. van den Brink, and G. Sawatzky, editors, *Quantum Materials: Experiments and Theory Modeling and Simulation.* Verlag des Forschungszentrum Jülich, 2016.

[49] M. N. Baibich, J. M. Broto, A. Fert, F. Nguyen Van Dau, F. Petroff, P. Etienne, G. Creuzet, A. Friederich, and J. Chazelas. Giant magnetoresistance of (001)Fe/(001)Cr magnetic superlattices. *Phys. Rev. Lett.*, 61:2472–2475, 1988.

[50] G. Binasch, P. Grünberg, F. Saurenbach, and W. Zinn. Enhanced magnetoresistance in layered magnetic structures with antiferromagnetic interlayer exchange. *Phys. Rev. B*, 39:4828–4830, 1989.

[51] Y. Tserkovnyak, A. Brataas, and G. E. W. Bauer. Enhanced gilbert damping in thin ferromagnetic films. *Phys. Rev. Lett.*, 88:117601, 2002.

[52] C. W. Sandweg, Y. Kajiwara, A. V. Chumak, A. A. Serga, V. I. Vasyuchka, M. B. Jungfleisch, E. Saitoh, and B. Hillebrands. Spin pumping by parametrically excited exchange magnons. *Phys. Rev. Lett.*, 106:216601, 2011.

[53] M. D'yakonov and V. Perel. Possibility of orienting electron spins with current. *JETP Letters*, 13:467, 1971.

[54] W. Heitler and F. London. Wechselwirkung neutraler Atome und homöopolare Bindung nach der Quantenmechanik. *Z. Physik*, 44:455–472, 1927.

[55] P. Lazić, V. Caciuc, N. Atodiresei, M. Callsen, and S. Blügel. First-principles insights into the electronic and magnetic structure of hybrid organic-metal interfaces. *Journal of Physics: Condensed Matter*, 26:263001, 2014.

[56] G. L. Miesler, P. J. Fischer, and D. A. Tarr. Inorganic Chemistry, 5th ed. *Pearson*, pages 117–165, 475–534, 2014.

[57] Benzene and Aromaticity https://chem.libretexts.org/@go/page/53694 (accessed Apr 11, 2021).

[58] S. Sanvito. Molecular Spintronics. *Chem. Soc. Rev.*, 40:3336–3355, 2011.

[59] N. Ishikawa, M. Sugita, T. Ishikawa, S. y. Koshihara, and Y. Kaizu. Mononuclear lanthanide complexes with a long magnetization relaxation time at high temperatures: A new category of magnets at the single-molecular level. *J. Phys. Chem.B*, 10:11265–11271, 2011.

[60] M. Urdampilleta, S. Klyatskaya, J.-P. Cleuziou, M. Ruben, and W. Wernsdorfer. Supramolecular spin valves. *Nat. Mater.*, 10:502–506, 2011.

[61] D. C. Langreth, B. I. Lundqvist, S. D. Chakarova-Käck, V. R. Cooper, M. Dion, P. Hyldgaard, A. Kelkkanen, J. Kleis, L. Kong, S. Li, P. G. Moses, E. Murray, A. Puzder, H. Rydberg, E. Schröder, and T. Thonhauser. A density functional for sparse matter. *J. Phys.: Condens. Matter*, 21:084203, 2009.

[62] M. L. Perrin, C. J. O. Verzijl, C. A. Martin, A. J. Shaikh, R. Eelkema, J. H. van Esch, J. M. van Ruitenbeek, J. M. Thijssen, H. S. J. van der Zant, and D. Dulic. Large tunable image-charge effects in single-molecule junctions. *Nature Nanotech*, 8:282–287, 2013.

[63] M. C. Lennartz, V. Caciuc, N. Atodiresei, S. Karthäuser, and S. Blügel. Electronic mapping of molecular orbitals at the molecule-metal interface. *Phys. Rev. Lett.*, 105:066801, 2010.

[64] V. Caciuc, M. C. Lennartz, N. Atodiresei, S. Karthäuser, and S. Blügel. Fine tuning of the electronic structure of π-conjugated molecules for molecular electronics. *Nanotechnology*, 22:145701, 2011.

[65] H. Harutyunyan, M. Callsen, T. Allmers, V. Caciuc, S. Blügel, N. Atodiresei, and D. Wegner. Hybridisation at the organic-metal interface: a surface-scientific analogue of Hückel's rule? *Chem. Commun.*, 49:5993, 2013.

[66] C. Barraud, P. Seneor, R. Mattana, S. Fusil, K. Bouzehouane, C. Deranlot, P. Graziosi, L. Hueso, I. Bergenti, V. Dediu, F. Petroff, and A. Fert. Unravelling the role of the interface for spin injection into organic semiconductors. *Nature Phys.*, 6:615–620, 2010.

[67] L. Schulz, L. Nuccio, M. Willis, P. Desai, P. Shakya, T. Kreouzis, V. K. Malik, F. L. Pratt C. Bernhard, N. A. Morley, A. Suter, G. J. Nieuwenhuys, T. Prokscha, E. Morenzoni, W. P. Gillin, and A. J. Drew. Engineering spin propagation across a hybrid organic/inorganic interface using a polar layer. *Nature Mater.*, 10:39–44, 2011.

[68] K. Yoshida, I. Hamada, S. Sakata, A. Umeno, M. Tsukada, and K. Hirakawa. Gate-Tunable Large Negative Tunnel Magnetoresistance in Ni–$C_6$0–Ni Single Molecule Transistors. *Nano Lett.*, 13:481–485, 2013.

[69] F. Matthes and D. E. Bürgler. The Nano-Spintronics-Cluster-Tool. `https://fz-juelich.de/pgi/pgi-6/DE/Leistungen/Instrumentierung/TheNanoSpintronicsClusterTool/_node.html`.

[70] J.L. Bubendorff, E. Beaurepaire, C. Mény, P. Panissod, and P. Bucher. Perpendicular magnetization in ultrathin electrodeposited cobalt films. *Phys. Rev. B*, 56:12, 1997.

[71] D. Renard and G. Nihoul. Crystal structure of a magnetic cobalt layer deposited on a (111) gold surface determined by transmission electron microscopy. *Phil. Mag. Part. B*, 55:75–86, 1987.

[72] R. Allenspach, M Stampanoni, and A. Bischof. Magnetic Domains in Thin Epitaxial Co/Au(111) Films. *Phys. Rev. Lett.*, 65:26, 1990.

[73] B. Voigtländer, G. Meyer, and N. M. Amer. Epitaxial growth of thin magnetic cobalt films on Au(111) studied by scanning tunneling microscopy. *Phys. Rev. B*, 44:18, 1991.

[74] Ch. Rath, J. E. Prieto, S. Müller, R. Miranda, and K. Heinz. hcp-to-fcc stacking in thin cobalt films induced by Cu capping. *Phys. Rev. B*, 55:16, 1997.

[75] N. Spiridis, M. Kisielewski, A. Maziewski, T. Ślezak, P. Cyganik, and J. Korecki. Correlation of morphology and magnetic properties in ultrathin epitaxial Co films on Au(111). *Surf. Sci.*, 507-510:546–552, 2002.

[76] K. Morgenstern, J. Kibsgaard, J. V. Lauritsen, E. Læsgaard, and F. Besenbacher. Cobalt growth on two related close-packed noble metal surfaces. *Surf. Sci.*, 601:1967–1972, 2007.

[77] Q. Meng, S. Guo, X. Zhao, and S. Veintemillas-Verdauger. Bulk metastable cobalt in fcc crystal structure. *J. All. Comp.*, 580:187–190, 2013.

[78] P. Beauvillain, P. Bruno, C. Chappert, H. Hurdequint, K. Le Dang, C. Marlière, D. Renard, and P. Veillet. *Physics, Fabrication, and Applications of Multilayered Structures*, chapter Structure and Magnetic Properties of Cobalt Ultrathin Films, pages 397–399. Springer Boston.

[79] N. Haag, M. Laux, J. Stöckl, J. Kollamana, J. Seidel, N. Großmann, R. Fetzer, L. L. Kelly, Z. Wei, B. Stadtmüller, M. Cinchetti, and M. Aeschlimann. Epitaxial growth of thermally stable cobalt films on Au(111). *New. J. Phys.*, 18:103054, 2016.

[80] C. H. Lee, H. He, F. Lamelas, W. Vavra, C. Uher, and R. Clarke. Epitaxial Co-Au Superlattices. *Phys. Rev. Let.*, 62:6, 1989.

[81] M. Kleinert, H.-F-Waibel, G. E. Engelmann, H. Martin, and D. M. Kolb. Co deposition on Au(111) and Au(100) electrodes: an in situ STM study. *Electrochim. Acta*, 46:3129–3136, 2001.

[82] M. A. Van Hove, R. J. Koestner, P. C. Stair, J. P. Biberian, L. L. Kesmodel, I. Batos, and G. A. Somorjai. The surface reconstructions of the (100) crystal faces of iridium, platinum and gold: I. Experimental observations and possible structural models. *Surf. Sci.*, 103:189–217, 1981.

[83] K. D. Brommer, M. Needels, B. Larson, and J. D. Joannopoulos. Ab initio theory of the Si(111)-(7×7) surface reconstruction: A challenge for massively parallel computation. *Phys. Rev. Let.*, 68:1355, 1992.

[84] S. Narasimhan and D. Vanderbilt. Elastic Stress Domains and the Herringbone Reconstruction on Au(111). *Phys. Rev. Lett.*, 69:10, 1992.

[85] J. Barth, H. Brune, G. Ertl, and R. Behm. Scanning tunneling microscopy observations on the reconstructed Au(111) surface: Atomic structure, long-range superstructure, rotational domains, and surface defects. *Phys. Rev. B*, 42:9307–9318, 1990.

[86] V. Repain, J. M. Berroir, S. Rousset, and J. Lecoeur. Growth of self-organized cobalt nanostructures on Au(111) vicinal surfaces. *Surf. Sci.*, 447:L152–L156, 2000.

[87] C. Lee and A. L. Barabasi. Spatial ordering of islands grown on patterned surfaces. *Appl. Phys. Lett.*, 73:2651, 1998.

[88] K. V. Nefedev and V. Y. Kapitan. Concentration Phase Transition and Hysteresis Phenomena in Co-Nanofilms. Computer Data Processing and Simulation. *Adv. Mat. Res.*, 718-720:69–73, 2013.

[89] R. Lizárraga, F. P., L. Bergqvist, E. Holmström, Z. Gercsi, and L. Vitos. First Principles Theory of the hcp-fcc Phase Transition in Cobalt. *Sci. Rep.*, 7:3778, 2017.

[90] Y. P. Ivanov, A. I. Ilin, A. V. Davydenko, and A. V. Zotov. Optimal Cu buffer layer thickness for growing epitaxial Co overlayers on Si(111)7x7. *J. Appl. Phys.*, 110:083505, 2011.

[91] Y. P. Ivanov, K. V. Nefedev, A. I. Ilin, and V. Y. Kapitan. Ferromagnetism in epitaxial fcc Co films on Si(111)7x7 with Cu buffer layer. *Phys. Proc.*, 23:128–131, 2012.

[92] Elena Dirksen. *Synthese neuartiger Acceptor-substituierter Phenothiazine als Systeme für photoinduzierten intramolekularen Elektronentransfer*. PhD thesis, Heinrich Heine Universität Düsseldorf, 2019.

[93] O. Johansson, M. Borgström, R. Lomoth, M. Palmblad, J. Bergquist, L. Hammarström, L. Sun, and B. Åkermark. Electron Donor-Acceptor Dyads Based on Ruthenium(II) Bipyridine and Terpyridine Complexes Bound to Naphthalenediimide. *Inorg. Chem.*, 42:2908–2918, 2003.

[94] J. W. Verhoeven, H. J. van Ramesdink, M. M. Groeneveld, A. C. Benniston, and A. Harriman. Long-Lived Charge-Transfer States in Compact Donor–Acceptor Dyads. *Chem. Phys. Chem.*, 6:2251–2260, 2005.

[95] T. Nyokong. Electrocatalytic and photosensitizing behavior of metallophthalocyanine complexes. *J. Porphyrins Phthalocyanines*, 12:1005–1021, 2008.

[96] S. Guha, F. S. Goodson, L. J. Corson, and S. Saha. Boundaries of Anion/Naphthalenediimide Interactions: From Anion-π Interactions to Anion-Induced Charge-Transfer and Electron-Transfer Phenomena. *J. Am. Chem. Soc.*, 134:13679–13691, 2012.

[97] M. Martinez-Quiroz, A. Ochoa-Teran, G. Pina-Luis, and H. Santacruz Ortega. Photoinduced Electron Transfer in N,N-Bis(Pyridylmethyl)Naphthalenediimides: Study of Their Potential as PH Chemosensors. *Supramol. Chem.*, 29:32–39, 2017.

[98] M. Seydou, J. Teyssandier, N. Battaglini, G. T. Kenfack, P. Lang, F. Tielens, F. Maurel, and B. Diawara. Characterization of NTCDI supra-molecular networks on Au(111); combining STM, IR and DFT calculations. *RSC Adv.*, 4:25698, 2014.

[99] Y. Miyake, T. Nagata, H. Tanaka, M. Yamazaki, M. Ohta, R. Kokawa, and T. Ogawa. Entropy-Controlled 2D Supramolecular Structures of N,N'-Bis(n-alkyl)-naphthalenediimides on a HOPG Surface. *ACS Nano*, 6:3876–3887, 2012.

[100] C. Fu, H. Lin, J. M. Macleod, A. Krayev, F. Rodei, and D. F. Perepichka. Unravelling the Self-Assembly of Hydrogen Bonded NDI Semiconductors in 2D and 3D. *Chem. Mater.*, 28:951–961, 2016.

[101] T. Kakinuma, H. Kojima, M. Ashizawa, H. Matsumoto, and T. Mori. Correlation of mobility and molecular packing in organic transistors based on cycloalkyl naphthalene diimides. *J. Mater. Chem. C*, 1:5395, 2013.

[102] R. Ebeling, S. Tsukamoto, E. Dirksen, V. Caciuc, T. J. J. Müller, N. Atodiresei, and S. Karthäuser. Imaging Individual Molecular-Like Orbitals of a Non-Planar Naphthalene Diimide on Pt(111): A Combined STM and DFT Study. *J. Phys. Chem. C*, 121(48):26916–26924, 2017.

[103] V. Heß, R. Friedrich, F. Matthes, V. Caciuc, N. Atodiresei, D.E. Bürgler, S. Blügel, and C.M. Schneider. Magnetic subunits within a single molecule-surface hybrid. *New J. Phys.*, 19:053016, 2017.

[104] H. A. Yoon, M. Salmeron, and G. A. Somorjai. Scanning tunneling microscopy (STM) study of benzene and its coadsorption with carbon monoxide on Rh(111). *Surf. Sci.*, 373:300–306, 1997.

[105] K. Momma and F. Izumi. Vesta 3 for three-dimensional visualization of crystal, volumetric and morphology data. *J. Appl. Cryst.*, 44:1272–1276, 2011.

[106] J. D. Dunitz and A. Gavezzotti. How molecules stick together in organic crystals: weak intermolecular interactions. *Chem. Soc. Rev.*, 38:2622–2633, 2009.

[107] F.S. Tautz. Structure and bonding of large aromatic molecules on noble metal surfaces: The example of PTCDA. *Prog. Surf. Sci.*, 82:479–520, 2007.

[108] L. Bartels. Tailoring molecular layers at metal surfaces. *Nat. Chem.*, 2:87–95, 2010.

[109] S. N. Okuno, T. Kishi, and K. Tanaka. Spin-Polarized Tunneling Spectroscopy of Co(0001) Surface States. *Phys. Rev. Lett.*, 88:066803, 2002.

[110] L. Diekhöner, M. A. Schneider, A. N. Baranov, V. S. Stepanyuk, P. Bruno, and K. Kern. Surface States of Cobalt Nanoislands on Cu(111). *Phys. Rev. Lett.*, 90:236801, 2003.

[111] F. J. Himpsel and D. E. Eastman. Intrinsic Λ_1-symmetry surface state on Co(0001). *Phys. Rev. B*, 20:3217, 1979.

[112] H. Poppa, K. Heinemann, and A. G. Elliot. Epitaxial Orientation Studies of Gold on uhv-Cleaved Mica during Early Stages of Nucleation and Growth. *J. Vac. Sci. Technol.*, 8:471–480, 1971.

[113] C. E. D. Chidsey, D N. Loiacono, T. Sleator, and S. Nakahara. STM Study of the Surface Morphology of Gold on Mica. *Surf. Sci.*, 200:45–66, 1988.

[114] G. Kästle, H.-G. Boyen, B. Koslowski, A. Plettl, F. Weigl, and P. Ziemann. Growth of thin, flat, epitaxial (111) oriented gold films on c-cut sapphire. *Surf. Sci.*, 498:168–174, 2002.

[115] M. Kamiko and R. Yamamoto. Epitaxial growth of Au(111) on alpha-Al2O3(0001) by using a Co seed layer. *J. Crys. Growth*, 293:216–222, 2006.

[116] H. W. Chang, B. F. Wu, Y. D. Yao, W. B. Su, and C. S. Chang. Co Nanoislands on Au(111) and Cu(111) Surfaces Studied by Scanning Tunneling Microscopy and Spectroscopy. *J. Nanosci. Nanotechnol.*, 10:4663–4666, 2010.

[117] M. Levlin, A. Laakso, H.E.-M. Niemi, and P. Hautojärvi. Evaporation of gold thin films on mica: effect of evaporation parameters. *Appl. Surf. Sci.*, 115:31–38, 1997.

[118] A. Putnam, B.L. Blackford, M.H. Jericho, and M.O. Watanabe. Surface topography study of gold deposited on mica using scanning tunneling microscopy: effect of mica temperature. *Surf. Sci.*, 217:276–288, 1989.

[119] J.A. DeRose, T. Thundat, L.A. Nagahara, and S.M. Lindsay. Gold grown epitaxially on mica: conditions for large area flat faces. *Surf. Sci.*, 256:102–108, 1991.

[120] U. Höpfner, H. Hehl, and L. Brehmer. Preparation of ordered thin gold films. *Appl. Surf. Sci.*, 152:259–265, 1999.

[121] B. Lüssem, S. Karthäuser, H. Haselier, and R. Waser. The origin of faceting of ultraflat gold films epitaxially grown on mica. *Appl. Surf. Sci.*, 249:197–202, 2005.

[122] G. E. Poirier and M. J. Tarlov. The c(4×2) Superlattice of n-Alkanethiol Monolayers Self-Assembled on Au(111). *Langmuir*, 10:2853–2856, 1994.

[123] M. H. Dishner, M. M. Ivey, S. Gorer, J. C. Hemminger, and F. J. Feher. Preparation of gold thin films by epitaxial growth on mica and the effect of flame annealing. *J. Vac. Sci. Technol. A*, 16:3295–3300, 1998.

[124] J. V. Barth, H. Brune, G. Ertl, and R. J. Behm. Scanning Tunneling Microscopy Observations on the Reconstructed Au(111) Surface: Atomic Structure, Long-Range Superstructure, Rotational Domains and Surface Defects. *Phys. Rev. B*, 42:9307–9318, 1990.

[125] H. Okamoto, T. B. Massalski, M. Hasebe, and T. Nishizawa. The Au-Co (Gold-Cobalt) System. *J. Phase Equilib.*, 6:449–454, 1985.

[126] L. Z. Mezey and J. Giber. The Surface Free Energies of Solid CHemical Elements: Calculation from Internal Free Enthalpies of Atomization. *Jap. J. Appl. Phys.*, 21:1569–1571, 1982.

[127] S. Königshofen, F. Matthes, D. E. Bürgler, C. M. Schneider, E. Dirksen, and T. J. J. Müller. Epitaxial and contamination-free Co(0001) electrodes on insulating substrates for molecular spintronic devices. *Thin Solid Films*, 680:67–74, 2019.

[128] J. Tersoff. Surface-Confined Alloy Formation in Immiscible Sytstems. *Phys. Rev. Lett.*, 74:434–437, 1995.

[129] W. D. Luedtke and U. Landman. Stability and Collapse of Metallic Structures on Surfaces. *Phys. Rev. Let.*, 73:569–572, 1994.

[130] S. Padovani, F. Scheurer, and J. P. Bucher. Burrowing self-organized cobalt clusters into a gold substrate. *Europhys. Lett.*, 45:327–333, 1999.

[131] J. H. Scofield. Hartree-Slater Subshell Photoionization Cross-Sections at 1254 eV and 1487 eV. *J. Electron. Spectrosc. Relat. Phenom.*, 8:129–137, 1976.

[132] M. P. Seah. *Practical Surface Analysis, edited by D. Briggs and M. P. Seah*, volume 1, chapter Quantification of AES and XPS, pages 201–255. John Wiley & Sons, (Sussex, England), 1990.

[133] D. Zhang, Y. Wang, and Y. Gan. Characterization of critically cleaned sapphire single-crystal substrates by atomic force microscopy, XPS and contact angle measurements. *Appl. Surf. Sci.*, 274:405–417, 2013.

[134] S. Yuasa, T. Nagahama, A. Fukushima, Y. Suzuki, and K. Ando. Giant room-temperature magnetoresistance in single-crystal Fe/MgO/Fe magnetic tunnel junctions. *Nat. Mat.*, 3:868–871, 2004.

[135] A. Riminucci, P. Graziosi, M. Calbucci, R. Cecchini, M. Prezioso, F. Borgatti, I. Bergenti, and V. A. Dediu. Low intrinsic carrier density LSMO/Alq3/AlOx/Co organic spintronic devices. *Appl. Phys. Lett.*, 112:142401, 2018.

[136] B. Oliver, Q. He, X. Tang, and J. Nowak. Tunneling criteria and breakdown for low resistive magnetic tunnel junctions. *Appl. Phys. Lett*, 94:1783–1786, 2003.

[137] C. M. Schneider, P. Bressler, P. Schuster, J. Kirschner, J. J. de Miguel, and R. Miranda. Curie Temperature of Ultrathin Films of fcc Cobalt Epitaxially Grown on Atomically Flat Cu(100) Surfaces. *Phys. Rev. Let.*, 64:9, 1990.

[138] J. R. Cerdá, P. L. de Andres, A. Cabollada, R. Miranda, E. Navas, P. Schuster, C. M. Schneider, and J. Kirschner. Epitaxial growth of cobalt films on Cu(100): a crystallographic LEED determination. *J. Phys.: Condens. Matter*, 5:2055–2062, 1993.

[139] G. L. Borges, M. G. Samant, and K. Ashley. Grazing Incidence X-Ray and Electrochemical Study of Thin Film Copper(111) on Mica. *J. Electrochem. Soc.*, 139:1565–1568, 1992.

[140] G. Dehm, M. Rühle, G. Ding, and R. Raj. Growth and structure of copper thin films deposited on (0001) sapphire by molecular beam epitaxy. *Phil. Mag. B*, 71:1111–1124, 1995.

[141] K. Bröhl, P. Bödeker, N. Metoki, A. Stierle, and H. Zabel. Epitaxial growth of Co films and Co/Cu superlattices on sapphire substrates with and without buffer layers. *J. Crys. Gro.*, 127:682–685, 1993.

[142] V. Dediu, L. E. Hueso, J. Bergenti, A. Riminucci, F. Borgatti, P. Graziosi, C. Newby, F. Casoli, M. P. De Jong, C. Taliani, and Y. Zhan. Room-temperature spintronic effects in Alq_3-based hybrid devices. *Phys. Rev.* **B**, 78:115203, 2008.

[143] Y. Busby, S. Nau, S. Sax, E. J. W. List-Kratochvil, J. Novak, R.Banerjee, F. Schreiber, and J.-J. Pireaux. Direct observation of conductive filament formation in Alq3 based organic resistive memories. *J. Appl. Phys.*, 118:075501, 2015.

[144] R. C. Bruce, R. Wang, J. Rawson, M. J. Therien, and W. You. Valence Band Dependent Charge Transport in Billk Molecular Electronic Devices Incorporating Highly Conjugated Multi-[(Porphinato)Metal] Oligomers. *J. Am. Chem. Soc.*, 138:2078–2081, 2016.

[145] F. Al Ma'Mari, T. Moorsom, G. Teobaldi, W. Deacon, T. Prokscha, H. Luetkens, S. Lee, G. E. Sterbinsky, D. A. Arena, D. A. MacLaren, M. Lokstra, M. Ali, M. C. Wheeler, G. Burnell, B. J. Hickey, and O. Cespedes. Beating the Stoner criterion using molecular interfaces. *Nature*, 524:69–73, 2015.

[146] K. C. Handel. *Anfänge der Halbleiterforschung und -entwicklung.* PhD thesis, RWTH Aachen, 1999.

Acknowledgements

Die letzten Seiten möchte ich nutzen, um all denjenigen zu danken, die direkt oder indirekt dazu beigetragen haben, dass diese Dissertation angefertigt werden konnte. Dies sind neben zahlreichen Mitarbeitern des Forschungszentrums Jülich nicht ausschließlich aber insbesondere:

Mein Doktorvater PD Dr. Daniel E. Bürgler, dem ich für die Themenstellung, die Betreuung, die fachlichen und persönlichen Gespräche, die Geduld und nicht zuletzt für die Möglichkeit danke, am Forschungszentrum Jülich forschen und meine Dissertation anfertigen zu dürfen.

Prof. Dr. Schneider, für die Möglichkeit zumindest zeitweise Teil des PGI-6 zu sein und für die tolle Austattung der Labore.

Prof. Michely, für für die Übernahme des Zweitgutachtens.

Die Volkswagenstiftung, die drei Jahre lang meine Doktorandenstelle finanziert und diese Dissertations somit ermöglicht hat.

Dr. Frank Matthes, für die tatkräftige und kompetente Hilfe bei den Modifikationen und Reparaturen am NSCT, für viele interessante fachliche Diskussionen, sowie für die Unterstützung bei der Durchführung vieler STM und STS Messungen.

Thomas Jansen, für die stets zuverlässige und schnelle Unterstützung bei der Lösung von technischen Problemen, sowie für die Herstellung von Substraten mit ”contact-pads”.

Dr. Nicolae Atodiresei, für zahlreiche interessante und äußerst hilfreiche Diskussionen und für die Bereitstellung mehrerer VESTA-Modelle.

Dr. Rene Ebeling, Dr. Elena Dirksen, Dr. Lisa Bensch, Dr. Silvia Karthäuser, Prof. Dr. Thomas J. J. Müller und Dr. Vasile Caciuc, für die gute Zusammenarbeit

und die vielen Diskussionen.

Meine ehemaligen Bürokollegen Dr. Volkmar Hess, für die Einarbeitung am NSCT und Dr. Sebastian Schleicher, für die tatkräftige Unterstützung bei zahlreichen Reparaturen und Umbauarbeiten.

Dr. Timm Flatten, für die Hilfe beim 4-Spitzen-STM und der Suche nach Kurzschlüssen.

Marek Wilhelm, für die Hilfe beim Bonding der Testdevices und bei der Bedienung der PPMS Anlage, sowie die vielen netten Gespräche innerhalb und außerhalb des Forschungszentrums.

Besonderer Dank gilt auch Dr. Ilhan Engin, der mir gerade auch in schwierigen Phasen während und nach meiner Zeit am Forschungszentrum mit Rat und Tat zur Seite stand und mir mehr als einmal aus dem Tal herausgeholfen hat.

Meine Eltern Felicitas und Dr. Volker Lehnert, die mich lange unterstützt und immer an mich geglaubt haben.

Meine Kinder Jonathan, Joshua und Lina, für die vielen Abende die Ihr auf mich verzichten musstet. Ihr wart und seid mein Antrieb.

Meine Frau Carmen, für die jahrelange Unterstützung, die Geduld, das "Rückenfreihalten" und den Verzicht, wenn ich erst abendelang im Labor und später bis spät in die Nacht am Schreibtisch saß. Ohne Dich hätte ich diese Dissertation und so vieles andere nicht geschafft.

Erklärung

Ich versichere, dass ich die von mir vorgelegte Dissertation selbstständig angefertigt, die benutzten Quellen und Hilfsmittel vollständig angegeben und die Stellen der Arbeit - einschließlich Tabellen, Karten und Abbildungen -, die anderen Werken im Wortlaut oder dem Sinn nach entnommen sind, in jedem Einzelfall als Entlehnung kenntlich gemacht habe; dass diese Dissertation noch keiner anderen Fakultät oder Universität zur Prüfung vorgelegen hat; dass sie - abgesehen von unten angegebenen Teilpublikationen - noch nicht veröffentlicht worden ist, sowie, dass ich eine solche Veröffentlichung vor Abschluss des Promotionsverfahrens nicht vornehmen werde.
Die Bestimmungen der Promotionsordnung sind mir bekannt. Die von mir vorgelegte Dissertation ist von PD Dr. Daniel E. Bürgler betreut worden.

Teilpublikationen:
„Epitaxial and contamination-free Co(0001) electrodes on insulating substrates for molecular spintronic devices “, S. Königshofen, F. Matthes, D.E. Bürgler, C.M. Schneider, E. Dirksen, T.J.J.Müller, *Thin Solid Films*, **680**, 67-74 (2019).

Neuss, den 14.11.2021